Cell Wall Nonlinear Elasticity and Growth Dynamics: How Do Bacterial Cells Regulate Pressure and Growth?

Yi Deng

A Dissertation
Presented to the Faculty
of Princeton University
in Candidacy for the Degree
of Doctor of Philosophy

Recommended for Acceptance
by the Department of
Physics
advisor: Joshua W. Shaevitz

November 2012

Abstract

In my thesis, I study intact and bulging *Escherichia coli* cells using atomic force microscopy to separate the contributions of the cell wall and turgor pressure to the overall cell stiffness. I find strong evidence of power–law stress–stiffening in the *E. coli* cell wall, with an exponent of 1.22 ± 0.12, such that the wall is significantly stiffer in intact cells ($E = 23 \pm 8\,\mathrm{MPa}$ and $49 \pm 20\,\mathrm{MPa}$ in the axial and circumferential directions) than in unpressurized sacculi. These measurements also indicate that the turgor pressure in living cells *E. coli* is $29 \pm 3\,\mathrm{kPa}$. The nonlinearity in cell elasticity serves as a plausible mechanism to balance the mechanical protection and tension measurement sensitivity of the cell envelope. I also study the growth dynamics of the *Bacillus subtilis* cell wall to help understand the mechanism of the spatiotemporal order of inserting new cell wall material. High density fluorescent markers are used to label the entire cell surface to capture the morphological changes of the cell surface at sub-cellular to diffraction-limited spatial resolution and sub-minute temporal resolution. This approach reveals that rod-shaped chaining *B. subtilis* cells grow and twist in a highly heterogeneous fashion both spatially and temporally. Regions of high growth and twisting activity have a typical length scale of 5 μm, and last for 10-40 minutes.

Motivated by the quantification of the cell wall growth dynamics, two microscopy and image analysis techniques are developed and applied to broader applications beyond resolving bacterial growth. To resolve densely distributed quantum dots, we present a fast and efficient image analysis algorithm, namely Spatial Covariance Reconstruction (SCORE) microscopy that takes into account the blinking statistics of the fluorescence emitters. We achieve sub-diffraction lateral resolution of 100 nm from 5 to 7 seconds of imaging, which is at least an order of magnitude faster than single-particle localization based methods such as STORM and PALM. SCORE is insensitive to background and can be applied to different types of fluorescence sources, including

but not limited to organic dye and quantum dot that are tested experimentally in this thesis. The second development is an extension from tracking single quantum dot to the more general cases of moving objects at high density based on active contour model. I add a repulsive interaction between open contours to the original model and treat the trajectories as extrusions in the temporal dimension. This technique is applicable to a broad range of problems and two specific tracking problems are chosen as illustrations: (i) the quantification of walking and chasing behaviors of *Drosophila* and (ii) the study of trajectories of gliding bacteria *Myxococcus xanthus* on flat surface. I demonstrate the capability of this high-through and highly automated analysis method for studying social and group behaviors in interacting organisms.

Acknowledgements

At this point of time in graduate school, I believe it is not only me that have a well-mixed feeling about the years of life spent in one place. One one hand, I am excited to take on new adventures and move on to a new stage of life, and on the other, it is just a difficult time to leave all the fantastic people around, as well as the efforts that were put in the failures and accomplishments. During the five years of time, I have learned that becoming a good scientist and scholar was not just about science itself, but also about the ability to work with people synergistically, the spirit to face stress and failure, and a second instinct of critical thinking based on unbiased observations.

The first person I would like to send my gratitude to is who initially brought me here, my advisor Professor Joshwa W. Shaevitz, for the support and freedom he has been constantly offering me. He has always been around the lab, giving critical thrusts to make sure I stay on the track of being productive and innovative, and to direct my focus to the right subjects to learn and study. If it was not the right amount, I could imagine my research drifting in Brownian motion, or myself never reaching the degree of independence I have now.

I would like to acknowledge my examining committee, Professor Ned Wingreen, Thomas Gregor, Ed Groth, and my advisor Josh for reviewing my work, and my second reader, Professor Mala Murthy for reading this dissertation. Mala, and her student Philip Coen are also our collaborator on the *Drosophila* tracking project in Chapter 6. Thanks to Pip for sharing his data with us. It was truly a delightful experience to expand the methods of what I used for bacterial studies to more general applications. I would also like to thank Natacha Ruiz from the Silhavy Lab for teaching me the basics of playing with bacterial genetics, and Professor Zemer Gitai and members from the Gitai lab for support and advices.

The most enjoyable part in the lab apart from getting results is the time I spent with the fantastic members of the Shaevitz Lab. Mingzhai Sun, Teuta Pilizota, Siyuan

Wang and I are the very first generation of the Shaevitz Lab, like the way we shared cubic spaces, we shared the our lives both inside and outside the labs together and had become the stories in each other's life. Teuta, in particular, who sat next to me for three years always had lengthy, amusing, and intriguing discussions about everything with me. It is great to have Hugo Arellano-Santoyo, Gordon Berman, Fabian Czerwinski, Jeffrey Nguyen, David Borenstein, Benjamin Bratton, Nikolay, Daniel Choi, and Sven van Teeffelen around who joined our lab or the neighboring labs. Outside the lab, I have had great time with the crowd that provided social support to me. For that, I thank Anand Murugan, Lin Lin, Bingkan Xue, Arijeet Pal, Liang Li, Guillaume Lambert, Hans Bantilan, and Chris Laumann who said "it can't be wrong to come to Princeton" to me at the open house in 2007.

I would like to give my very special thanks to my wife Jeanie. I would not have been writing this dissertation now, but for years of her understanding and support on my commitment to research. She is always faithful and encouraging with regards to my career choices, and takes over the hard choices with me, and for me. I am also indebted to my parents, who have always been supportive and respect my decision to study half a world away with very limited time for reunion.

Finally, I thank the Grants that funded my research projects: NIH Training Grant through Lewis-Sigler Institute at Princeton University, NSF CAREER Award (Award # 0844466), Sloan Fellowship, and Pew Fellowship.

To my grandma, parents, and my wife.

Contents

List of Tables

List of Figures

Chapter 1

Introduction

Prokaryotic microorganisms, or bacteria, are the oldest, simplest and smallest life form on our planet. Through four billion years of evolution, bacteria acquired a wide range of diversity that grants adaptations to the environment including extreme temperature, chemical composition, and pressure that no other higher life form on earth manage to live, as well as surviving other animal, plants, fungi and bacteria in the game of survival. As a matter of fact, both the bacterial biomass and the genetic diversity far exceed their eukaryotic descendants that take more sophisticate approaches to adaptation. Bacteria diverse in biochemical characteristics such as genetics, metabolism, life cycle as well as physical characteristics such as morphology, motility, and other mechanical properties. These properties are closely interconnected.

1.1 Bacterial morphological diversity and fitness

The morphological diversity of bacteria is displayed as a large variety of both size and shape. The smallest known bacteria *Mycoplasma* takes a radius of a merely 100 nm, while the largest bacteria *Thiomargarita namibiensis*, or sulfur pearl of Namibia has a radius of 100-750 micrometers, clearly visible to naked eye. The great majority of

bacteria has a dimension from 1 to 10 micrometers, typically an order of magnitude smaller than eukaryotic cells. Although a library of various shapes are observed across species, the cell shape is usually well conserved among individual cells of one bacterial specie. Bacterial cells most commonly take shapes of spheres or rods, namely cocci and bacilli respectively[24]. These highly symmetric and thus simple shapes require minimal control effort both genetically and energetically, while the essential cell functions are still fulfilled by these simple shapes. More complex shapes can be found in bacteria that usually exhibit unique cell functions, or that live in specific habitat. For instances, vibrio is a class of bacteria that takes curved rod or comma shape. Spirilla and spirochaetes take spiral or coiled shapes[25, 54]. In rarer cases, bacteria shapes can be tetrahedral, planar, or star-shaped[47, 157].

Bacterial cell morphology is not randomly determined. It is closely regulated in coordination with other cell functions and specific living environment, which impose heavy selective pressure on cell shape. Bacterial cell motility in relation to the cell morphology is one of the most extensively studied and well understood demonstration on selection and adaptation. A tiny perturbation on radius of a merely 0.1 μm costs 5 orders of magnitude more energy for chemotaxis[99, 167]. In addition, the aspect ratio of a rod-shaped bacteria or the curvature of a curved bacteria will determine the radius of the swimming trajectory near the interface between water and solid surface or air, thus alter the ability of a cell to hover around a potential nutrient-rich zone. As another example of cell morphology determining cell function, the division of many rod-shaped bacteria including the model organism *Escherichia coli* relies on the min oscillation, a reaction-diffusion process taking place on the inner surface of the cell[100]. The length scale of the min-oscillation set by the min protein concentration matches the size of the cell, so that a high concentration of the diffusion front traverses along the cell axis back and forth, and this oscillation determines the mid-cell where the division takes place. However, while the cell shape is disturbed by a faulty growth,

the min oscillation no longer creates a robust concentration distribution and the cell mid plane localization fails, leading to fatal division or inability to divide. In the case of more complicated cell shape, such as spiral or coiled shape, the cell can exhibit more sophisticated behavior or function. Experimental observations show that spiral bacteria *Arthrospira* can escape from predation by quickly alternate the handedness or pitch of the spiral[101]. It has also been shown that spiral shape is more efficient in swimming through viscous than rod or spherical shapes[146].

While bacteria regulate and maintain the shape, certain flexibility enable them to perform more complex motion than simple diffusing and swimming in fluid. *E. coli* can swim through a gap as thin as only 30% of its diameter, and is able to grow into even narrower spaces to reach nutrient rich area[103]. Rod-shaped gliding bacterium *Myxococcus xanthus* can make steep turns to its cell body while changing gliding direction[131]. This flexibility further allows *Myxococcus xanthus* to glide in large groups of thousands of cells collectively and eventually form a fruiting body, a higher order structure at millimeter scale, because rigid cell shape disables them to form compact slugs that move in large groups. The overall mechanical property of a bacterial cell appears more elastic at short time scales, and actively adaptive and self-organized at longer time scales of cell cycle during cell growth.

1.2 Cell envelope structure and mechanics

The cell morphology is constantly under challenges from the external environment. Solute osmolarity imposes a mechanical stress on the bacterial envelope, with a magnitude that may vary depending on the environment, which can be a freshwater lake or the intestine of an animal, and the osmotic pressure differs by orders of magnitude. Direct mechanical perturbations also act on the isolated cells or the ones in biofilms, an aggregate of bacterial cells that are held together by extracellular poly-

meric substance (EPS). Bacterial cells almost always have to deal with the changing environment and withstand a variable stress and external mechanical perturbation.

Bacterial have particular structural elements to maintain cell shape. In a simplified picture of bacterial cell structure, DNA, which is the main genetic material, and viscous cytoplasm that contains certain composition of salts, small organic molecules and enzymes are enclosed in a semi-permeable cell envelope. The selective permeability is maintained by cytoplasmic membrane that functions as a barrier to maintain a proper internal environment for essential biochemical functions. Outside the cell membrane, most bacteria have a relatively rigid exoskeleton that acts as the key structural role to define the cell shape. The space between the cell wall and cell membrane is called periplasmic space. A class of bacteria have another membrane outside the cell wall, and many have flagella and pili as surface appendages (figure 1.1) .

Cell wall

Similar to plant cells and many kinds of fungi, bacteria use cell wall to define and maintain cell shape. Bacterial cell wall is a polymer mesh network enclosing the entire cell body as a relatively rigid shell[158]. The chemical composition of bacterial cell wall is known as peptidoglycan (PG), also called murein, and is well conserved among almost all bacteria. The saccharide (poly-N-acetylglucosamine and N-acetylmuramic acid) polymerize into the backbone of the

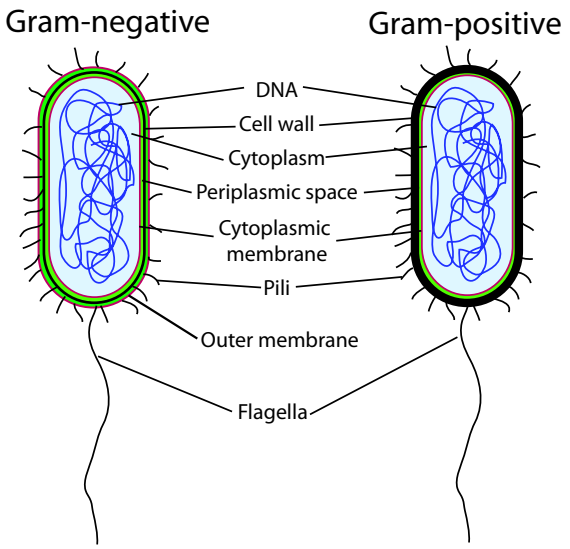

Figure 1.1: Gram-negative and gram-positive bacterial structure shown in cartoons.

PG, while the peptide containing special D-alanine crosslinks the sugar backbones. Bacteria can be broadly categorized to two classes, Gram-positive and Gram-negative bacteria based on the result of the Gram stain[7] (figure 1.1) . The difference in Gram stain is resulted from the difference of the cell envelope architecture: Gram-negative cells have an outer membrane outside the cell wall, whereas it is absent in gram-positive cells. Outer membrane mainly serves as an initial selective barrier to screen potentially harmful chemicals or biomolecules[104, 117]. Gram-positive and -negative bacterial cell wall are also different in the thickness, Gram-positive being thicker (20-80 nm) than Gram-negative (5-8 nm)[97]. Moreover, Gram-positive bacterial cell wall contains teichoic acids that are not found in Gram-negative cells, but the bulk of Gram positive bacterial cell wall is identical[97]. Since cell wall allows small chemicals and proteins to freely travel through, its main function is narrowed down to providing mechanical protection to the inner membrane from lysing due to the turgor pressure, and to define the cell shape. Consequently, the disruption of cell wall will cause inner membrane bulges[32], abnormal cell morphology[53], spheroplasts[16] or cell lysis.

Turgor pressure and osmoregulation

The cytoplasm is enclosed by the semi-permeable cytoplasmic membrane underneath the cell wall (figure 1.1). The transporters on the bacterial cytoplasmic membrane are essential to the membrane selective permeability, and consequently the cell viability[161]. From a mechanics point of view, the cytoplasmic membrane maintains a higher concentration of solute in the cytoplasm than the external environment. The difference in osmotic pressure, namely the turgor pressure, pushes the membrane against the cell wall. The turgor pressure and the cell wall together define the over mechanical and geometric property of a bacterial cell.

Instead of passively keeping a high turgor and relying on a strong cell wall, bacterial cells are able to regulate the turgor pressure according to the changing envi-

ronment. Maintaining a proper turgor pressure is vital to cell viability. For example, the osmolarity that *E. coli* can tolerate ranges from 0.015 to 3.0 Osm[10, 115], which corresponds to osmotic pressures ranging from 0.4 atm to 74 atm. Without active adaptation, the cytoplasm hydration and the tension on the cell envelope would vary depending on the environmental osmolality in large magnitudes. Under abnormal hydration conditions, harsh concentration of the cytoplasmic solutes, especially salts threats the confirmation and function of essential enzymes by denaturing them, thus conditioning the internal environment is essential. Bacteria achieve the adaptation to the changes in osmotic pressure by uptaking or exporting specific solutes[161], or by internally synthesizing and breaking down larger molecules, usually polysaccharide in the cytoplasm[136, 80]. The adaptation requires the coordination of a set of osmo-sensitive regulatory proteins and channels residing on the cytoplasmic membrane. The major response to the osmotic up-shock is to activate the transporters to import osmolytes to bring up the turgor pressure. Compatible solute covers a wide range of chemicals, including potassium salt, amino acids such as proline and amino acid derivatives such as betaine, choline and ectoine[161]. Under osmotic down-shocks, the fast influx of water can result in an increase of turgor pressure at the scale of 10 atm in a few milliseconds. Mechanical sensitive channels MscS and MscL undergoes conformational changes to release osmolytes to induce water efflux thereafter deflates the cell[29, 18]. The activation is directly gated by the membrane tension caused by the high turgor pressure[121, 58]. The mechanosensitivity of these exporters are confirmed in patch-clamp experiments *in vitro*[171, 14] and viability assay *in vivo*[85, 93].

A fundamental question: how is tension distributed between wall and membrane?

The roles of the semi-permeable membrane and the rigid cell wall appear well characterized and separated: the former maintains an ideal turgor pressure, which transfers

to the latter by a normal force between the two, and becomes a lateral surface tension on the cell wall. The fact that cell wall, if a bacteria specie has it, is vital suggests that the tension baring function of cell wall is necessary, and the membrane itself can not withstand the turgor pressure. However, if the mechanosensitive channels and transporters function based on the membrane surface tension, the cell wall must not take all the surface tension. A fundamental question regarding bacterial cell mechanics that one shall ask is *how the surface tension generated by the turgor pressure is distributed between cell wall and cell membrane*, to give rise to overall good protection against the turgor pressure, while allowing channels and transporters that reside on cell membrane regulate turgor through mechanical cues on the membrane. If the membrane surface area is larger than that of a rigid cell wall, tension sensory proteins will have no tension to measure, leading to zero sensitivity to the change of turgor pressure. On the other hand, the cell wall area must not exceed membrane surface area, or it will no long take tension to protect the cell membrane from rupture. This argument suggests that the surface area of the cell wall and cell membrane must be almost equal at their physiological tension respectively. Under this assumption, the distribution of the surface tension on both the cell wall and cell membrane depends on their elastic property respectively, and balances the protection of the cell wall and the tension measurement sensitivity.

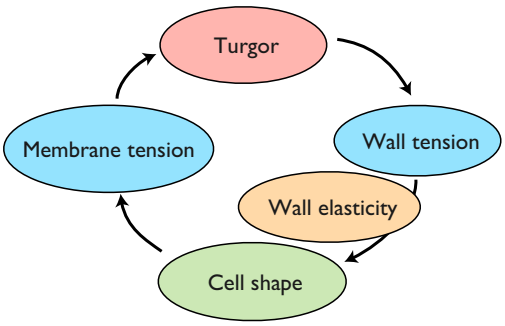

Figure 1.2: Osmotic regulation scheme through mechanical and geometric cues in bacteria.

I propose a feedback mechanism how bacterial cells respond to the external osmotic changes by changing the shape, tension and turgor pressure, qualitatively explained as the following. Given that the cell wall is the major tension baring structure, turgor pressure determines how much tension is applied on the cell wall. Together with a specific elasticity of

the wall, the tension sets an equilibrium surface area. As a weaker structural element, the area of the membrane follows the cell wall, and in turn governs the membrane tension. The mechanosensitive channels and transporters then act according to the membrane tension. One goal of this thesis is to quantitatively characterize the elasticity of cell wall and turgor to address the tension distribution question, and to validate this feedback scheme.

Previous works

Both cell wall elasticity and turgor have been experimentally studied in the literature by directly applying mechanical perturbations or indirectly evaluating the chemical concentration in the cytoplasm. Special types of bacteria such as cyanobacteria and halobacteria contain gas vesicles that can reflect the magnitude of the turgor pressure[153, 68]. These vesicles connect the pressure to the optical observables. By comparing the collapsing fraction of the gas vesicles in different media and external pressure, the turgor pressure was measured to be in the range of mega-pascal. The major limitations of this method lay in the fact that only a small portion of bacteria contains gas vesicle, and cells may active adapt to the change of the pressure. Another type of direct quantification of the turgor pressure is achieved with the Atomic Force Microscopy (AFM). AFM is capable of applying a localized force to the surface of an object and to quantify the substrate stiffness, which is related to the turgor, and from the stiffness measurement, proper mechanical model of the deformation is required to extract turgor pressure. Arnoldi[5] and Yao [166] had modeled the Gram-negative cells as inflated spheres or tubes enclosed by elastic membrane that is free to bend. From their models and measurement on cell stiffness, the turgor pressure was measured as 85-150 kPa in *Magnetospirillum gryphiswaldense* and 10-20 kPa in *E. coli*. These values are smaller than the typical measurements from the gas vesicle, even

though the effect of the cell wall bending is already neglected. Although mechanical experiments, such as AFM indentation, are the most direct probes, separating the mechanical contributions of the wall and pressure has not been previously possible and thus these experiments may only provide an upper bound on the true turgor pressure. Turgor pressure can be estimated by evaluating the total solute concentration and water activity in a range between 50 kPa to 310 kPa[26].

The other mechanical component, the cell wall elasticity has been difficult to probe in individual, live cells. Most previous mechanical measurements on the cell wall have been performed using chemically isolated walls, termed sacculi, that may be altered from the native state, or on large bundles of cells. Yao *et al.* reported an anisotropic elasticity of 25 MPa and 45 MPa in the axial and circumferential directions relative to a cell's rod-shape using single flattened *E. coli* sacculi[165] measured with AFM. Thwaites *et al* probed the elastic modulus of macroscopic threads of many *Bacillus subtilis* sacculi in humid air and found that the modulus varied from 10 to 30 MPa depending on the humidity and salt concentration[142, 143, 96]. Mendelson *et al* measured the relaxation of single bent *Bacillus subtilis* filaments and determined the modulus to be 50 MPa[95]. Attempts to probe whole–cell elasticity have also been made using AFM indentation of *Myxococcus xanthus* cells[112] and optical–tweezer bending of *Borrelia burgdorferi* cells[41].

Cross-linked polymer meshes, especially ones that play structural rules are expected to exhibit novel nonlinear mechanical properties such as stress–stiffening[50, 82, 140, 22, 78]. Unpressurized sacculi thus provide a poor platform for estimating the wall elasticity in live cells. Boulbitch*et al* modeled the cell wall as a deformable hexagonal mesh and predicted a load-dependent elasticity with a power–law stress–stiffening exponent of about one[19]. Thwaites and coauthors found about an order of magnitude change in the thread modulus upon loading, although it is unclear how

to interpret measurements from these very large, multi–sacculus objects performed in air[142, 143, 96].

Mechanical indentation of live cells is likely the most direct method for probing these sorts of mechanical properties. Under external perturbation, however, the cell wall and turgor pressure have mixed contributions to the response, making it hard to independently estimate these two quantities. By studying a bulging strain of *E. coli*, we are able to simultaneously determine both the wall elasticity and the turgor pressure and reveal their dependence as discussed in details in Chapter 3. We argue that this nonlinear elasticity of cell wall serves as a passive-adaptation strategy to balance the membrane tension measurement sensitivity and cell wall protection against hypoosmotic shocks.

1.3 Dynamics of cell wall growth

Bacterial cell wall is not a static structure, but undergoes constant remodeling during cell growth because the shape that the cell wall defines changes as cells grow. The growth of cell wall is established by inserting the subunits of peptidoglycan into the existing wall with enzymes that reside on the inner cell membrane. The peptidoglycan biosynthesis is a set of complex pathways that involves approximately 20 enzyme reactions, with the details discussed in a recent review[89]. In brief, PG biosynthesis is a three-stage process. As the first stage, the precursors of peptidoglycan, UDP-N-acetylmuramyl-pentapeptide (UDP-MurNAc-pentapeptide) and UDP-N-acetylglucosamine (UDP-GlcNAc) are synthesized in the cytoplasm. In the second stage, phospho-MurNAc-pentapeptide assembles with undecaprenyl phosphate carrier on the inner surface of the cell membrane to form lipid I, which is modified to lipid II by adding GlcNAc, and then translocated through the membrane to the periplasm. In the last stage, the peptidoglycan subunit carried by lipid II is incorporated into

the existing cell wall by transglycozylation and transpeptidation. The peptidoglycan biosynthesis mechanism is conserved among almost all bacterial species, yet this universal mechanism is able to give rise to a collection of different shapes, and the shapes are maintained with high accuracy during cell growth. This remarkable observation brings up the second fundamental question that I will address in my thesis: *How is the material inserted to the existing cell wall to give rise a robust growth?* Biologically, the answer is recapitulated above as a series of biosynthesis processes. Physically and geometrically, we are interested in what the specific insertion rule is for the new material, in terms of the insertion location and rate. In this thesis, I mainly focus on the mechanism that generates rod shapes as in model organism *E. coli* and *B. subtilis*.

Peptidoglycan insertion machinery and architecture

The polymerization of single peptidoglycan subunits in the third stage of PG synthesis takes place on the outer surface of the cell membrane. Broadly speaking, the growth for a rod shaped bacterial cell wall can be categorized into two kinds: elongation and division, which typically happens in the mid-cell plane. Asymmetric division is frequently adopted by rod-shaped bacteria as well, such as in the sporulation of *B. subtilis*. The major enzymes that facilitate the PG insertion are called penicillin-binding proteins (PBPs). Even though PBPs are usually specialized in elongation and division, for example PBP2 for elongation and PBP3 for division in *E. coli*, in each bacterial specie, many different types of PBPs coexists and carrie redundant function. For instance, *E. coli* has 12 known types of PBPs while *B. subtilis* has as least 16 types[123]. Because of the functional redundancy, and the fact that they usually form complexes that contain multiple types of PBPs, the specific roles of many types of PBPs are difficult to investigate individually and thus remain largely unclear.

While PBPs are shown to facilitate peptidoglycan polymerization directly, bacterial cytoskeleton proteins are also involved in determining cell shape. An actin homologue in bacteria, MreB is an essential protein that maintains the shape of many rod-shaped bacteria including *E. coli* and B. subtilis[160]. Depletion of MreB by treating with a drug A22, or a gene knockout will cause abnormal morphology. Certain bacteria have multiple set of MreB-like proteins[76], and sometimes carry redundant function in regulating cell shape. Specifically, cell will gradually grow into lemon shape after a few generations, and eventually lyse[53]. The MreB associate proteins, MreC, MreD, and other transmembrane proteins that interact with PBPs also have significant roles in determining rod cell shape, and are believed to be part of, or associated with the cell wall synthesis complexes.

Experimental observations suggest that PBPs and cytoskeletal protein MreB are not diffusively distributed on the cell membrane, but rather localize into organized features. Early studies of the MreB organization using fluorescent fusion with green fluorescence protein (GFP) tags suggested that MreB formed long ($\geq 1\mu$m), continuous helixes encircling the cell on the surface. However, a recent studies on MreB configuration challenged this view. Images of functional fluorescent fusions showed that MreB, as well as several kinds of PBPs form foci that distributed randomly on the cell envelope instead of long filaments in both *B. subtilis*[42, 51] and *E. coli*[150]. Moreover, these foci progressively translocate along the circumferential direction on the cell envelope, and the translocation depends on both transpeptidation and transglocylation activities[51, 150]. These results imply that the motion of the PBP complexes and MreB may correlate with the insertion of the peptidoglycan subunits. This hypothesis is supported by the agreement between the measured motion speed, foci density and growth rate in a quantitative model. Using electron cryotomography, Swulius *et al* argued that the native MreB in *V. cholerae* did not form long filaments longer than 80 nm[138]. The actual configuration of the cytoskeletal proteins and the

cell wall synthesis proteins are under debate. Concrete evidences for either hypothesis is still lacking

Since PBPs are recognized as the main cell wall insertion machinery, and they are observed to randomly distributed on the cell surface in *E. coli* and *B. subtilis*, the cell wall growth is expected to be dispersed as well. Experimental observations indeed show consistent results with the characteristic PBP distribution and motion patterns. The visualization of the peptidoglycan incorporation is first realized by labeling the PG precursors. Heavy isotope pulse-labeling[108] and D-Cys-labeling[35] showed a diffusive or patchy growth pattern in E. coli, while fluorescent labeling using ramoplanin-fluorescein and vancomycin-fluorescein in *B. subtilis* showed patchy or segmented helical pattern[145]. These insertion patterns support the picture that the moving PBP complexes facilitate new PG insertion, although direct correlation between growth and PBP localization is not available due to the limitations in spatial and temporal resolution of these techniques.

Even though the chemical component of the bacterial cell wall is known, the specific three-dimensional architecture how the peptidoglycan is organized geometrically remains elusive. For Gram-negative bacteria, the cell wall is less than 10 nm in thickness while the averaged glycan chain length is 20-35 nm in the case of *E. coli*[152], and therefore the configuration is likely a layered structure, where glycan strands align parallelly to the membrane. This glycan configuration is supported by NMR studies on short synthetic fragment[98], and further confirmed by electron cryotomography on isolated *E. coli* and *C. crescentus* sacculi[49]. This parallel arrangement appears to be consistent to the observation of lateral motion of MreB in *E. coli*, and the original "three-for-one" growth model proposed by Holtje *et al*, where three pre-made nascent strands replace an old strand on the cell wall mediated by a multi-enzyme complex[70] (figure 1.3). The high turnover rate of PG favors the "three-for-one"

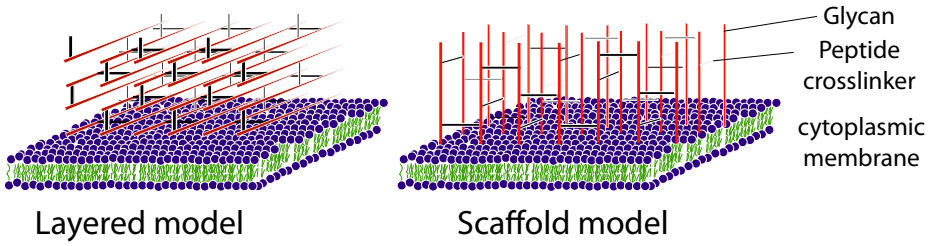

Figure 1.3: Two possible peptidoglycan architecture in thick cell wall of gram-positive bacteria. In the layered model shown on the left, glycan strands (red lines) align parallel to the cell membrane, whereas in the scaffold model in the right panel, glycan strands protrude perpendicularly to the cell membrane.

model over a simpler insertion scheme that one new strand is inserted between two strands on the wall[55, 107].

Gram-positive bacterial cell wall architecture is particularly elusive because of its larger thickness allows more possibilities to organize the peptidoglycan. It is both possible that glycan strands align parallel (layered) or perpendicular (scaffold) to the cell membrane (figure 1.3). NMR study on *S. aureus* sacculi showed that the glycan strands align parallelly one another, and peptide cross-linkers are nearly perpendicular to the glycan strands[125]. However, this result can not rule out either layered or scaffold configuration. While it is difficult to resolve the PG architecture using electron microscopy and NMR, limited information has been provided by AFM imaging on cell division planes[148], purified sacculi of *B. subtilis*[59], live *Lactococcus lactis*[4] and *Bacillus atrophaeus* spors[114]. These observations hinted that peptidoglycan on the surface of the cell wall organized into a banded structure parallel to the cell surface but perpendicular to the cell long-axis. Although whether peptidoglycan form hierarchical organization in these banded structure is still under debate.

Up to date, the scheme of inserting new PG into the thick gram-negative cell wall remains hypothetical. The most plausible picture is the "inside-to-outside" model proposed nearly three decades ago[81] based on the assumption that new PG insertion could only take place at the wall-membrane interface where the PBPs reside (figure 1.4). In this model, new material is inserted at the inner-most surface of the thick

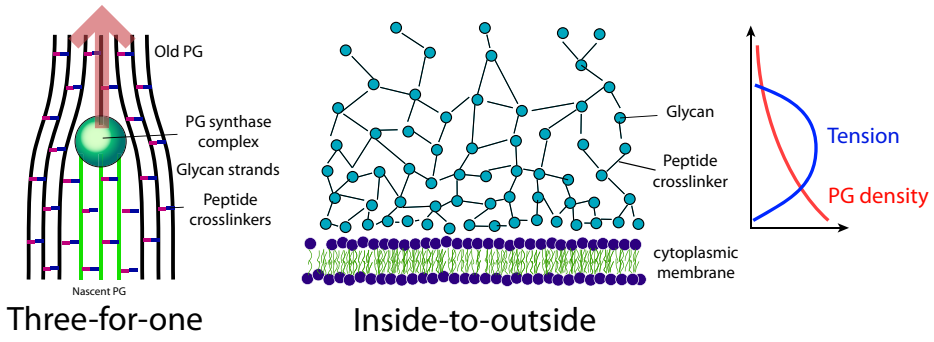

Figure 1.4: Peptidoglycan insertion models for both gram-negative and -positive bacteria. (a) "Three-for-one" insertion in single-layered gram-negative bacteria, where three nascent glycan strands replace one old strand in the PG network. (b) "Inside-to-outside" scheme for multi-layered cell wall. New PG is inserted at the innermost layer, pushing the old PG outwards while stretching more. (c) Schematic plot of PG density and tension distribution at various cell wall depth.

wall, and subsequently the old inner layers are pushed outward. During elongation, the nascent PG has a higher density than the existing PG, thus takes less or no tension, whereas the middle layers are fully stretched and bares the majority of the cell wall tension. As the layers are pushed outwards and the mesh is more stretched with increasing tension, more cross-lining peptides break due to autolytic activity or spontaneous hydrolysis. In the outermost layer, the cross-linking degree is minimum and cell wall bares no tension. The "inside-to-outside" growth model is consistent with the layered configuration, but again does not exclude scaffold configuration.

Quantitative growth models

Based on the proposed cell wall architecture and the localization of cell wall synthesis machinery, several quantitative growth models have been proposed recently in attempts to reenact cell wall growth of rod-shaped bacteria *in silico*. Jiang and Sun took a mean field approach, taking into account the balance between the chemical energy gain from incorporating new PG and stretching energy of the wall[73]. Their work predicted a mechanism that is able to maintain a robust radius during elongation, although mean field calculation can not provide insights to the local stability

against perturbation to the shape. Detailed heterogeneous growth dynamics was simulated on a down-scaled single-layered frame network[69]. There the peptidoglycan was described as a set of nearly parallel glycan hoops along the cell surface, and the strands were connected by peptide linkers to form a network. All bonds and joints are elastic, and are stretched under the turgor pressure. Insertion of new PG followed particular rules and gave rise to different types of growth. In summary, a random insertion with a insertion rate independent on the local cell wall density will cause positive feedback in growth upon small perturbation, and thus generate shape defects such as bending and bulging. Uniform insertion, however is able to maintain radius for several doubling cycles in length. Insertion that is spatially inhomogeneous instantaneously, but averages to a uniform distribution following larger-scale spacial order has similar shape effect to uniform insertion[48, 156]. Such spatial order can be an intact helix or several helical segments along the cell surface about the cell axis. Circumferential rotation can also serve as a global order to ensure uniform insertion in the averaged sense[150, 150], where long helical filaments are not required.

Observing cell wall growth in live cells

Insertion under spatial order at cellular length scale can give rise to ordered global growth pattern beyond simple elongation. For instance, when following helical insertion patter, the whole cell wall twists during elongation as shown in simulations[48]. Microscopically, the ordered helical insertion will also shear the growth of peptidoglycan at an angle to the circumferential direction. Even though recent observations question on the classical helical picture of cytoskeletal proteins such as MreB[138, 42, 51, 150], a local order such a preferred specific insertion angle is also able to give rise to global chiral growth pattern. The predictions of helical, or segmental helical insertion are experimentally verified by Wang *et al*[156], where two beads are attached on the surface of *E. coli*, and the motion of the two beads confirmed the

growth twist and turgor twist that indicate the chiral order of *E. coli* peptidoglycan. Similar growth twist was also found in gram-positive bacteria *B. subtilis*[156]. However, when working with the growth models of different bacteria, caution must be taken in distinguishing gram-positive and -negative bacteria, because the cell wall structure are essentially different even though related.

Although two-bead assay is able to reveal cell wall growth twist as opposed to a simple elongation, to understand the PG insertion rules better beyond the whole-cell scale, it is necessary to obtain a more detailed live cell growth map that pin points where material is inserted. With growth maps, cell wall growth dynamics can be studied at different levels. At sub-cellular scale, the growth rate is previously shown to be heterogeneous[17], with a more active growth in the mid-cell and inert polar caps. We want to ask the question how the growth rate distributes along the cell, in terms of both elongation rate and twist rate. At molecular level, the distribution and motion of cell wall synthesis complexes and cytoskeletal proteins are believed to directly relate to the cell wall growth, but it has not been directly proved. The colocalization of growth and the PBPs or cytoskeletal proteins would strongly support the above assumption. In addition, current quantitative cell wall growth models omit the PG turnover, which is also important in remodeling the cell wall architecture. The turnover can be indicated as negative growth in growth map, and that information will shed new light to correct the quantitative growth models.

In order to obtain detailed growth, I develop a novel fluorescent marker assay using nano-motion capture. High density of quantum dots (QDots) are covalently attached to the surface amine groups of the cell wall on gram-positive bacteria *B. subtilis* up to 2 QDots per square micrometer, comparable to the observed density of the PBPs and MreB. [51, 150]The motion of the fluorescent markers are resolved in three dimensions to reconstruct the material insertion and turnover pattern. Our results suggest that *B. subtilis* cell wall growth is twisted, compartmentalized and highly heterogeneous

in both space and time at sub-cellular level. We expect this assay to bridge the macroscopic cellular cell wall growth and microscopic molecular mechanism of PG insertion.

1.4 Summary and thesis outline

In Chapter 1, I introduce the background of bacterial cell mechanics, specifically cell turgor pressure and surface tension, and cell cell growth dynamics with current growth models. Two fundamental questions are brought regarding tension distribution and growth dynamics. Chapter 2 introduces the instrumentation of the tool, a home-built atomic force microscope I used to probe the cell mechanics. The work in this chapter is published as [38]. In Chapter 3, a special bulging *E. coli* strain was studied with AFM to show the results of the nonlinear elasticity and turgor pressure measurements. In Chapter 4, I introduce a novel assay to illustrate and quantify bacterial cell growth on gram-positive bacteria *Bacillus Subtilis*. The growth displays highly heterogeneous patterns in both space and time. Chapter 5 and Chapter 6 introduce new super-resolution optical microscopy technique and image analysis tools that are not only used in assisting the work in this study, but also find broader applications in biophysics, biology and neuroscience.

Chapter 2

Building Atomic Force Microscope to Probe cell Mechanics

Generally speaking, the mechanical property of an object can be obtained mostly directly from its geometric or rheological response to external mechanical perturbations. For biomolecules and cells, the mechanical interaction with the surrounding environment can be intrinsically generated by the cells themselves as those measured in traction force microscopy[13], or exerted externally by entropic force[74], optical force[23], viscous force of the surrounding media[120], or direct normal force from force probes[165]. Specifically in my study, the cell mechanical properties that I investigate, turgor and cell wall elasticity, both contribute to the overall cell stiffness under external bending force as discussed in [155] or compressive force[165]. Atomic force microscope (AFM) is a suitable tool to apply such forces while probing the geometric responses. Although AFM is mostly appreciated as an imaging tool to gain insights to micro- and nano-structures at both cellular and molecular levels[11], it is also a handy tool to manipulate micro-objects, and to apply a local force of typically 10^{-9} N to 10^{-7} N, which is relevant in biological processes at cellular level, onto

an area with a spatial scale of 10 nm, making it an ideal tool to probe mechanical properties such as object stiffness both *in vivo* and *in vitro*.

In this chapter, I describe the design and realization of the AFM I built for E. coli cell indentation experiments. Our AFM is specialized in the application to probe cell shape and stiffness, and one feature is that the AFM is built compatible with an inverted microscope and the probe has freedom in full three-dimensional motion. Since this AFM is not designed mainly for imaging, I followed [12] to design a digital feedback controller that is realized by computer and an analogue-to-digital converter instead of a faster hardware interface.

2.1 AFM construction

The key element of an AFM is a elastic cantilever arm, usually rectangular- or triangular- shaped, with a probe at the end. The tip can be made into different shapes and sharpness to fit in various applications. When subjected to external force, the cantilever arm will bend at a certain angle, which is optically amplified into a linear displacement and detected by a position detector, usually a quadrant photodiode (QPD) or a position-sensitive photodetector (PSD). The cantilever is mounted on a Z- or XYZ-piezoelectric state to control the position of tip and to apply force.

Our AFM was built in compatible with an inverted microscope (Nikon TE2000) for the combined functionality of both force microscopy and optical microscopy. It enables us to mechanically probe the sample while imaging it in optically simultaneously. The information from mechanical measurements can be obtained together with protein localization observations to precisely identify the mechanical structure in relation to the distribution of particular cellular component such as cytoskeleton. In addition to the combination of AFM and fluorescence imaging, both AFM tip and the sample stage have independent degrees of freedom to move in three dimensions.

The complete control over both specimen and AFM probe allows us to independently perform force measurement and take images with scanning techniques such as confocal microscopy or Stimulated-Emission-Depletion (STED) microscopy. Lastly, I developed our own control and analysis software package for maximum flexibility and extensibility. Beyond the basic indentation and imaging at any specific location, we are able to program complex and automated probing sequences in combination with computer vision analysis in realtime.

Motion Control

The major compromise of additional degrees of freedom to position the tip is the more demanding controlling effort due to the mechanical complexity. A simpler AFM design typically has a laterally fixed vertical scanner and the specimen stage is built on an x-y piezoelectric stage. The bandwidth of the cantilever vertical motion reaches kHz range, making it possible to probe sample in the tapping mode and to scan fast in the contact mode. In our setup, the full 3-D motion of the AFM cantilever is provided by three single-axis piezoelectric stages (Mad City Labs, OP-30). On top of that, I use a 3-axis manual stage to adjust the position in large scales (figure 2.1), which is useful to place the tip approximately above the specimen and in the field of view of the inverted microscope before fine positioning using piezoelectric stages. The mass on the piezoelectric stages and the mechanical stiffness set the upper limit for the bandwidth of the z-piezoelectric feedback loop at about 70 Hz. Even though slower than commercial AFMs, it is sufficiently fast for our purpose to investigate whole cell mechanics.

The motion of the MCL piezoelectric stages can be controlled in two methods at the same time. The stage controller has an internal digital to analogue (D/A) converter which is able to take digital controlling signal through USB port. One drawback of the USB control is that the exact time the computer writes USB port

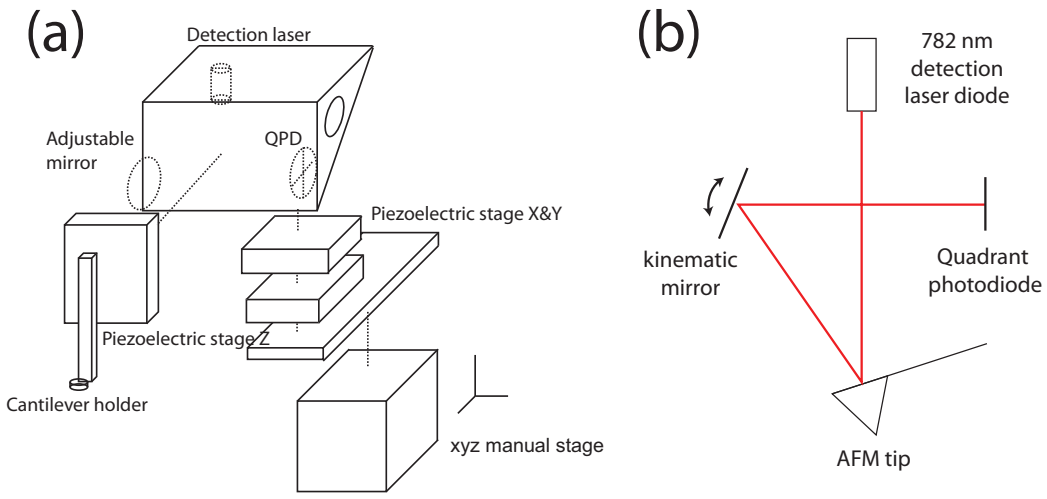

Figure 2.1: Schematic drawing of the construction of the AFM. (a) The cantilever is loaded on a commercial cantilever holder, which is mounted on the Z-piezoelectric stage. The Z-stage, detection laser diode, QPD and a kinematic mirror are fixed on the X&Y piezoelectric stage by a L-shaped adaptor and the whole setup is mounted on a XYZ manual stage for big-range adjustments. (b) The bending angle of the AFM cantilever can be optically detected. The laser diode and the mirror each has two degrees of freedom to rotate to align the detection beam paths.

is determined by the operating system and it is variable. The stage controller also takes direct control signal by an analogue input port and I connect it to the analogue output channel of the data acquisition board (National Instruments, PCIe-6251) to achieve timing precision in position control. The exact position of the cantilever can be monitored by a built-in sensor on the stage controller and is sent to the computer through an A/D converter on the NI-DAQ acquisition board. Sample stage positioning does not require precise timing in the applications in my thesis, thus USB port is sufficient for moving the sample slide.

Deflection Detection

The data collection and cantilever/sample stage control diagram is shown in figure 2.2. To detect the cantilever deformation, I use an optical lever to amplify the motion of the tip. The detection part includes a fiber-coupled diode laser (Bluesky Research, 781 nm wavelength, 28 mW maximum power), and a quadrant photodiode with built-

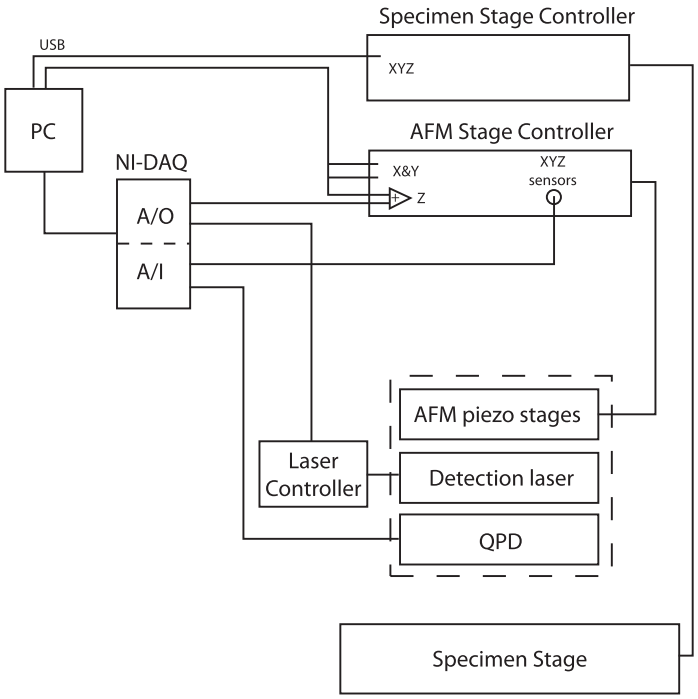

Figure 2.2: Schematic drawing of the control and data collection. Both specimen stage and AFM stage positions are controlled by USB ports, and an additional analogue signal is generated from the data acquisition interface and sent to the AFM tip z-position control for fast movement. The AFM tip height and the quadrant photodiode signals are collected by the same DAQ interface and are sent to the computer.

in amplifiers (Pacific Silicon Sensors, QP50-6-SD2). The laser from the fiber coupled diode is tuned to focus at onto the cantilever tip and the focused laser is reflected onto the QPD (figure 2.1). Because the exact cantilever tip location and angle may vary every time a new cantilever is loaded, the laser head is mounted on a kinematic mirror mount (Thorlabs VM05), and a kinematic mirror directs the reflected laser to the center of the QPD. Data I/O interface between computer and the instrument is achieved through a data acquisition board (National Instruments, PCIe-6251), and the signal is processed by the customized control software written in LabVIEW.

Sample chamber

The specimen is placed in a home-made sample chamber. The top of the chamber is left open for the cantilever access to the specimen, and I use a glass coverslip as the

bottom of the chamber, which is held above the objective of the inverted microscope by an aluminum chamber holder. An aluminum ring with rubber sealing serves as the wall to prevent leakage so that the coverslip is disposed and can be easily replaced after each use. The microscope stage also has a set of manual and piezoelectric x-y positioners, which enables the coarse and fine control of the specimen position. In our application, it is mainly used to select and place the specimen in place. Due to its large movement range of 200 μm, more than 7 times larger than the width of the field of view of the camera, it is also used to automatically switch fields in automated cell indentation experiments.

Optical Imaging

The fluorescence microscope base that the AFM is built on is fully capable for regular epi-fluorescence and total internal reflection fluorescent (TIRF) microscopy. The fluorescence excitation light source can be selected to be a halogen lamp or diode lasers with home-built controllers. Laser beam profile is cleaned with a 30 μm pinhole placed at the focal point of the beam expansion telescope. Fluorescence or bright-field optical images are acquired by an Electron Multiplying Charge Coupled Device (Andor Technology, iXon+ 897E EMCCD camera) with single photon sensitivity. If required, scanning imaging techniques, for example confocal or STED microscopy, can be implemented without changing the existing AFM setup. Since the space above specimen plane is occupied by the AFM, it is not applicable to use any imaging method that requires a condenser lens, such as differential interference contrast (DIC) or phase contrast microscopy. I use an LED as the illumination source to obtain bright field image.

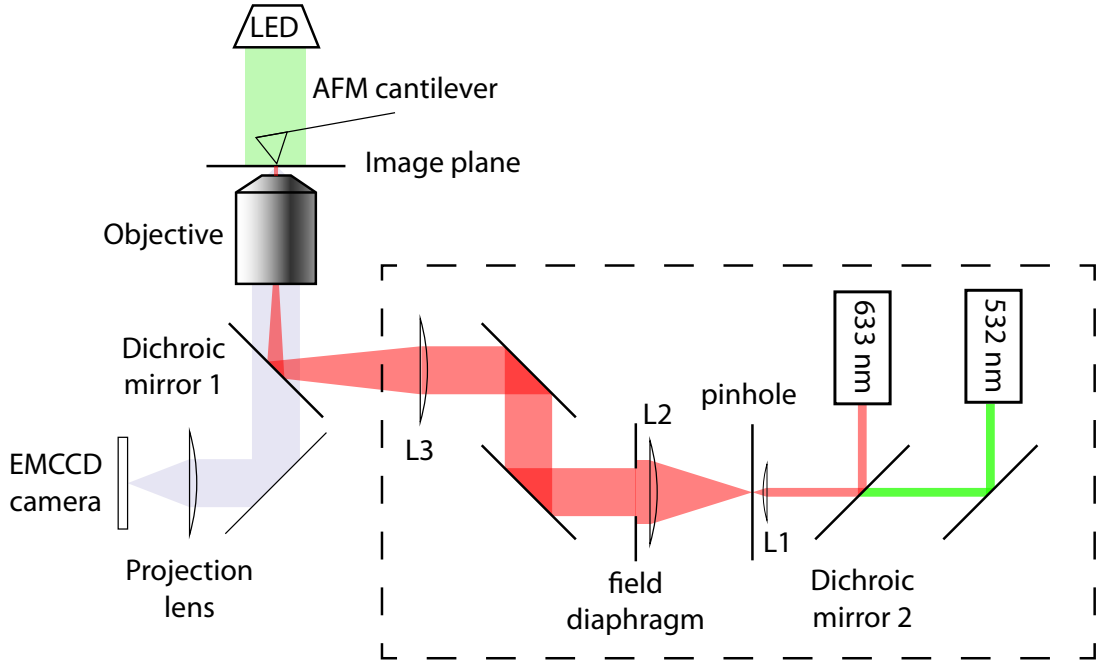

Figure 2.3: Fluorescence imaging diagram to show the combination of two-color fluorescence imaging and AFM force probing/imaging capability. Two laser beams at 532 nm and 633 nm wavelengths are expanded and collimated at the image plane. Total internal reflection fluorescence (TIRF) microscopy can be realized by moving lens L2. The laser excitation in the dashed line box can be switched to halogen lamp.

Control software

The controlling software of the AFM is written in LabVIEW based on the lower level hardware drivers of piezoelectric stages, NI-DAQ board and the iXon+ camera control. Higher level applications include feedback control of the deflection (force), cantilever landing, video tracking of the cantilever tip, automatic cell detection, scanning for topographical and stiffness map. The controlling software is particularly specialized in cell indentation related functions, including detecting the contact point (height of the surface), executing pre-programed or adaptive indentation sequence based on the surface topology and fluorescence images. These functions can be easily combined or extended to carry the specific tasks in various experiments.

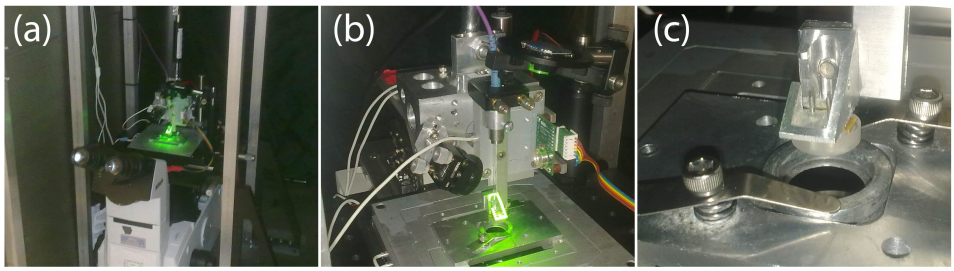

Figure 2.4: Pictures of the AFM. a) The whole setup including the AFM, the optical microscope and the EMCCD camera. b) AFM head including the translational stages and optical deflection detection elements. c) A close look of the specimen chamber, chamber holder and the cantilever holder.

In summary, the AFM consists of the following modules: mechanical-motion control, cantilever deformation detection, data acquisition, data processing (PC) and optical imaging. Pictures of The AFM at various levels of details are shown in figure 2.4.

2.2 Closed-loop feedback for constant force mode

An imaging AFM mainly operates in two modes: open-loop mode and constant force closed-loop mode. In the open-loop mode, a fixed height signal is sent to the z-positioner of the cantilever, so that the deflection or the force that cantilever applies to the substrate varies based on the surface topography. In contrast, closed-loop mode holds constant the force or equivalently the cantilever deflection by varying the z-position of the cantilever. Although open-loop mode is easy to implement and offers higher bandwidth, closed-loop mode is preferred in imaging the substrate topography, because it allows large height variation range and constrains the contact force at an optimal value to avoid damaging the sample or the cantilever tip.

Many feedback control applications adopt simple proportion-integral-differential (PID), but for our task, PID controller is not specially optimized to our instrument and will greatly limit the speed, and thus I seek more specific controller for better performance. The design of our controller mainly follows [12], a detailed "cookbook" for designing useful yet simple feedback controllers. More sophisticated approaches such as robust controller and adaptive controller may further improve the controller performance, but they are beyond the main functional requirements of our AFM and are not discussed in my thesis.

Control algorithm

In linear systems where different frequency components do not interfere, it is convenient to work in the frequency domain. Instead of the Fourier transform, Laplace transform

$$\mathcal{L}[y(t)] = \int_0^\infty e^{-st} y(t) dt \tag{2.1}$$

is conventionally used in control theory to convert signals in the time domain to the frequency domain. The two transforms are connected by setting $s = i\omega$. A signal $y(t)$ in the time domain is equivalently expressed in the frequency domain by its Laplace transformation $y(s)$. Here I have used the same symbol for the representations in two domains, since the argument of the function indicates the domain of the function without confusion. The behavior of a linear dynamical system can be fully characterized by its response to sinusoidal signals at all frequencies, namely the complex gain $G(s)$. For example, if the response of a system is given by $G(s)$, then for an input $r(s)$, the output $y(s)$ can be simply expressed as $y(s) = G(s)r(s)$. This relation is usually visualized by engineers as block diagrams shown in figure 2.5(a). The magnitude and phase of G as functions of frequency are called the Bode plots.

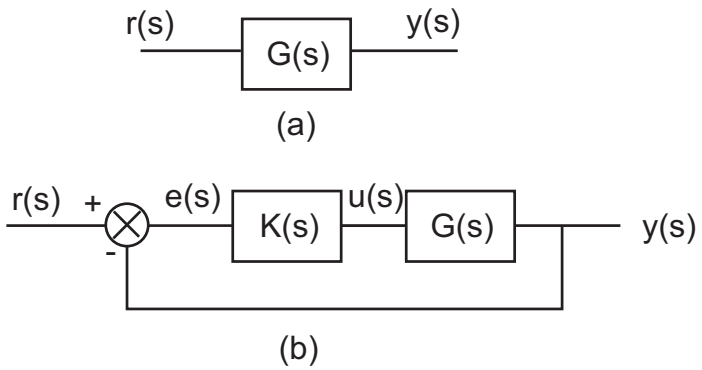

Figure 2.5: Block diagrams of (a) an open-loop system and (b) closed-loop feedback system. $G(s)$, $K(s)$ stand for system response and the controller response; $r(s)$, $y(s)$, $e(s)$ and $u(s)$ are the input signal, output signal, the error signal, and the controller output signal.

For our AFM working in the open-loop mode, the input is a position signal sent by the user (application), and the output is the deflection of the cantilever which depends on the height of the cantilever when it is in contact with the substrate. The deflection signal is related to the substrate topography in a nonlinear fashion due to the nontrivial interaction between the cantilever tip and the substrate. In contrast, for the closed-loop feedback mode, the input is a force, or cantilever deflection signal. A controller is inserted before the AFM to decide a proper position signal to sent to the AFM so that the force or cantilever deflection has desired dynamics with respect to the input force signal, for example a constant value in the contact scanning mode. Consider the block diagram shown in figure 2.5(b), where the output signal $y(s)$ from the system $G(s)$ is compared with the input signal $r(s)$ and the difference $e(s)$ is used to compute the proper input $u(s)$ for $G(s)$. The conversion from the error signal $e(s)$ to the actual driving signal $u(s)$ is what I need to design, namely the controller $K(s)$. It can be shown that the response of the closed loop is

$$y(s) = \frac{K(s)G(s)}{1 + K(s)G(s)} r(s). \tag{2.2}$$

Define the open-loop gain as $L(s) \equiv K(s)G(s)$, and the closed-loop gain becomes

$$T(s) = \frac{L(s)}{1 + L(s)}. \tag{2.3}$$

From this expression, it is apparent that a large $\|L\|$ in general results in a T close to identity, which is essentially the goal of the closed-loop feedback in constant force mode. However, if $L(s)$ approaches to -1 on the complex plane at a particular frequency s, $T(s)$ diverges and the system becomes unstable at $L(s) = -1$. The rules of designing a controller $K(s)$ becomes clear: to have $\|L\|$ large while keeping it far away from -1 on the complex plane.

According to equation (2.3), I can construct the controller $K(s)$ given the system response $G(s)$ and the desired closed-loop response $T(s)$:

$$K(s) = \frac{T(s)}{1 - T(s)} G^{-1}(s). \tag{2.4}$$

If I choose the open-loop response $T(s)$ to have a simple single-pole low-pass form

$$T(s) = \frac{1}{1 + s/\omega_0}, \tag{2.5}$$

the controller becomes

$$K(s) = \frac{\omega_0}{s} G^{-1}(s). \tag{2.6}$$

The next step is to convert the analytical form of $K(s)$ into digitized form to apply on the computer, which is achieved by the "z-transform" defined as $z \equiv e^{sT_s}$, where T_s is the sampling interval of a continuous signal. Multiplying a transform by z correspond to a shift of T_s in the time domain, and multiplying z^{-1} means delay by T_s. The conversion from s to z is given by Tustin's transformation[43]

$$s \to \frac{2}{T} \left(\frac{1 - z^{-1}}{1 + z^{-1}} \right). \tag{2.7}$$

Consider the delay caused by the zero-order hold[12], the digitized controller is written as

$$D(z) = (1 - z^{-1})\frac{K[s(z)]}{s(z)} \tag{2.8}$$

$$= \frac{B_0 + B_1 z^{-1} + B_2 z^{-2} + \cdots}{1 - A_1 z^{-1} - A_2 z^{-2} - \cdots}. \tag{2.9}$$

Also note that $D(z) = u(z)/e(z)$, I obtain the final form of the controller

$$u_n = A_1 u_{n-1} + A_2 u_{n-2} + \cdots + B_0 e_n + B_1 e_{n-1} + B_2 e_{n-2} + \cdots , \tag{2.10}$$

where u_n is the n^{th} output (newest) and u_{n-i} are the previous outputs, and e_j is the j^{th} error.

Measuring the transfer function

Since the controller is designed based on how the system responds to the control signal, we need to know the specific transfer function of the system, $G(s)$. The measurement of the complex transfer function is normally done with a lock-in amplifier. Since the typical time scale is much slower than milliseconds, it is possible to measure the transfer function directly with the NI-DAQ board at sufficient accuracy. To measure the complex gain at a frequency f, a sinusoidal waveform at frequency f is uploaded to the A/O channel, which writes to the analogue input of the piezoelectric stage controller. At the same time, both the deflection signal from the QPD and the control signal are measured and recorded by A/I channels. The two signals are Fourier transformed, and the ratio of the complex amplitudes gives the magnitude gain and the phase lag of the output signal with respect to the input control signal. This procedure is repeated at various frequencies to quantify the response in a wide

range of spectra. The resulted magnitude and phase Bode plots are shown as the red dotted lines in figure 2.8.

The profile of the complex gain captures the common feature of a low-pass (LP) filter where the output magnitude decreases with increasing phase lags as the frequency of the input signal increases. It is expected to observe an overall low-pass type of profile because the piezoelectric stage internally runs a closed-loop feedback that is tuned as a LP filter. On top of the overall LP feature, I observe two major and one minor resonance peaks, with the lowest resonance peak centered around $72Hz$. Experimentally I observed that increasing the mass of the moving parts on the AFM head will shift the resonance peak to lower frequency. The mechanical stability could be improved by decreasing movable parts at costs of flexibility usability. I compromised the stability, and thus limited the bandwidth for the full three-dimensional motion of the AFM head.

Model of the Mechanical Vibration

To parameterize the transfer function, first consider a simple mechanical setup where a massive block m is attached on another base block M, which is connected to a fixed point by a spring of force constant k and damping coefficient γ (figure 2.6). The positions of the two blocks are labeled as x_1 and x_2. In this model, the input is the relative displacement between the two blocks $x_1 - x_2$, in analogous to piezoelectric in the z-axis driving the relative motion between the AFM head and the cantilever. The output is the absolute displacement of the small block x_1, in analogous to the distance between the tip and the spatially fixed sample. The equations of motion of the two blocks are written as the following:

$$M\ddot{x}_2 = -\gamma\dot{x}_2 - kx_2 + f; \tag{2.11}$$

$$m\ddot{x}_1 = -f, \tag{2.12}$$

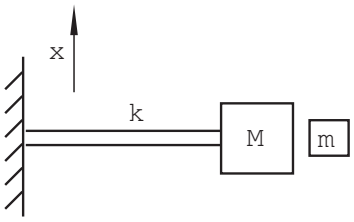

Figure 2.6: Schematic drawing of the mechanical model. The mass of the two blocks are labeled as m and M, with displacements x_1 and x_2. M is attached to a fixed point by an elastic spring with spring constant k. The dynamics of M and m is driven by the relative motion between them.

where f is the force block m exerted on M. Write the stable oscillatory solution as

$$x_j = A_j e^{i\omega t}, \tag{2.13}$$

where j takes value of 1 or 2. Substitute in the equation (2.12), we can show that the two complex amplitudes are in the following relation:

$$A_1 = \frac{1}{m\omega^2}(-M\omega^2 + i\gamma\omega + k)A_2. \tag{2.14}$$

The transfer function $G(s)$ can be calculated as

$$\begin{aligned} G &= \frac{A_1}{A_1 - A_2} && (2.15)\\ &= \frac{-M\omega^2 + i\gamma\omega + k}{-(M+m)\omega^2 + i\gamma\omega + k} && (2.16)\\ &= \frac{\alpha(s/\omega_0)^2 + \beta s/\omega_0 + 1}{(s/\omega_0)^2 + \beta s/\omega_0 + 1}, && (2.17) \end{aligned}$$

where I have defined new parameters $\omega_0 = \sqrt{k/(M+m)}$, $\alpha = M/(M+m)$ and $\beta = \gamma\omega_0/k$ in addition to $s = i\omega$. Now the transfer function is fully characterized by three parameters α, β and ω_0 resembling the reduced load, the damping, and the resonance frequency. Figure 2.2 shows the Bode plot of a typical parameter set $\{\alpha = 0.9, \beta = 0.05\}$ as a function of the scaled frequency $|s/\omega_0|$.

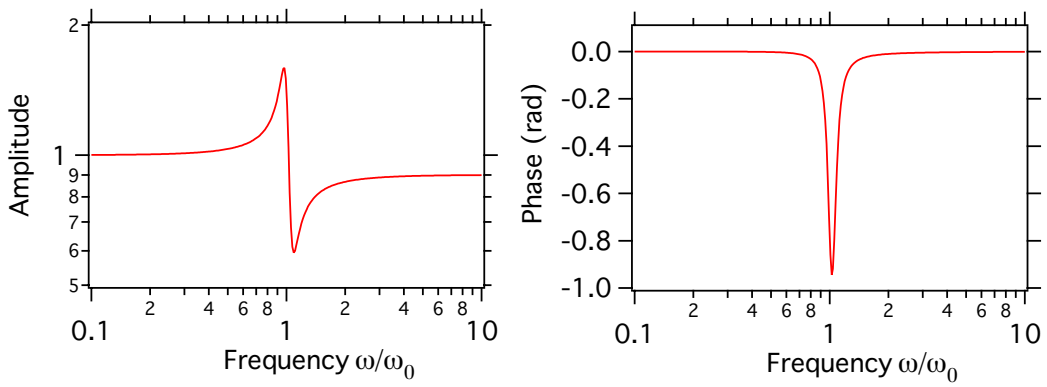

Figure 2.7: Typical Bode plots of the dynamical model in equation (2.12). The parameters are set as $\alpha = 0.9, \beta = 0.05$. The magnitude has a clear resonance peak and the phase has a lag at the resonance frequency but is flat away from the resonance frequency.

Compare the Bode plot of the model with the transfer function I measured previously, we can see that the model captures the feature of the resonances, except that more than one resonance peak exists. The two major and one minor peaks are generated because the piezoelectric stages in x- and y-direction are built on top of each other, and each of them has a resonance mode as described above, and the coupling between the two eigen modes gives rise to new modes at new frequencies. I assume that for each mixed mode, the expression in equation (2.17) still holds but with different parameter values. The base line of the system transfer function is captured by a second order roll-off function. The overall transfer function therefore can be written as

$$G(s) = G_0 \frac{1}{(1 + s/\omega_a)(1 + s/\omega_b)} \cdot \prod_j \frac{\alpha_j (s/\omega_j)^2 + \beta_j s/\omega_j + 1}{(s/\omega_j)^2 + \beta_j s/\omega_j + 1}. \tag{2.18}$$

To simplify the controller, I only include the two major resonance peaks and the minor peak is omitted. It is a reasonable simplification because simpler controller is more robust against changes in the mechanical character, such as mass, damping and spring constants. I fit the measured transfer function shown in the Bode plot with the functional form in equation (2.18), and list the fitting parameters of the

Table 2.1: Fitting parameters in the second order low-pass, two-resonance model of the transfer function.

G_0	6.18
ω_a	447.0 rad/s
ω_b	447.0 rad/s
ω_1	449.9 rad/s
α_1	0.9308
β_1	0.03309
ω_2	917.8 rad/s
α_2	0.9552
β_2	0.02269

model in table 2.1. Figure 2.8 shows the modeled transfer function (blue line) and the measured transfer function (red dots).

Controller realization

After the functional form of the transfer function $G(s)$ is obtained, the controller is realized following the procedure stated in the previous sections. Since I placed two extra poles to capture the low-pass feature in $G(s)$, the form of $K(s)$ calculated by equation (2.6) diverges at $s \to \infty$. To address this, I also add two poles to the controller:

$$K(s) = \frac{\omega_0}{s} G^{-1}(s) \frac{1}{1 + s/\omega_a} \frac{1}{1 + s/\omega_b}. \tag{2.19}$$

To simplify the controller, I chose $\omega_a = \omega_1$ and $\omega_b = \omega_2$. The new poles cancel the zeros brought in by $G^{-1}(s)$ term and they put an upper limit of the controller bandwidth roughly at $70Hz$. This bandwidth is good enough to meet our requirement in simple linear scan and locating the surface height of the substrate. Finally, equation (2.9) converts it to the digitized version. Considering the bandwidth limit of our controller and the reliable output rate of the NI-DAQ board, I set the digital sampling-control loop rate at $1kHz$, or equivalently $T_s = 1$ ms. The form of the controller is

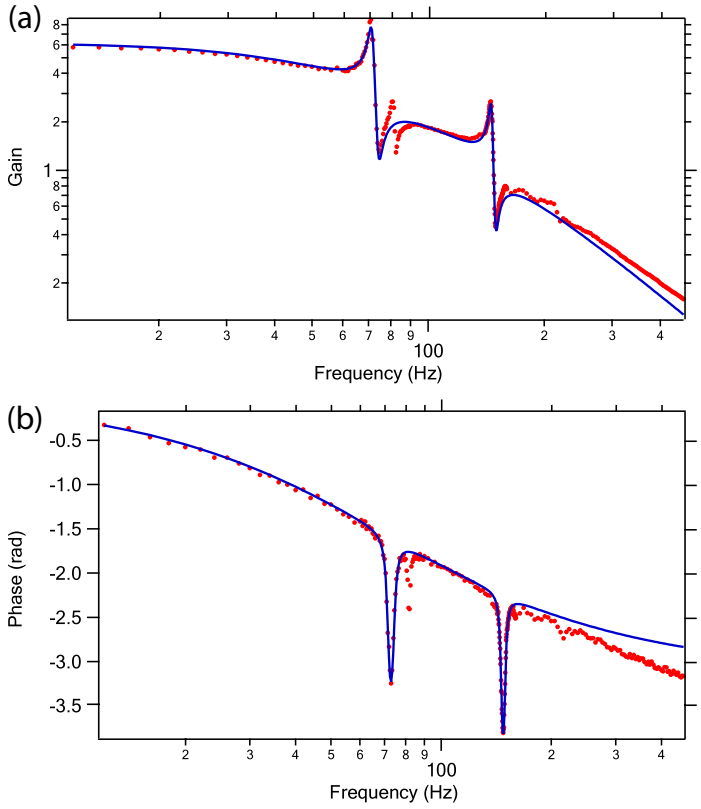

Figure 2.8: Experimental transfer function shown in the Bode plots (red dots) and the fit with two eigen modes (blue curves). The transfer function is characterized by a second-order low-pass profile and two major resonance peaks at 72 Hz and 133 Hz.

Table 2.2: The calculated constants used in the digitized controller of loop rate $1kHz$.

A_1	4.046	B_0	1.796×10^{-4}
A_2	-7.268	B_1	-5.546×10^{-4}
A_3	7.217	B_2	7.704×10^{-4}
A_4	-3.963	B_3	-5.458×10^{-4}
A_5	0.968	B_4	1.741×10^{-4}

expressed as follows:

$$u_n = \sum_{i=1}^{5} A_i u_{n-i} + \omega_0 \sum_{j=0}^{4} B_j e_{n-j}, \tag{2.20}$$

The parameters of the digitized controller are listed in table 2.2. The parameter ω_0 is left out from the table because in experiment it can be used as a quick adjustment to balance between bandwidth and stability. In practice this value is set to values between 200 and 500, corresponding to a bandwidth of 31 Hz to 80 Hz.

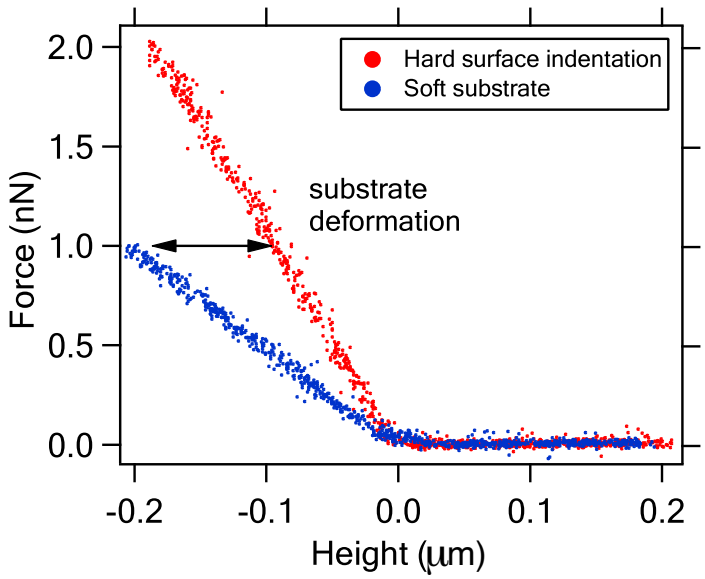

Figure 2.9: A typical indentation curve on hard surface (blue circles) and on *E. coli* (red circles). The indentation speed is set to $200nm/s$ and the indentation range is $400nm$. Both curves show linear force-indentation relation, and the difference in the slopes measures the stiffness of the cell given cantilever stiffness.

2.3 Cell Indentation

The main function of our AFM is to probe the cell stiffness by indenting the cell body, and correlate the indentation force and the deformation of the cell following the sequence described below. First, the cantilever is moved above the substrate or a cell, then is lowered until the deformation of the cantilever reaches a threshold (typically 10 nm). After the height of the surface is detected, the cantilever is programmed to drop and then rise at constant speed (typically 100-1000 nm/s) around the surface height, while the height of the cantilever and the deflection signal are recorded at 1 kHz.

The QPD deflection signal as a function of the cantilever height is called the indentation curve. The typical indentation curves on hard surface, usually glass substrate, and on *E. coli* are shown in figure 2.3. Before the cantilever is in contact with the surface, the deflection remains constant. After contact, the deflection is linear with the height of the cantilever for linear elastic material. The deformation of the hard

surface is negligible compared with the cantilever bending, thus the hard surface indentation curve serves as deflection-deformation calibration to give displace-deflection conversion factor in unit of μm/V. On the other hand, because the indentation force is proportional to the cantilever deformation or the deflection signal on the QPD, the slope of the indentation curve on a elastic substrate consequently measures the effective spring constant of the cantilever and the substrate in series. Denote the spring constants of the cantilever and the substrate as k_c and k_s, and the effective spring constant of the two in series k_e. From the relation $k_e^{-1} = k_c^{-1} + k_s^{-1}$, k_s in unit of k_c can be written as

$$k_s = \frac{1}{k_c/k_e - 1} k_c. \tag{2.21}$$

In this relationship, k_c/k_e can be conveniently replaced by the ratio of the indentation curve slope on the hard surface κ_{surf} and the slope on the sample κ_{smpl}, because the deflection measurement sensitivity does not depend on the substrate stiffness. In summary, given the cantilever stiffness k_c, sample indentation slope κ_{smpl} and hard surface indentation slope κ_{surf}, the linear indentation stiffness k_s is

$$k_s = \frac{k_c}{\kappa_{surf}/\kappa_{smpl} - 1}. \tag{2.22}$$

The interpretation of the stiffness information obtained from the indentation curves depends on the specific cell stiffness model. A popular quantification of both eukaryotic and bacterial cell stiffness is the Hertz model, where the cell is approximated as a solid elastic object with Young's modulus E as the only stiffness parameter[106]. The linear indentation stiffness depends on both E and the geometry of the cantilever tip, and is predicted to be a nonlinear power law relationship. Another model assumes that the cell shape is maintained mainly by the turgor pressure and the cell membrane and cell wall serves as a elastic envelope[165, 5]. The indentation stiffness in this model is mainly determined by the turgor pressure, and

the geometry of the cantilever is also essential in determining the functional form of the indentation curve[5]. In chapter 3, I discuss the limitations of the above models in details, and introduce a new mechanical model for bacterial cells. With a special bulging strain of *E. coli*, we overcome the difficulties that previous models have addressed poorly.

Chapter 3

A Passive Adaptive Strategy to Distribute Tension: Nonlinear Elasticity of Bacterial Cell Wall

Bacterial mechanics and morphology is essential to many physiological function including motility, division, nutrient access as discussed in Chapter 1. To recapitulate, the major mechanical elements in a bacterial consist of a relatively rigid cell wall, also called murein, or sacculi if purified from cell culture, and the turgor pressure that pushes the cytoplasmic membrane against the cell wall to inflate it. The cell wall is made of cross-linked peptidoglycan polymer, and is essential to define the cell shape and to maintain the physical integrity of the cell. Turgor pressure is the osmotic pressure generated by the solute concentration difference across the cytoplasmic membrane. Bacteria have a set of transporters and channels to regulate a positive turgor pressure, in order to maintain certain internal chemical environment. In addition, higher than normal pressure endangers the cell integrity. On the other hand, plasmolisis can take place at lower pressure, and potentially damage the membrane and periplasmic proteins.

Cell wall is built strong to serve as the main tension baring element, yet many channels and transporters operate based on the membrane tension. The distribution of the tension among cell wall and tension is a delicate balance between cell wall protection and membrane tension measurement sensitivity. The specific cell wall and membrane elasticity, together with the turgor pressure determine how much tension each layer of the cell envelope takes. In this chapter, I introduce our measurement of the cell wall elasticity and bacterial turgor pressure in *E. coli*, and discuss how the nonlinear elasticity serve as a passive adaptation strategy to distribute tension on cell wall and cytoplasmic membrane.

Both cell wall elasticity of different bacteria and turgor pressure have been measured in various ways. As the most straightforward approach, pure murein sacculi can be extracted and purified for mechanical measurements. In the bulk studies, large amount of murein sacculi was extracted from cell culture and form a thread in the macroscopic scale for mechanical studies in classical methods[144]. The purification of murein sacculi involves boiling in detergent SDS and ultra centrifugation. Usually after intensive centrifugation the sacculi are compressed into double-layered thin sheets. Yao *et al.* measured the Young's modulus of single sacculus sheet deposited on grids at hydrated condition as 25 MPa, similar to that of rubber, and a significantly higher value of 300 to 400 MPa under dry condition[165].

Cell mechanical property can be studied under more relevant conditions on live cells. At the spatial scale of a bacterial cell, optical tweezers and atomic force microscope are able to exert localized force onto single cells. Because forces generated by optical tweezers are usually below 100 pN, it has been only applied to stretched a helical-shaped bacteria without cell wall[95]. AFM instead is more suitable in terms of applying larger forces on the cell to generate observable deformation. Several studies have successfully measured the whole cell stiffness with AFM and are briefly reviewed in the next section.

3.1 Models of cell surface stiffness

When AFM is used to probe the stiffness of a substrate, the cantilever tip is pushed against the substrate. The normal force will both bend the cantilever and deform the substrate. Given the cantilever stiffness k_c, the substrate stiffness for that particular tip shape can be calculated from the relative change in the shape of the cantilever and the substrate. Typically when such stiffness measurement is performed, the bending angle of the cantilever is recorded as a function of the controlled position of the cantilever in Z. The height of the contact point and the relative stiffness can be extracted from the turn point and the slope of the indentation curve. One special indentation curve is obtained from the hard-surface indentation where the deformation of the substrate is negligible. From this trace, the relation between the cantilever optical deflection and the actual tip movement in Z is calibrated, and therefore the force can be calculated from the cantilever force constant (figure 2.3). Let the slope of the hard-surface indentation curve be s_0, and the slope on an soft substrate s, the substrate force constant is

$$k_s = \frac{k_c}{s_0/s - 1}. \tag{3.1}$$

The force constant on the substrate, a cell or part of a cell in our case, gives the relative quantification of the mechanical property. However, the stiffness strongly depends on the shape of the probe. More general properties of the cell such as cell wall elasticity and turgor pressure are not explicitly indicated from the force constant. Several mechanical models of bacterial cell have been proposed to extract these more general parameters.

3.1.1 Elastic solid model

A model that is frequently referred to in the AFM literature is the Hertz model[83]. It originally describes the deformation of two elastic spheres when they are pushed

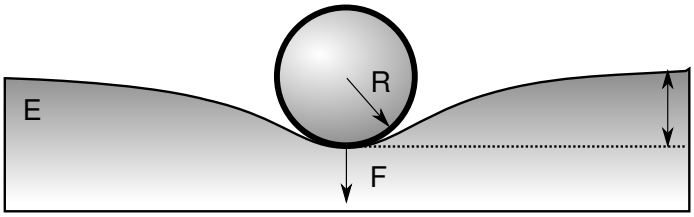

Figure 3.1: In the Hertz model, the cantilever tip is represented by a rigid sphere and the the cell is modeled as an infinitely large flat substrate filled with elastic material. The Hertz model is originally aimed to solve the deformation of two elastic spheres pressed into each other.

against each other. When applied in AFM system, the Young's modulus of one sphere is taken as infinity to represent the cantilever tip and the radius of the other one is assumed to be infinity to represent the soft substrate (figure 3.1). The applied force F and the deformation δ are nonlinearly related as

$$F = \frac{4E}{3(1-\nu^2)}\sqrt{R}\delta^{3/2}, \tag{3.2}$$

where E is the Young's modulus and ν is the Poisson ratio. The limitation of Hertz model is readily seen: the interior of a cell is viscous rather than elastic. The strain is uniformly distributed as the turgor pressure instead of elastic strain.

3.1.2 Inflated thin shell

More realistically, the cell structure is viewed as an inflated thin shell. The force resulted from the deformation have three main contributors: the intrinsic surface tension due to the positive turgor pressure P, the local stretching deformation, and the bending of the cell wall. In Gram-negative cells, the cell wall thickness is less than 10 nm. For this reason, the bending rigidity of the cell wall is neglected. The shape of the indenter is usually modeled as a cone with a spherical tip of finite radius r_t.

Yao's model

Yao *et al.* modeled the shape of the indentation curve in the framework of the inflated thin shell[166]. In their model, the indentation is shallow and the tip radius r_t is large so that the radius of the contact area between the tip to the cell wall r_c is small. Under the applied force F, the depth of the indentation created by the tip from the bottom to the edge of the bowl is

$$h = \frac{F}{2\pi P R_b}\left\{ln(\gamma) + \frac{1}{\gamma} - 1\right\}, \tag{3.3}$$

where R_b is the effective radius of the bacterium and $\gamma = (R_b/r_t)+1$ (figure 3.2). From this relation, it is apparent that the deformation is proportional to the applied force, therefore yield a linear force-indentation relation different from the Hertz model. Yao *et al.* also argued that because the Young's Modulus of the cell wall is relatively large, the global effect of the flattened top and bottom is minor compared to h. Nonetheless, they approximate the top and bottom deformation f as $\frac{F}{2\pi P R_b}$. They then further omitted the flattened deformation at the bottom because it was assumed to attach to the substrate before the AFM tip compressed the cell, and therefore the height change was even smaller. The overall effective force constant is

$$k = \frac{F}{h+f} = \frac{2\pi P R_b}{ln(\gamma) + 1/\gamma}. \tag{3.4}$$

Arnoldi's model

Another analytical result of the local indentation caused by the cone-shaped cantilever tip on the inflated thin shell was made by Arnoldi *et al.*[5]. The energy functional was minimized so that the profile of the shell was solved under particular force. For

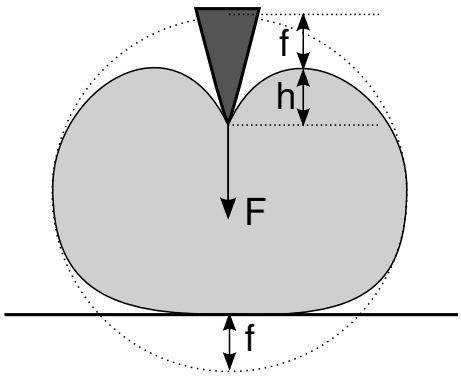

Figure 3.2: The cell is modeled as an inflated thin shell[5] or a fluidic membrane[165], and the AFM indentation created by a conical indenter under external force F has contributions from the global deformation f and the dent depth h.

small force, the indentation is linear with the applied force with a force constant

$$k = \frac{3\pi}{2} P R_b \phi(\rho/d), \tag{3.5}$$

where ρ is the radius of contact area between the cantilever tip and the cell, and d is the length scale on which the deformation relaxes to zero. ϕ is a geometric factor $\phi(\rho/d) = \rho K_1(\rho/d)/(dK_0(\rho/d))$, where K_0 and K_1 are modified Bessel's functions.

In this model, Arnoldi *et al* specifically discussed that the bending energy was negligible compared with the work against the membrane tension and the stretching energy, when the turgor pressure generated a large surface tension and the indentation was small. In fact, the ratio of the tension energy and the bending energy in their model was estimated as $\kappa = PR_b^2/Et^2$, where t is the thickness of the cell wall. In the case of a live *E. coli* cell, κ is in the order of 50. In some of our experimental conditions such as under a high external osmotic pressure or in bulging cells, these requirements are not always satisfied. Even in live cells, due to the possible stress stiffening effect, the Young's modulus can be substantially bigger than the strain-free values; therefore the bending energy may be underestimated in all conditions.

3.1.3 Hollow tube compression

In both Arnoldi and Yao's models, the bending energy was ignored. In the other extreme case when the turgor pressure reduces to zero, the cell wall forms a hollow tube and the compressibility falls to another category. For a long tube of radius R_b, wall thickness t, and Young's modulus E, the effective force constant under a point force is

$$k \propto Et^{5/2}/R^{3/2}, \tag{3.6}$$

with a proportional constant approximated equal to 1. This model was used to obtain the microtubule rigidity[34] and is suitable to describe a deflated bacterial cell wall.

3.1.4 Elastic filament

The mechanisms that eukaryotes use to maintain the shape are different from prokaryotes in principle. Actin network, microtubules and other cytoskeletal structures define the eukaryotic cell shape and provide cell motility and intracellular trafficking. Recently, cytoskeletal proteins in the bacterial world are identified and speculated to play a direct role in cell mechanics. It has been shown that fluorescently labeled actin homologue MreB assembles into helices in most rod-shaped cells including *E. coli*. The *in vitro* polymerization of MreB yields long and straight filaments or bundles of filaments[149]; similar assembly was observed for the MreB expressed in fission yeast[132]. These observations suggest that MreB form bundles that may act like its eukaryotic homologue actin. Wang *et al* showed that MreB could contribute up to 50% of the whole bending rigidity in filamentous *E. coli*[155]. It is also argued that MreB must bind to the cell envelope in order to create such dramatic change in cell bending stiffness.

The helical MreB configuration is challenged by several observations with fluorescence microscopy and electron microscopy[138] (also discussed in Chapter 1). In

accordance, our experiments on specifying the contribution of MreB had negative results. In our measurement, cells treated with A22, a drug that is able to disassemble MreB within minutes, had no observable effect on the cell indentation stiffness. How bacterial cytoskeletal proteins alter the indentation stiffness remains elusive, and its contribution is omit in the following analysis in this chapter.

3.1.5 Cell wall stiffness and turgor pressure are not independent

A realistic bacterial cell is far from a solid elastic body, an inflated fluid bubble, or a hollow elastic tube. The closest picture is close to an inflated bubble, but enclosed with an elastic shell. Under external mechanical perturbation, both turgor and cell wall contribute to the overall restoring reaction, e.g. linear cell stiffness in case of AFM indentation. Two technical difficulties must be resolved in order to quantify cell wall elasticity and turgor pressure: firstly, their contributions need to be separated somehow using only linear indentation; and secondly a realistic indentation model on the inflated shall is required.

Moreover, cell wall elasticity may not be independent from the turgor pressure, which is why studying purified sacculi is not sufficient to resemble the mechanics in live cells. It is well known in polymer physics that the elastic modulus of the material depends on the loaded strain[135]. As early as the 19 century, it has been documented that the elastic moduli of blood vessel wall increases as it is strained. Similar behavior can be observed in blood vessels[6], cornea[65], blood clots[124], neuronal filaments[84] and actin networks at cellular scale[71, 162, 90]. The nonlinear relation between elastic modulus and strain is named stress stiffening, strain stiffening or strain hardening. It is natural to speculate that the peptidoglycan polymer has this property; *i.e.* the stiffness of the cell wall depends on the stress caused by the turgor pressure. This idea was examined on B. subtilis by Thwaites *et al*[144], where the

nominal stress was measured on a bulk of *B. subtilis* murein sacculi as the applied stress changes. Thwaites *et al* pointed out that the nominal stress does not grow linearly with the applied strain. There is no direct evidence of the stress stiffening of PG in live cells under physiological conditions.

Stress stiffening can be resulted from several mechanisms at different spatial scales. In a thermal environment, the competition between external stress and entropy results in a highly nonlinear force-extension relation that has been modeled as worm-like chain (WLC) or freely-jointed chain (FJC)[23, 46]. The nonlinearity in these building blocks is a microscopic mechanism of stress stiffening. Consequently at a more macroscopic scale, the the geometric configuration or the cross-linking polymer network may change depending on the overall strain, thus change global elasticity. Even if all the chains still remain in the linear regime, the structural configuration of these linear springs is still able to generate a macroscopically nonlinear elasticity. Boulbitch *et. al.* modeled the PG network as a hexagonal mesh of rigid glycan subunits and elastic peptide cross-links. They predicted a power–law relationship between the axial elastic modulus and stress with a stiffening exponent of ~ 1 [19].

3.2 Indentation on bulging *E. coli*

3.2.1 Cell bulges separate the turgor and cell wall

In a live cell where both turgor pressure and cell wall support the cell shape, it is hard to quantify them separately from one indentation trace. This difficulty is solved in a *E. coli* strain with mutated gene *imp4213* that is sensitive to vancomycin and able to form spherical inner membrane bulges[118] (figure 3.3). The bulging cell brings the unique capability to quantify the turgor pressure and the cell wall separately. The idea is that the inner membrane bulge is not armored with the cell wall, whereas the combined contribution of the cell wall and turgor can be obtained from cell measure-

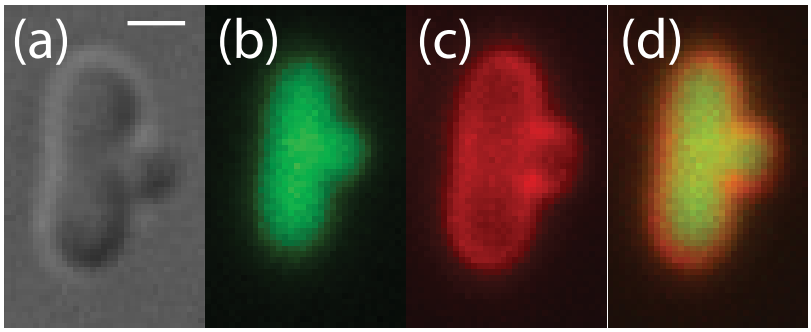

Figure 3.3: The images of a typical inner membrane on a vancomycin treated *imp4213* strain of *E. coli* carrying plasmid pWR20 to show the cytoplasm. Cells were treated in vancomycin for 40 minutes under 37°C and a 10-20% population of the cells form inner membrane bulges. a) differential interference contrast (DIC) image of a bulging cell, b) cytoplasmic GFP, c) FM4-64 membrane staining images indicate the cytoplasm and the cell membrane.

ments. Briefly, we first obtain the turgor pressure of individual bulging cells from the bulge radius and indentation stiffness using AFM and fluorescence microscopy [Fig. 3.4(a-e)]. Then, from the size and stiffness of the cell body, we are able to extract the elasticity of the cell wall under tension using numerical methods. The variation in turgor pressure among bulging cells allows us to probe the mechanical properties of the PG over a broad range of stresses. Additional experiments using non–bulging cells yields the turgor pressure and wall modulus of *E. coli* under physiological conditions.

The bulging *E. coli* strain we use is derived from the K12 wild-type strain and contains a mutation, *imp4213*, that increases the outer membrane permeability to allow small molecules to enter the periplasmic space [122, 44, 69]. *lptD* (*imp*) gene codes for a outer membrane protein that selectively transport material to the periplasmic space, while providing some drug resistance. *imp4213* is a frame deletion of a transmembrane alpha helix motif from *lptD*, resulting in an increased membrane permeability. We then use vancomycin, a drug that inhibits PG subunits from forming peptide cross-links, to generate a small number of local fractures in the cell wall. Under turgor pressure, the cytoplasm pushes the inner membrane through the frac-

ture and forms a membrane bulge outside the cell wall [Fig. 1(a), (c-e)]. Evidences showed that *E. coli* has large amount of extra outer membrane that will not apply significant constraints on the inner membrane bulge formation[130]. Figure 3.3 shows the image of a typical bulging cell. A plasmid pWR20 encoding EGFP was expressed to indicate the cytoplasmic volume. The uniform fluorescence in the bulge and the cell suggests that cytoplasm in the bulge and in the cell is connected. GFP molecules are able to move between the bulge and the cell interiors, indicating that cytoplasmic objects smaller than at least 3–4 nm are free to exchange between these compartments. Because the turgor pressure overwhelmingly results from the concentration of small solutes, the pressure in the cell and bulge can be considered the same.

Several lines of evidence indicate that the cell wall in bulged cells is not significantly different than in non–bulged cells. First, bulging is a discrete event that is completed within a few seconds. Second, the cell stiffness remains constant in the presence of vancomycin until the sudden bulging event when the stiffness drops dramatically [Fig. 3.4(f)]. Taken together, these indicate that the mechanical properties of the cell wall as a whole are unaffected by drug treatment except at the precise location of fracture and bulging.

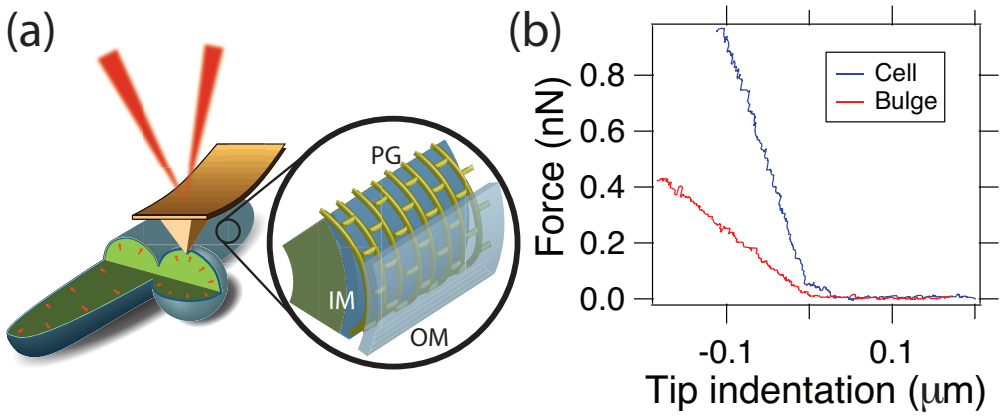

Figure 3.4: (a) Schematic cartoon illustrating the bulging *E. coli* and AFM stiffness measurement. The magnified region shows the details of the inner membrane (IM), peptidoglycan (PG) network in yellow mesh and the outer membrane (OM). (b) Typical force-indentation traces obtained by indenting a cell and bulge.

3.2.2 Surface appendages affect AFM probes

Wild type *E. coli* has a full set of surface appendages of pilus and flagellum. Since AFM probes the surface property, flexible surface appendages will severely compromise the stiffness quantification. Pili form a soft "cushion" that keeps the cantilever approaching the outer membrane, and the adhesive property of pili is particularly undesirable. Flagella can also disturb AFM tip to create extra noise. To remove the complication caused by the surface appendages, I constructed strain *YD133* ($\Delta flgE\ \Delta fimA\ \Delta fliC$) from the Keio collection. fimA encodes the P pilus assembly protein. $filC$ and $flgE$ encode the flagella filament and the hook. We did not remove the outer membrane subunit of pilus and the the basal body of the flagella motor because they do not seem to interfere with the stiffness measurement. *YD143* strain (*YD133 imp4213*) was made based on YD133 for the bulging experiments. The detailed protocols of the strain constructions are listed in Appendix A.

3.2.3 Experimental procedure

YD143 Cells are grown in LB medium containing 50 μg/ml kanamycin at 37°C to OD 0.3, followed by the addition of vancomycin (20 μg/ml) and a 10 minute incubation under 37°C. Cells are then immobilized on poly-l-lysine (PL) coated glass coverslips. In the presence of the drug, cells stochastically form bulges along the cell cylinder. We probe the stiffness of the cell and bulge with a custom-built AFM/fluorescence microscope [Fig. 1(a)].

Mechanical stiffness is measured by comparing the slope of indentation on the cell, bulge and glass surface as stated above. On each cell, a line is drawn across the cell so that cell body, cell wall and glass substrate are all covered. Then a number of points, typically 40, will be chosen on this line and the indentation is taken on each point. Figure 3.5 shows a typical trace of these measurements. The height profile clearly shows the boundaries of the bulge and cell body. To exclude the effect of viscosity on

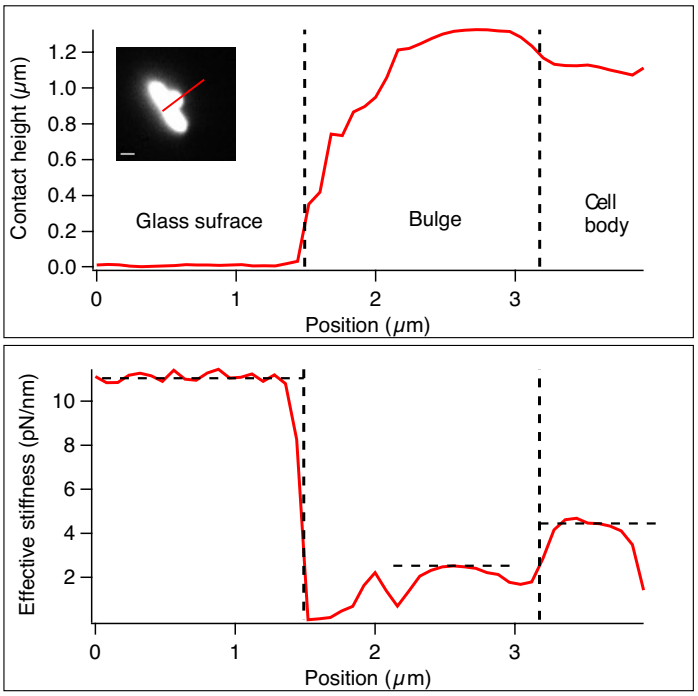

Figure 3.5: Stiffness and height along a line across the glass substrate, bulge and cell body of *E. coli* strain *imp4213 pWR20*. a) Height profile shows the geometry of the bulge and the cell. The height of the bulge indicates the approximate diameter of the bulge. b) The effective stiffness of the spring and substrate in series. The hard surface indentation stiffness is calibrated to be the cantilever stiffness 11 pN/nm. The insert is the cytoplasmic GFP image of this bulging cell, and a red line indicates the scan line, along which the indentation points distributesThe scale bar is 1 μm.

the stiffness, we tested the stiffness at several indentation speeds and found similar results. All measurements used a pyramidal-tipped cantilever (stiffness = 11 pN/nm, manufacture nominal value) and an indentation speed of 3 μm/s. The cell radius is obtained from the point of contact between the tip and the cell. The bulge radius is obtained from fluorescence microscopy.

3.2.4 Bulge stiffness under conical indenter

The shape of a deformed, pressurized membrane bulge indented by a conical indenter of half cone–angle α with force F can be solved analytically. Let P be the pressure in the bulge and σ_b the surface tension. Note that σ_b is uniform on the entire liq-

uid membrane bulge. From the force balance condition in the axial direction, the indentation force in cylindrical coordinates (r, ϕ, z) is given by

$$\pi P r^2 + 2\pi r \sigma_b \sin\theta = F, \tag{3.7}$$

where θ is the elevation angle of the bulge tangential direction in the axial cross-section [166]. The radial coordinate of the bulge contour r and it's derivative are

$$r = \frac{\sigma_b}{P}\left(\sqrt{\sin^2\theta + a} - \sin\theta\right), \tag{3.8}$$

and

$$\frac{dr}{d\theta} = -\frac{r\sigma_b \cos\theta}{Pr + \sigma_b \sin\theta}, \tag{3.9}$$

where $a = \dfrac{PF}{\pi\sigma_b^2}$. At $\theta = -\pi/2$, r reaches the bulge radius R_b and the surface tension σ_b can be solved from Equation (3.7):

$$\sigma_b = \frac{PR_b}{2} - \frac{F}{2\pi R_b} \tag{3.10}$$

Substituting Equations (3.8) and (3.9) into $\dfrac{dz}{dr} = \tan\theta$, we obtain

$$\begin{aligned} dz &= \tan\theta dr \\ &= \tan\theta \frac{dr}{d\theta} d\theta \\ &= \frac{\sigma_b}{P}\left(\frac{\sigma_b \sin^2\theta}{\sqrt{\sin^2\theta + a}} - \sin\theta\right) d\theta. \end{aligned} \tag{3.11}$$

Integrating over z, the shape of the bulge is solved as a function of the elevation angle θ. Here, we separate the total indentation into three parts: $h = h_{gobal} + h_{dent} + h_{cone}$ (Fig. 2). These are the distance from the highest point on the deformed bulge to

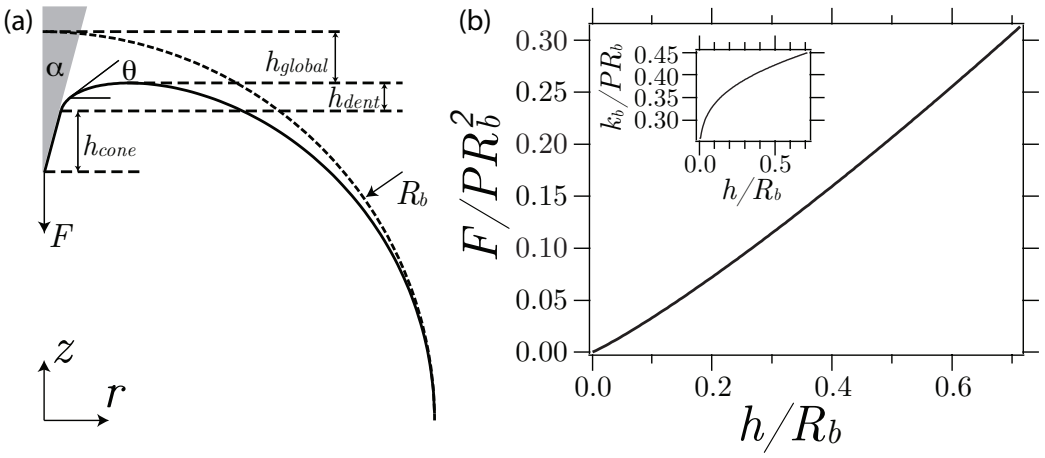

Figure 3.6: Model of a fluidic membrane bulge under a force F exerted by a conical indenter. (a) The total deformation of the bulge consists of a global deformation, h_{global}, a local dent h_{dent} and the contact height h_{cone}. The dashed line is a sphere of radius equal to the bulge waist. (b) The dimensionless force–indentation relation is nearly linear. Inset: dimensionless stiffness vs. indentation.

the undeformed bulge pole, h_{global}; the height from the indenter contact point to the highest point on the bulge, h_{dent}; and the depth of the contact region between the cone and bulge, h_{cone}. We further define the elliptical integral

$$I(\xi, a) = \int_0^{\xi} \frac{\sin^2 \zeta}{\sqrt{\sin^2 \zeta + a}} d\zeta, \tag{3.12}$$

The first two parts of the indentation can be easily solved

$$\begin{aligned} h_{global} &= R_b - [z(0) - z(\pi/2)] \\ &= R_b - \frac{\sigma_b}{P}\left[1 + I\left(\frac{\pi}{2}, a\right)\right]; \\ h_{dent} &= z(0) - z(\pi/2 - \alpha) \\ &= \frac{\sigma_b}{P}\left[1 - \sin\alpha - I(\pi/2 - \alpha, a)\right]. \end{aligned} \tag{3.13}$$

h_{cone} is determined by the radius of the contact circle where the normal force between the membrane bulge and the indenter vanishes. From Equation (3.8), setting $\theta =$

$\pi/2 - \alpha$, the radius of the contact circle is

$$r_{cone} = \frac{\sigma_b}{P}\left(\sqrt{\cos^2\alpha + a} - \cos\alpha\right), \tag{3.14}$$

so that

$$h_{cone} = \frac{\sigma_b}{P}\left(\sqrt{\cos^2\alpha + a} - \cos\alpha\right)\cot\alpha. \tag{3.15}$$

The total indentation size for an indentation force F, a bulge of radius R_b, an indenter half–conical angle of α and pressure P is given by

$$h = h_{gobal} + h_{dent} + h_{cone}; \tag{3.16}$$

The indentation, h, has a nearly linear dependence on the indentation force [Fig. 3.6(b)]. Under experimental conditions where $\alpha = \pi/12$, $R_b \sim 0.5\mu$m, $P \sim 1$ kPa and $F \sim 0.01 - 0.1$ nN, the dimensionless spring constant k_b/PR_b varies from 0.35 to 0.38 [Fig. 3.6 (b) *inset*].

For each bulging cell, we measure h/R_b and use the model to obtain the reduced stiffness k_b/PR_b as shown in the inset of Fig. 3.6(b). From the mechanical measurements of the bulge stiffness and radius, we then calculate the turgor pressure P in that particular cell. We then use this value to estimate the circumferential surface tension experienced by the cell wall, $\sigma_\perp = PR_c$, where R_c is the cell radius [1].

Figure 3.7 shows the cell radius, R_c, and stiffness, k_c, as functions of the pressure derived from bulge indentation. Both radius and stiffness are positively correlated with the turgor pressure. We further determined the size and stiffness of non–bulging cells to be 0.55 ± 0.02 μm and 0.017 ± 0.002 N/m, respectively [2].

[1] Circumferential quantities are denoted as $\perp$ while axial quantities are denoted as $\parallel$.

[2] The size and stiffness of a similar strain of *E. coli* that does not carry the *imp4213* mutation was within 10% of the values for the *imp-* strain, indicating that increased outer membrane permeability does not have a large effect on the turgor pressure or cell wall elasticity.

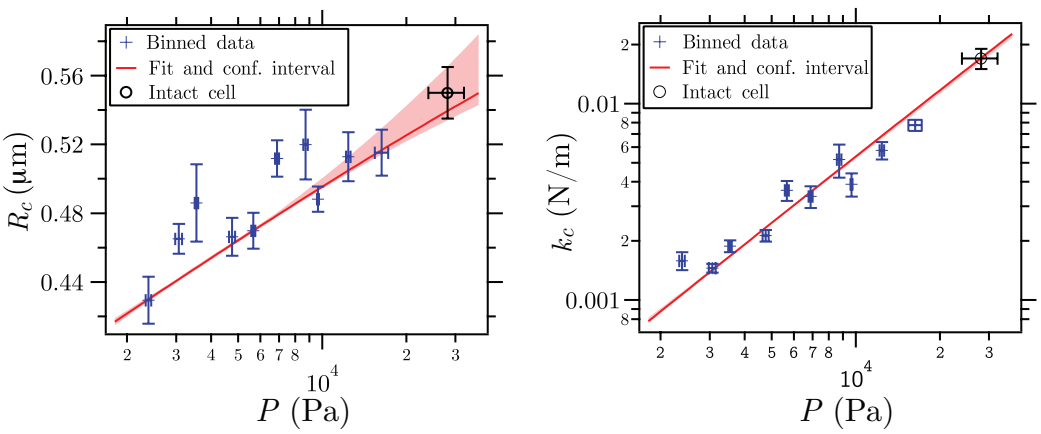

Figure 3.7: Bulging cell radius R_c and indentation stiffness k_c are plotted against cell turgor pressure P obtained from the individual bulge indentation stiffness measurements. Data from 72 bulged cells are binned in 10 logarithmically–spaced bins using weights from the relative error estimates of the individual indentation traces and fluorescent images (blue crosses). Data from 42 non-bulged cells are plotted as black open circles. Red lines indicate the best fit of the stress–stiffening model along with 68% confidence intervals.

3.2.5 Finite element simulations of cell indentation

The indentation stiffness of the cell wall is governed by terms associated with stretching and bending of the PG as well as terms related to the surface tension. While the bending energy of the wall has been shown to be negligibly small [5], we cannot ignore the stretching energy of the PG network and thus analysis of the cell indentation data is more complicated than for bulge indentation. The deformation of a elastic tube under external force and internal pressure is a classical 3D static linear elasticity problem. In biological applications, Zhao *et al.* probed rod-shaped fungus Aspergillus nidulans with AFM and made an attempt to construct a complete picture with cell wall mechanics and turgor pressure together analyzed with finite element methods[169]. In my study, we also used finite–element calculations of the force–indentation relation for an inflated cylindrical shell [Fig. 3.8 *inset*].

In our simulation, the cell wall is modeled as a tube with 2 μm length, and terminated with spherical endcaps (Fig. 4 *inset*). The simulation was performed on a quadrant of the endcapped cylinder with symmetric boundary condition. We adopt

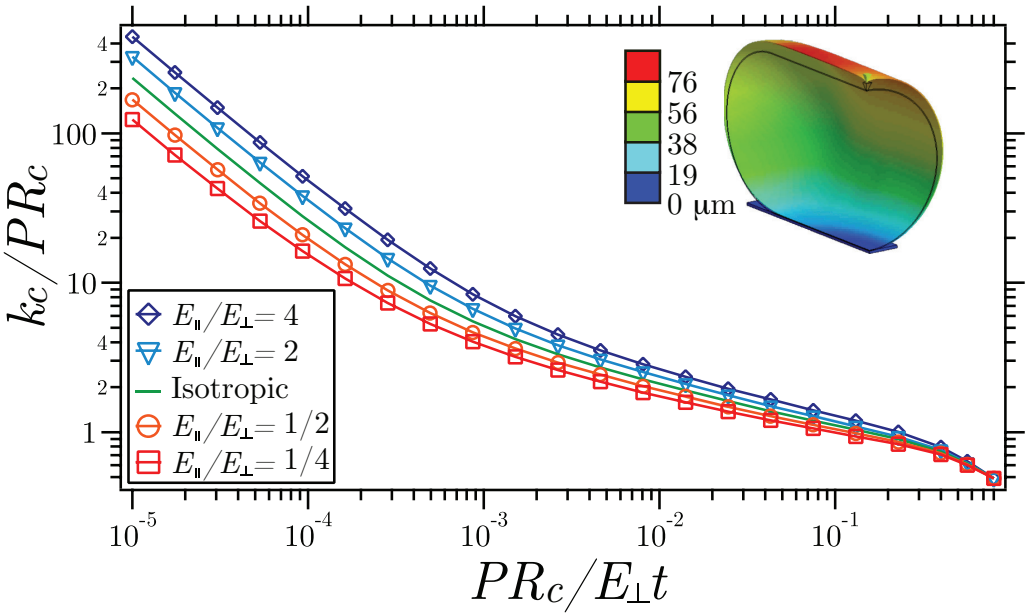

Figure 3.8: Simulated value of reduced cell indentation stiffness k_c/PR_c against the reduced inflation magnitude $PR_c/E_\perp t$ for different orthotropic ratios of the stretching elasticity in the axial direction to the circumferential directions, $E_\parallel/E_\perp$. (inset) The result of a single simulation. One quadrant of the indented cylinder is shown, with color labeling the displacement in the indentation direction. The black wireframe shows the undeformed, unpressurized capsule.

the convention of natural, or engineering, stress and strain to define the Young's modulus E and set the poisson ratio to zero. The elastic modulus is set to 20 MPa, the thickness to 6 nm (yielding a combined parameter $Et = .12$ N/m), the cell radius in the absense of pressure to 500 nm and the cone angle of the indenter to $\pi/12$ with a spherical tip of radius 7.5 nm. The turgor pressure is chosen to be the independent variable, and the indentation stiffness is obtained from the force required to create an indentation of 1/20 of the cell radius. Rather than attempting to estimate the elastic parameters for each measured cell, we generated a numerical model for the radius, R_c, and stiffness, k_c, in the presence of stress–stiffening and performed a global fit to all the cellular indentation data.

We incorporate stress–stiffening in the cell wall by describing the nonlinear elasticity of the PG network as a power law in the turgor pressure, $E_\perp = E_0(P/P_0)^\gamma$. E_0 is the Young's Modulus at reference pressure P_0 (fixed at 5 kPa, in the middle of the

range of measured bulge pressures), and γ is the stress–stiffening exponent. Here, the nonlinearity is only dependent on the pressure in a given cell and we ignore the much smaller change in stress caused by AFM indentation. The independent parameters γ and $E_0 t$, where t is the thickness of the cell wall, fully define the nonlinear elasticity. These two quantities, combined with the radius of a cell at the reference pressure, R_0, make up the fitting parameters for interpreting bulged cells. Our global fit additionally includes the radius and stiffness data from the non–bulged, intact cells which introduces one additional free parameter: the physiological turgor pressure.

3.2.6 Radial expansion of an inflated cylinder with stress-stiffening

Here, we model the radius R_c of an elastic cylinder under variable internal pressure P. Radial expansion of a cylinder under pressure is governed by the elasticity of the cylinder wall in the circumferential direction, $E_\perp$. In the follow discussion, we set the Poisson's ratio to zero. The circumferential surface tension on the wall

$$\sigma_\perp = P R_c, \tag{3.17}$$

and the natural stress is $\sigma_\perp / t$, where t is the thickness of the wall. $E_\perp$ is defined using the natural stress and the incremental strain, dR_c/R_c:

$$E_\perp \frac{dR_c}{R_c} = \frac{d\sigma_\perp}{t}. \tag{3.18}$$

We also assume that $E_\perp$ depends on the internal pressure P and follows a power law

$$E_\perp = E_0 \left(\frac{P}{P_0} \right)^\gamma, \tag{3.19}$$

where E_0 and P_0 can be combined to one single free parameter, E_0/P_0^γ. Without loss of generality, we choose E_0 as the free parameter and fix $P_0 = 5$ kPa, a typical turgor pressure in a bulging cell. Let R_0 be the radius of the cylinder at pressure P_0. We define the following dimensionless quantities

$$\begin{aligned} \hat{P} &= P/P_0; \\ \hat{E} &= E_\perp/E_0; \\ \hat{R} &= R_c/R_0; \\ \hat{\sigma} &= \frac{\sigma_\perp}{P_0 R_0}; \\ p &= \frac{P_0 R_0}{E_0 t}. \end{aligned} \tag{3.20}$$

Equations (3.17), (3.18) and (3.19) can then be rewritten as

$$\hat{\sigma} = \hat{P}\hat{R}, \tag{3.21}$$

$$\hat{E}\frac{d\hat{R}}{\hat{R}} = p d\hat{\sigma}, \tag{3.22}$$

$$\hat{E} = \hat{P}^\gamma, \tag{3.23}$$

Equations (3.21-3.23) can be combined and solved to yield

$$\frac{d\hat{R}}{\hat{R}^{\gamma+1}} = p\frac{d\hat{\sigma}}{\hat{\sigma}^\gamma}, \tag{3.24}$$

and

$$\hat{\sigma} = \left[1 + \frac{1-\gamma}{p\gamma}\left(1 - \hat{R}^{-\gamma}\right)\right]^{\frac{1}{1-\gamma}} \tag{3.25}$$

In the limit of linear stress stiffening, i.e. $\gamma \to 1$, the dimensionless tension reduces to

$$\hat{\sigma} = \exp\left[\frac{1}{p}\left(1 - \frac{1}{\hat{R}}\right)\right] \tag{3.26}$$

Using Equation (3.21), we obtain the desired relationship between the pressure and the inflated radius

$$\frac{P}{P_0} = \frac{R_0}{R_c}\left[\frac{(\gamma-1)E_0 t}{\gamma P_0 R_0}\left[(\frac{R_0}{R_c})^{\gamma} - 1\right] + 1\right]^{\frac{1}{1-\gamma}} \tag{3.27}$$

Again, this is simplified in the limit $\gamma \to 1$:

$$\frac{P}{P_0} = \frac{R_0}{R_c}\exp\left[\frac{E_0 t}{P_0 R_0}(1 - \frac{R_0}{R_c})\right] \tag{3.28}$$

The radial expansion, $R_c(P; E_0 t, \gamma, R_0)$, can be solved implicitly from the following equation as derived in the supplemental materials [1]

$$\frac{P}{P_0} = \frac{R_0}{R_c}\left[\frac{(\gamma-1)E_0 t}{\gamma P_0 R_0}\left[(\frac{R_0}{R_c})^{\gamma} - 1\right] + 1\right]^{\frac{1}{1-\gamma}}. \tag{3.29}$$

The dimensionless quantity $PR_c/E_{\perp}t$ describes the magnitude of inflation under pressure.

3.2.7 Anisotropy of the elastic modulus in the presence of stress-stiffening

For a cylinder, the surface tension is anisotropic. The tension in the circumferential direction is twice that along the axial direction. For a stress-stiffening material, this results in an anisotropic elasticity. Here, we find the ratio of the axial elasticity to the circumferential elasticity at a given pressure.

Equations (3.21) and (3.25) can be combined to give the dimensionless pressure at a given surface tension

$$\hat{P}(\hat{\sigma}) = \hat{\sigma}\left[1 - \frac{p\gamma}{1-\gamma}\left(\hat{\sigma}^{1-\gamma} - 1\right)\right]^{\frac{1}{\gamma}} \tag{3.30}$$

which reduces to

$$\hat{P}(\hat{\sigma}) = \hat{\sigma}\left(1 - p\ln\hat{\sigma}\right) \tag{3.31}$$

in the limit that $\gamma \to 1$. The elastic modulus is found by taking this expressions to the power γ:

$$\hat{E}(\hat{\sigma}) = \hat{\sigma}^{\gamma}\left[1 - \frac{p\gamma}{1-\gamma}\left(\hat{\sigma}^{1-\gamma} - 1\right)\right] \tag{3.32}$$

Note that Equation (3.32) is a general expression that applies in both the circumferential and axial directions, where the surface tension differs by a factor of two. Therefore, the anisotropic ratio of the two elasticities can be found as

$$\frac{E_{\parallel}(\hat{P})}{E_{\perp}(\hat{P})} = \frac{\hat{E}\left[\hat{\sigma}_c(\hat{P})/2\right]}{\hat{E}\left[\hat{\sigma}_c(\hat{P})\right]}. \tag{3.33}$$

3.2.8 Scaling laws

When an inflated cylinder is indented by a conical indenter, the force F required to generate an indentation h can be written as

$$F = \mathcal{F}(h; E, P, R, t, \delta), \tag{3.34}$$

where E and P are mechanical parameters corresponding to stiffness and pressure and R, t, and δ, are geometric parameters corresponding to the cylinder radius, cylinder thickness and indenter tip radius. The inflated cylinder radius can be written as

$$R = \mathcal{R}(E, P, R_0, t), \tag{3.35}$$

where R_0 is the radius at any given reference pressure P_0. The functions $\mathcal{F}$ and $\mathcal{R}$ are determined by the material properties of the material under consideration. Due to the linearity of solid mechanics, scaling the mechanical parameters results in a scaling of the function $\mathcal{F}$ but leaves $\mathcal{R}$ unchanged:

$$\mathcal{F}(h; \lambda E, \lambda P, R, t, \delta) = \lambda \mathcal{F}(h; E, P, R, t, \delta); \tag{3.36}$$

$$\mathcal{R}(\lambda E, \lambda P, R_0, t) = \mathcal{R}(E, P, R_0, t). \tag{3.37}$$

Similarly, when all spatial dimensions scale we have

$$\mathcal{F}(\mu h; E, P, \mu R, \mu t, \mu \delta) = \mu^2 \mathcal{F}(h; E, P, R, t, \delta); \tag{3.38}$$

$$\mathcal{R}(E, P, \mu R_0, \mu t) = \mu \mathcal{R}(E, P, R_0, t). \tag{3.39}$$

For thin shells, one additional scaling rule applies according to Kirchhoff–Love theory [88]:

$$\mathcal{F}(h; \eta E, P, R, \eta^{-1} t, \delta) = \mathcal{F}(h; E, P, R, t, \delta); \tag{3.40}$$

$$\mathcal{R}(\eta E, P, R_0, \eta^{-1} t) = \mathcal{R}(E, P, R_0, t). \tag{3.41}$$

The three scaling laws together reduce the total number of independent parameters in the cylinder–indentation problem:

$$\mathcal{F}(h; E, P, R, t, \delta) = PR^2 \cdot \mathcal{F}(h/R; Et/PR, 1, 1, 1, \delta/R); \tag{3.42}$$

$$1 = \mathcal{R}(Et/PR, 1, R_0/R, 1). \tag{3.43}$$

From Equation (3.42), we obtain the scaling rule for the stiffness:

$$\frac{d\mathcal{F}(h; E, P, R, t, \delta)}{dh} = PR \cdot \mathcal{F}'(h/R; Et/PR, 1, 1, 1, \delta/R). \tag{3.44}$$

For small indentations, where the stiffness of the material can be considered to be nearly linear, $\mathcal{F}'$ is independent of the indentation depth h. Therefore, k/PR only depends on PR/Et and the scaled indenter size δ/R. In addition, from Equation (3.43), the dependence of R/R_0 on PR/Et can be implicitly solved.

Calculation of the cell stiffness under pressure, $k_c(P; E_0t, \gamma, R_0)$, is significantly more complicated. The dimensionless stiffness, k_c/PR_c, depends only on $PR_c/E_\perp t$ as can be found from scaling arguments, and monotonically decreases as the cylinder is inflated due to the relative magnitudes of surface tension and shell bending [Fig. 3.8 *green line*]. However, stress stiffening adds an extra complication due to an anisotropy inherent in a cylindrical geometry; the surface tension in the circumferential and axial directions of a cylinder are different by a factor of 2. Therefore, the Young's modulus, which is a function of surface tension, is orthotropic. We simulated indentation of pressurized cylinders with several different values for the elastic anisotropy, $E_\parallel/E_\perp$ [Fig. 3.8]. For a given pressure, the anisotropy can be calculated [1] and the correct relationship between the dimensionless stiffness and the radial inflation can be interpolated using the curves shown in Fig. 3.8. Combined with the radial expansion function, this is sufficient to solve for $k_c(P; E_0t, \gamma, R_0)$.

The results of a global fit of the functions $R_c(P; E_0t, \gamma, R_0)$ and $k_c(P; E_0t, \gamma, R_0)$ to the experimental data are shown in Fig. 3.7. The best fit yields parameter estimates of $E_0t = 0.026 \pm 0.001$ N/m, $\gamma = 1.22 \pm 0.12$, $R_0 = 464.2 \pm 0.9$ nm and a turgor pressure $P = 29 \pm 3$ kPa. At this turgor pressure, using the estimated cell wall thickness 4.5 ± 1.5 nm [166], the cell wall Young's moduli are $E_\perp = 49 \pm 20$ MPa and $E_\parallel = 23 \pm 8$ MPa.

Table 3.1: List of constants and symbols

symbol	description	value
α	indenter half–cone angle	$\pi/12$
a	normalized indentation force	$PF/\pi\sigma_b^2$
P_0	normalization constant for pressure	5000 Pa
t	cell wall thickness	4.5 ± 1.5 nm
E_0	circumferential Young's modulus of the cell wall at pressure P_0	
$E_\perp$	circumferential Young's modulus of the cell wall	
$E_\parallel$	axial Young's modulus of the cell wall	
F	indentation force	
γ	stress–stiffening exponent	
h	total deformation	
k_b	bulge indentation stiffness	
k_c	cell indentation stiffness	
P	turgor pressure	
R_b	bulge radius	
R_c	cell radius	
σ_b	surface tension of the bulge	
$\sigma_\perp$	cell wall circumferential surface tension	
$\sigma_\parallel$	cell wall axial surface tension	
θ	elevation angle along bulge	
(r, z)	cylindrical coordinates in bulge calculation	
R_0	cell radius at pressure P_0	
IM	inner membrane	
OM	outer membrane	
PG	peptidoglycan	

3.2.9 List of symbols

3.3 Discussions

Previous work using AFM indentation of bacteria has been used to quantify turgor pressure and cell wall elasticity [5, 166]. In that work, the relationship between linear indentation and surface tension was established, but the stretching of the cell wall was neglected or at most underestimated. Our study, which independently measures the turgor pressure and cell stiffness, suggests that cell wall stretching and surface tension contribute similar amounts to the indentation stiffness. This is most evident in

the difference in the k/PR ratio for membrane bulges, ~ 0.36, and cells, ~ 0.9. This difference arises from the fluidity of lipid membranes; while the bulge can redistribute material to minimize stress, the rigid cell wall can not. For the cell wall, therefore, the overall stiffness depends on stretching even in a tension-dominated regime.

Mendelson and others introduced a pressure–independent, tube–bending method to quantify cell wall elasticity [95]. Wang *et al.* bent live *E. coli* cells and found their flexural rigidity to be $2.0 \pm 0.4 \times 10^{-20}$ Nm^2 [155]. This result yields an axial cell wall Young's modulus, including uncertainties in the wall thickness, of $E_{\|} = 11 \pm 4$ MPa, in agreement with our measurements. Using our numerical model, we combined this value of the axial modulus with the stiffness of intact cells measured using AFM indentation and estimate the turgor pressure in intact cells to be 35 ± 7 kPa. This bulge–free measurement further validates our estimate of the turgor pressure and cell wall stress–stiffening.

Polymer networks often exhibit a nonlinear stress-strain relation due to intrinsic geometric nonlinearities and a potential nonlinear force-extension relation of the individual polymers at finite temperature [50]. Boulbitch *et. al.* modeled the PG network as a hexagonal mesh of rigid glycan subunits and elastic peptide cross-links. They predicted a power–law relationship between the axial elastic modulus and stress with a stiffening exponent of ~ 1 [19]. We find a stiffening exponent of 1.22 ± 0.12 in the *E. coli* cell wall in quantitative agreement with the model and similar to observations from gram–positive *Bacillus* sacculus threads [143].

The main function of cell wall is to bare tension created from the turgor pressure, especially under hypoosmotic shocks that can dramatically increase the turgor pressure. Even though it is the cytoplasmic membrane that generates the turgor pressure, the expansion of the membrane is counter-balanced by the normal restricting force from the cell wall. On the other hand, the channels and transporters that regulate the solute importation and exportation sense membrane tension that is generated from

the turgor pressure as discussed in Chapter 1. It appears contradictory that cell membrane transfers the tension to the cell wall but meanwhile still able to measure surface tension. This "paradox" can be solved by the difference in elasticity of cell wall and cell membrane. Elasticity of lipid membrane has been recently measured by Picas *et al* using AFM[113]. Their results suggest that cell membrane also has a nonlinear elasticity similar to cell wall, However at certain strain, the elastic modulus reaches 40 MPa, a value surprisingly in accordance with our measurement with peptidoglycan at slightly turgid pressure, and seized to grow at higher strain. At lower turgor pressure, both cell wall and cell membrane are soft and flexible. Enabled by the flexible cell envelope, a change in turgor pressure will cause significant change in cell shape, thus membrane tension, and allow mechanosensitive channels to respond to the change. Whereas at high turgor pressure, the cell wall elastic modulus increases faster than that of the cell membrane, bearing more tension and restraining volume inflation. The nonlinear elasticity of lipid membrane, together with stress-stiffening of cell wall works as a passive adaptation mechanism to balance surface tension measurement and cell wall protection.

The fact that the cell wall and the cell membrane together takes surface tension implies that the surface area of the two are always the same unless plasmolysis takes place. Experimental results on *E. coli* also show the surface area of spheroplast is identical to intact cells within error (unpublished data by Miller and Shaevitz). Even during cell growth, the cell surface area constantly increases, which brings up the question how the wall and the membrane manage to grow at the same rate, or how these two completely different biochemical process couple together. Hinted by the mechanism of mechanosensitive channels, I hypothesize that the membrane tension possibly participates not only in regulating turgor pressure, but also in synchronizing cell wall and membrane growth (figure 3.9). Upon cell wall growth, the surface area of cell wall increases, causing the membrane to expand and increase tension. The minor

tension can boost the fusion of lipid into the membrane as shown experimentally by Staykova *et al*[133], or trigger membrane production. So far there is no evidence to connect bacterial membrane tension and lipid production, but it is well known in eukaryotic cells, cortical tension directly regulate endocytosis, exocytosis, which is a mechanism to modify surface area[31]. More generally, cell mechanics may play a key role in the information flow between global cellular property such as size, shape, macromolecule organization such as DNA, and formation of sub-cellular structure, and microscopic molecular scale biochemistry.

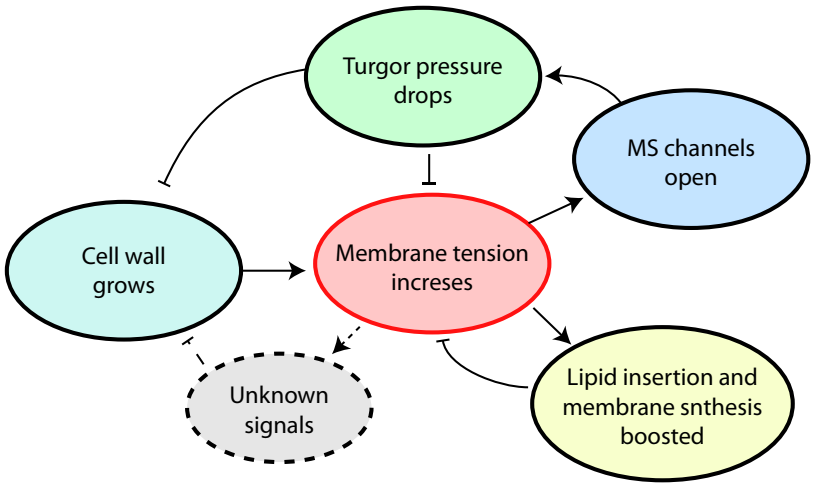

Figure 3.9: Schematic figure to show the proposed roles of mechanical parameters to regulate cell physiological functions such as material transportation, membrane synthesis and growth. As the cell wall area increases, the tension on the key mechanical parameter, the surface tension increases, which can trigger the mechanical sensitive (MS) channels to regulate the turgor pressure, and accelerate the insertion rate or synthesis of the cell membrane.

To summarize, we used AFM and fluorescent microscopy to probe the elastic properties of live *E. coli* cells using a system that allows us to separately probe pressure and elasticity. Our results indicate that the turgor pressure in live cells is $\sim$ 30 kPa, or $\sim$ 0.3 atm. This value is lower than previous chemical estimates of the pressure but similar to other mechanical measurements. Our data further indicate that the cell wall stress-stiffens. Stress–stiffening affords a unique mechanical advantage to cells by preventing abrupt cell shape changes during changes in external

pressure or osmolarity while maintaining a relatively compliant cell elasticity under normal conditions.

Chapter 4

Rod-shaped Bacterial Cell Wall Growth Dynamics Revealed by Nano-motion Capturing

4.1 Background of Bacterial Cell Wall Growth

As the major tension bearing element, the building blocks of bacterial cell wall, peptidoglycan units form a high cross-linking density covalently linked polymer network. As discussed in the previous chapter, cell wall has a novel static mechanical property, and may participate in the regulation of bacterial physiology in addition to providing protection against turgor pressure. However in order for a cell to grow, the cell wall has to be remodeled by inserting new material into the existing wall, and also removing material by autolysis (also called cell wall turnover). Peptidoglycan insertion is the final stage of the whole PG synthesis process and takes places in the periplasmic space at the interface between cytoplasmic membrane and cell wall. PG precursor Lipid II is harvested by the penicillin binding protein (PBP) complexes, which ac-

complish to incorporate PG subunit by transpeptidation and transglycosylation. The details of this process how lipid II enters each PBP complex remain elusive.

Peptidoglycan subunit has an asymmetric cross-linking nature, which is disaccharide connecting to form relatively longer stands over 100 nm, while the peptide side chains to form short cross-linkers of typically a few animo acids, 10 in the case of *E. coli* between glycan strands. NMR studies showed that instead of a random orientation, the glycan strands align roughly in parallel, whereas the cross-linking peptides are nearly perpendicular to the glycan strands[151]. In single-layered rod-shaped gram-negative bacterial cell wall, the plausible organization of PG is such that glycan strands run in parallel with the cell surface approximately along the circumferential direction. For gram-positive bacteria, because the cell wall is generally thicker (20-80 nm), more possibility exists as to how PG is organized. It is favored that the gram-positive wall is simply a stack of the single-layered gram-negative cell wall, although the extremely experimental results can not rule out other possibilities such as the scaffold architecture (figure 1.3).

The knowledge of PG biochemistry helps understand what participates in synthesizing cell wall and what their relationships are, it does not provide a mechanism for the formation of a particularly well defined shape. In addition, geometrical and dynamical information are required to answer the question how PG subunits self-organize into an ordered structure with a spatial scale mediated at micrometer scale by molecular machinery at nanometer scale. To give rise to an asymmetric, highly ordered bacterial cell wall, the enzymatic machinery that facilitates material insertion must be organized following certain rules. It is indeed observed that bacterial cells have non-diffusive sub-cellular structures that are closely related to the cell morphology. The structure of actin homolog in bacteria MreB was first resolved by van den Ent *et al*[149], and identified to have a role in governing cell shape: depletion of MreB leads to lemon-shaped defect and cell lysis after a few generations. GFP and YFP

fluorescent fusion of MreB appeared helical in many species of bacteria, or filamentous in fission yeast and *in vitro*. Recent studies challenged this MreB configuration[138], and proposed that MreB formed translocating foci along the circumferential direction, in parallel to the glycan strands in gram-negative bacteria, or in the layered model of gram-positive bacteria[42, 51, 150]. More directly, PBP II itself was found undergoing similar motion in gram-positive bacterium *B. subtilis*. The translocation of these protein complexes requires the activity of PBP, as when treated with PBP inhibitory antibiotics, both MreB and PBP motion seized[51, 150], strongly suggesting that the motion itself is driven by, and facilitating PG insertion.

4.1.1 Growth models

In the past few years, several quantitative growth models for rod-shaped bacteria have been proposed based on mean field or the observations of PBPs and MreB family proteins localization and motion, with the goal to resemble a robust cylindrical growth mechanism to maintain cell radius. On the global scale without considering the detailed microscopic growth, Jiang *et al* built a mean field model to recapitulate the balance between the free energy gain from forming new bonds in the PG during growth, and the energy cost to stretch the newly inserted PG patches[73]. They defined a general forces of growth as the net free energy gain per unit change in the cell radius and length, and set the growth rates on the two directions proportional to the general forces. With experimentally determined parameters such as cell turgor pressure, wall stretching stiffness, their energy argument successfully predicted a optimal radius for rod-shaped bacteria to minimize the free energy during growth.

At the microscopic scale, Furchtgott *et al* numerically simulated the dynamics of the cell wall under different insertion rules of the new material in terms of the selection of the insertion locations[48]. The PG network was modeled as a mesh network with cross-linked glycan strands as the building blocks. New glycan strands with a variable

length were inserted between two existing strands at a location selected based on certain insertion rule. If following a self-similar random insertion meaning that the any peptide cross-linker had equal chance to be selected as the insertion site, the mesh network would develop bulges, bends, large holes, and the radius was not kept. In contrast, a uniform insertion did not cause positive feedback on the perturbations of the local PG density. Interestingly, a global insertion order had similar effect as the uniform insertion. These order are in the form of inserting at a finite processivity along a circumferential hoop, of intact or segmented helical tracks[150].

Another microscopic model quantitatively addressed the motion of the growing end of the glycan strands responsible for active cell wall growth[2]. It was assumed that the experimentally observed moving PBP and MreB was exactly where glycan strand tips grew, and these tips were the dislocations, or topological charges in a crystalline peptidoglycan similar as defects in regular crystals (figure 1.4(a)). The motion of the dislocations were driven by the Peach-Koehler force exerted by both the turgor pressure [111] and chemical energy released by forming bonds. Apart from the active dislocations that were moving, many more dislocations were not associated with PBPs or not actively moving, stayed stationary, and did not contribution to the cell elongation. The active and inactive dislocations convert back and forth, and interact with each other through surface tension of the cell wall. Even tough it is difficult to associate experimentally observable properties of the cell with the parameters in the dislocation model, it nonetheless provides a plausible microscopic view to quantitatively bridge the microscopic molecular mechanism to the global growth at cellular scale.

4.1.2 Observations of rod-shaped cell wall growth

Long before the quantitative models for cell wall growth were proposed, experimentalists had been trying various ways to depict the insertion rules. The visualiza-

tion of the peptidoglycan incorporation is first realized by labeling the PG precursors. Isotope pulse-labeling[108] and D-Cys-labeling[35] showed a diffusive or patchy growth pattern in E. coli, while fluorescent labeling using ramoplanin-fluorescein and vancomycin-fluorescein in *B. subtilis* showed patchy or segmented helical pattern[145]. These insertion patterns support the picture that the moving PBP complexes facilitate new PG insertion, although direct correlation between growth and PBP localization is not available due to the limitations in spatial and temporal resolution of these techniques. More macroscopically at the cellular level, Want *et al* attached two fluorescent beads as fiducial markers on the surface of *E. coli* and *B. subtilis* to observe the growth of the whole cell[156]. It was found that both *E. coli* and *B. subtilis* rotate as the cells are elongating, suggesting a global chiral order of the PG organization, possibly due to the helical insertion guided by the cytoskeletal proteins.

4.2 Labeling cell wall with high density quantum dots

In order to obtain a high-resolution, high accuracy growth map, several considerations must be taken into account. Firstly, the cells need to stay viable during the decoration, and are able to grow afterwards. Secondly, the markers must be small enough that they don't affect, or are not affect by the growth. Because we seek high density decoration, the bead assay developed by Wang et al is not suitable because of the size of the beads are typically hundreds of nanometers, and thus will interact with the surface when the cell is immobilized. Thirdly, accurate determination of growth requires high contrast in the surface labeling. For instance, organic fluorescent dyes are small molecules that can be used to label cell wall as shown in [145, 59]. However, the labeling density is usually so high that the features in the fluorescence signal is at the scale of micrometers. Tracking these features during growth can only give

information at very limited resolution. Reducing labeling density can increase labeling heterogeneity, at the cost of weaker signals and severe photobleaching. Fourthly, the decoration must faithfully indicate the cell wall movement. Labeling the membrane, membrane associated protein, or flexible appendages of the cell are not proper for our purpose.

With all the requirements listed above, I choose quantum dots (QD) as the marker to decorate the surface of the cell. Quantum dots are semiconductor nano-crystals of size typically 3-5 nanometers in diameter for the core. The surface of a quantum dot is usually covered with organic coating and can be chemically functionalized at will. Quantum dots have substantially better resistant to photobleaching than fluorescent protein and organic dyes, making it possible to withstand long-lasting imaging during cell growth. The high brightness also allows resolving individual dispersively distributed quantum dots from fluorescence images, thus improves the resolution of grow map from micrometer to diffraction limit of the images.

Gram-positive and gram-negative bacterial have different envelope structure. Gram-negative bacteria have an outer membrane that selectively transports material to the periplamic space, thus providing protection against toxic molecules. Due to the outer membrane, it is hard to get direct access to the cell wall and fluorescently label it. Surface structure of gram-negative bacteria, such as the s-layer or lipopolysaccharide (LPS) can be stained[129, 52], but it provides little information regarding the cell wall growth due to the fluidity of the outer membrane. On the contrary, gram-positive bacteria lack the outer membrane, therefore the peptidoglycan is directly exposed to the external environment available for modification. Although a high portion of the surface area is still covered by the s-layer[139], the direct and firm linkage between s-layer and the PG layer makes the surface of gram-positive bacteria a transiently solid substrate for labeling, while the fluidity is solely contributed from the PG insertion at slow temporal scales. For these reasons, I choose the model

organism for gram-positive bacteria, *B. subtilis* as the model organism to study cell wall growth dynamics.

The fluorescent markers can be attached to the *B. subtilis* cell wall by an intermediate molecule that binds to the subunits of PG, or they can be covalently linked to PG directly. Both methods are shown to be effective. In the first approach, wheat germ agglutinin (WGA) is chosen to be the intermediate molecule because it binds preferentially to N-acetyl glucosamine (GlcNAc), one of the primary subunits of PG[128, 45]. Specifically, carboxylated quantum dots are first functionalized with 1-Ethyl-3-[3-dimethylaminopropyl] carbodiimide (EDC), a standard cross-linker to couple carboxyl groups to primary amine, then the functionalized QD are incubated with WGA to react with the primary amine on the surface of WGA. Finally, the labeled WGA are then incubated with bacillus cells to bind to the PG. WGA-QD conjugate achieves a nearly uniform labeling at a density of greater than 10 QD per micrometer cell length, or 3 per square micrometer, high enough that the limiting factor to the growth map resolution is the optical diffraction at typically 100-150 nm.

Because the peptide cross-linking fraction in peptidoglycan is only 30-50 %[152], a high density of amine groups at the termini of the peptides are available for chemical modifications, thus EDC activated QD can directly link to the surface amine groups on PG. Cautions must be taken for the following reasons. Because EDC cross-links all amine and carboxyl groups, it is extremely toxic to live cells. Unbound excess EDC must be removed before reacting with the PG amine, and it was achieved by dialysis. Also because the functionalized QD reacts with all primary amine groups, the incubation media must not contain amine group. I used a phosphate buffer with Mg^{2+} and SO_4^{2-} and glucose as the incubation media to reduce the stress to the cells.The density of quantum labeling reaches 10 μm^{-1} in length, or an area density of 3 μm^{-2}. Even tough lower than WGA mediated labeling, directly labeling provides

shorter and stronger linkage. The detailed protocols of WGA labeling and direct labeling are listed in the Appendix B.

To show the surface decoration by quantum dots, we took transmission electron microscopy (TEM) images of the labeled *B. subtilis* (figure 4.1). The negatively stained cells appear overall dark, thus only the quantum dots resides on the side are visible under TEM. These quantum dots appear as cylinders of 5 to 10 nanometers, sometimes in clusters. A light gray halo is usually visible, presumably due to the polymer cross-linker surrounding the quantum dots. On the surface of the cell wall, quantum dots typically are closely attached, sometimes embedded into the PG at high density ($\geq 10\mu\text{m}^{-1}$). The height of the bump caused by the dots is typically smaller than 5 nm. In order to immobilize cells on the surface for fluorescence imaging, I press the labeled cells between glass coverslip and buffered LB (without Sodium Cloride) 0.3% agarose gel. The soft gel allows cells to grow freely, and in contrast, cells pressed between stiffer 1% agarose gel will buckle during elongation and seize to grow presumably due to the stress built on the cell wall. Since we study the growth of cell wall in three-dimensions as oposed to the 2-D projection, I take a series of z-sectioning at each time point of observation.

The effectiveness of directly labeling at the surface amine groups strongly depends on the cell density in liquid culture. I test the labeling first on the lab strain PY79 of *B. subtilis*. In the early exponential phase of growth, PY79 cells form long chaining cells of length over 50 to 100 μm. These chaining cells have segmented cytoplasm and closed septa between cells, yet the PG between cells is still connected. When reaching stationary phase, PY79 cells start separating and expressing genes responsible for motility, chemotaxis and other stress responses[21]. I find that the labeling works well on the chaining cells, but the short cells at late growth stage have very low labeling density following the same procedure. Wild type strain 3610 on the other hand does not form chaining cells even at early exponential phase, and consistently hard to

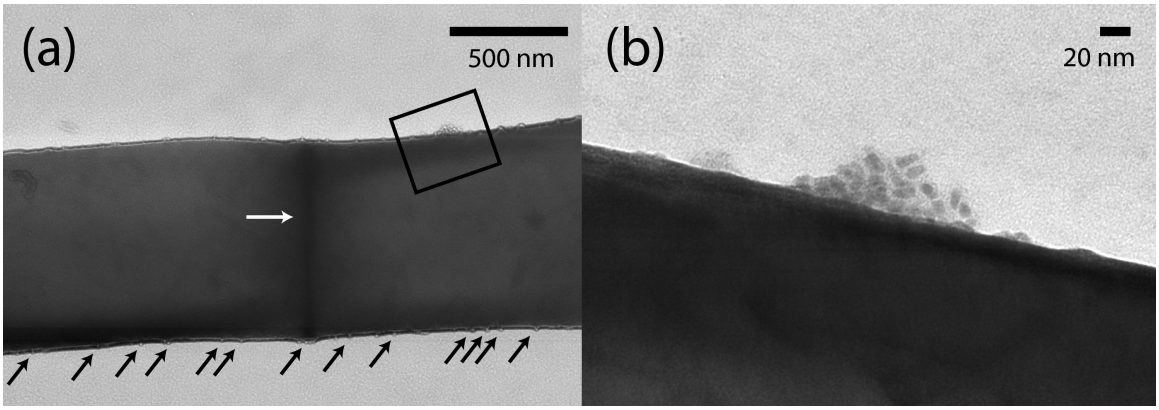

Figure 4.1: TEM images of quantum dot decorated *B. subtilis* cells on the primary amine groups on the cell surface. (a) Quantum dots appears as bright bulges that attach on the cell surface, indicated by the black arrows. The white arrow points at the septum between two daughter cells that are not separated. (b) The zoomed-in image of the edge of the cell surface indicated by the black box in (a). Several quantum dots form a cluster that attaches to the cell surface. The imaging focus has been adjusted so that quantum dots appear as dark particles of size 4×10 nm

label. It was found in [77] that *swrA*, a gene that is required for swarming behavior in *B. subtilis* is directly related to the chaining phenotype, and PY79 indeed contains a unique mutation in *swrA*[77]. The *swrA* knockout mutant, DS215[1] shows similar chaining phenotype and the labeling property as PY79 at different growth stages. The reasons of the correlation between swarming, chaining and surface labeling is unclear. I hypothesis that flagella may contribute to the connection.

B. subtilis in the wild spends most of the time in the soil underground, and thus it develops sensitivity to light. It is known that *ytvA* in *B. subtilis* is responsible for sensing blue light through the LOV (light, oxygen and voltage) domain on YtvA photoreceptor. The activation of YtvA then triggers the general stress factor σ^B, which then induces the activation of over 100 genes that prepare the cells to deal with the stress (see review [60]). In addition to blue light, it is later reported that red light also triggered the stress signal factor at lower sensitivity than blue light through energy stress branch of the σ^B activation, yet the specific receptor responsible for sensing

[1]We thank the Losick Lab at Harvard University for helping with this strain.

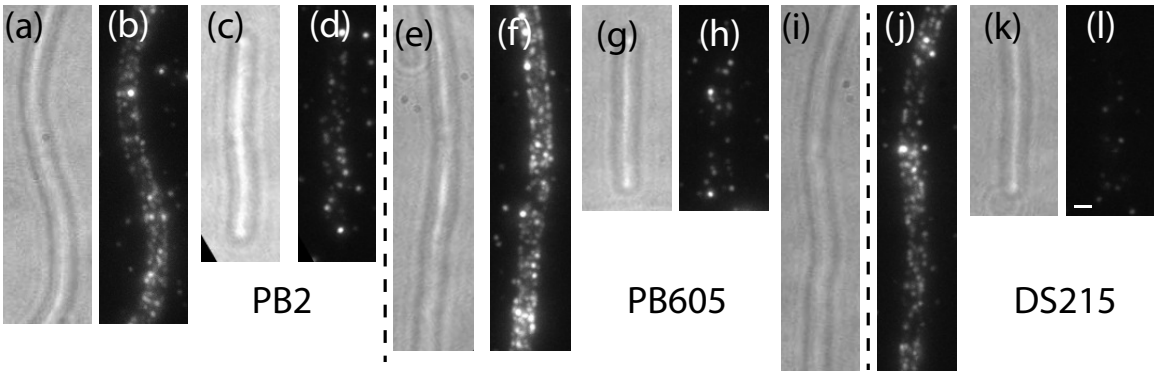

Figure 4.2: Fluorescent images of *B. subtilis* labeled with QDot655 on the surface amine groups. Bright field images (a, c, e, g, i, k) and maximum intensity projection of z-stacks (b, d, f, h, j, l) are shown for three different strains: PB2 (wild type, a-d), PB605 ($\Delta rsbQ$, e-h) and DS215 ($\Delta swrA$, i-l) grown to optical density 0.1. Chaining cells in all three strains have higher labeling density than short separated cells. All panels share the same magnifications indicated by the 1 μm scale bar in (l).

red light was not identified[8]. The sensitivity to blue and red light limits the fluorescence excitation wavelength and power, as well as the exposure to excitation light per unit time. Under blue or strong green illumination, I observe that initially growing *B. subtilis* cells stop growing in 5 minutes time scale and start shrinking if the illumination intensity is strong. Blue light illumination directly inhibit the PBP and MreB motion (personal communication with Ethan Garner at Harvard University), which indicates the microscopic mechanism of the overall inhibition of cell wall growth. For the photosensitivity reason, even tough quantum dots have better quantum efficiency at ultraviolet and blue wavelengths, I use green 532 nm laser illumination. To further reduce the photosensitivity, I used a background strain PB605[2] that has a knockout of $rsbQ$, which is responsible to trigger the energy stress[8].

Taking considerations of cell labeling, immobilization and photosensitivity into the account, I design the experimental protocol as the following. Quantum dot with emission maxima at 655 nm is chosen as the fluorescence marker to decorate *B. subtilis* strain PB605←DS215, using either WGA mediated labeling or direct amine labeling

[2]We also thank the Price Lab at University of California, Davis for helping with the strain

in phosphate-$MgSO_4$-glucose buffer. Cells are pressed between coverslip and 0.3% agarose gel in LB without NaCl before fluorescence imaging. To correct stage drift, a bright field z-stack image series is taken every 30 seconds, and the pixel value variance is used to correct for the z-drift, while direct image correlation corrects the translational drift. Typically, a fluorescence image stack of 15 images are taken at every 180 seconds with inter-frame distance of 150 nm, which translates to 133 nm in imaging plane because of the index of refraction difference between glass and water. The exposure time of each section is 0.2 seconds at an illumination intensity 1 W/cm^2 at a wavelength of 532 nm. Images are taken on the same AFM-microscope setup described in Chapter 2. 532 nm excitation laser is given by a 20 mW home-built diode laser system. Green laser is sent to the specimen by a single edge dichroic mirror (Semrock FF560-Di01). Appendix C lists the details of the laser controller design.

4.3 Extracting growth map from three-dimensional fluorescence movie

4.3.1 Unwrapping long *B. subtilis* cells

To show that we only label the surface of the cells, the fluorescence intensity projection along the cell axial direction is shown in figure 4.3, which indeed results in a hollow ring. With a high density labeling on the cell surface, and three-dimensional image stack, the distribution of the quantum dots can be extracted. The motion of the quantum dots in 3D contains information of the cell wall growth pattern. In principle, it is possible to extract the motion of each quantum dot in 3D followed by the reconstruction of the growth map. However, in the case of normal cylindrical growth, the deformation of the wall is constraint on the two-dimensional surface. Therefore,

it is practical to only look at the two-dimensional cylindrical surface assuming that cell radius is a constant.

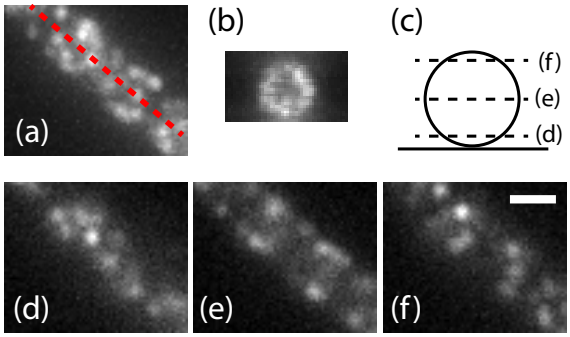

Figure 4.3: The three-dimensional distribution of the quantum dots that label the surface of *B. subtilis* cells can be indicated by the set of fluorescence images taken at multiple focal depths. (a) The maximum intensity projection along the optical axis (z direction) of all frames in a z-stack. (b) The maximum intensity projection along the cell axis indicated by the red dashed line in (a). (c) A cartoon to show the position of individual sections in (d)-(f). All panels have the same magnifications indicated by the 1 μm scale bar in (f)

Because the cell shape is a curved cylinder, it is natural to build a curved cylindrical coordinate around the cell, which requires to first locate the cell centerline. From the image stacks of dense quantum dots, I use an active contour model to detect the cell centerline. In brief, the centerline of a cell is modeled as an elastic open contour, and the images are treated as an external potential field that exerts force to the contour. The minimum-energy configuration of the contour is the detected position of the centerline. To convert the image to a potential field, I convolve the raw image stack with the Laplacian of the Gaussian (LoG!!!FIX!!!) kernel in 3D: $-\frac{r^2-2\sigma^2}{\sigma^4}\exp(-r^2/2\sigma^2)$, where r is the distance to the origin in a spherical coordinate, and σ is the length scale of the Gaussian, and I assign it as the cell radius so that the cell centerline is a minimum potential if the quantum dots are densely distributed. In practice, combined with a proper contour stiffness, the LoG kernel correctly converge

the contour to the centerline of the cell in 3D. More details and examples of the open active model can be found in Chapter 7.

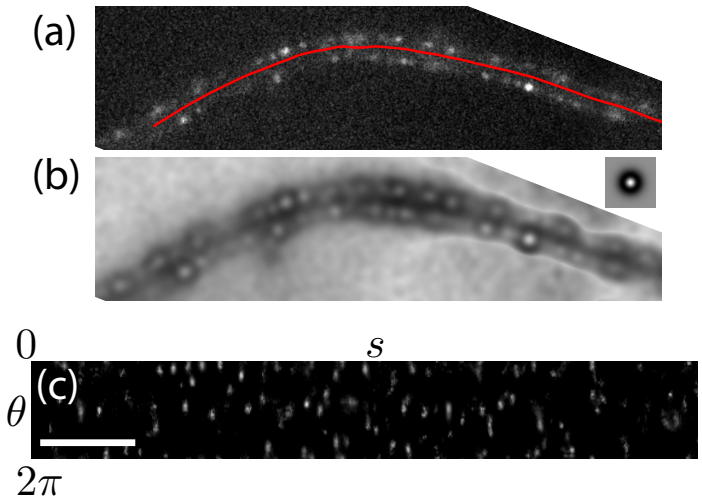

Figure 4.4: The cell centerline is detected using active contour model, and the fluorescence intensity of the surface markers are projected along the radial direction to give an unwrapped two-dimensional image. (a) A long chaining *B. subtilis* cell centerline is detected and labeled by a red line. (b) To track the cell centerline, the original z-stack is convolved with a "Mexican-hat" shaped kernel. The centerline and the cell surface where the quantum dots locate have the maximum contrast. Inset: the convolution kernel. (c) The fluorescence intensity in 3D is projected along the radial direction of the curved cylindrical coordinate about the cell centerline. Scale bar is 5 μm.

After the centerline is obtained, I build a curvilinear cylindrical coordinate (s, θ, r) about the centerline of the cell, where s is the axial arc position, θ is the polar angle, and r is the radial distance from the centerline. In my observations, normal *B. subtilis* cell curvature is typically greater than 50 μm, much greater than the cell radius of 1 μm, and because the cells are confined between glass coverslip and agarose gel, the height variation is negligible. Thus, it is a good approximation that (θ, r) plane up to $r \sim r_{cell}$ is still locally flat, and one can use an undistorted cylindrical coordinate with a fixed $\theta = 0$ direction parallel to the image plane to describe the three-dimensional position near the cell centerline (figure 4.4). In this coordinate system, the fluorescence intensity is a function of (s, θ, r), and I project the intensity along the r direction with a Gaussian weight function peaked at $r = r_{cell}$:

$r \exp[(r - r_{cell})^2/2\sigma^2]$, taking into account the metric of a cylindrical coordinate. The projection on the $r = r_{cell}$ surface effectively "unwraps" the intensity distribution on the cell surface into a flat two-dimensional plane (figure 4.4).

4.3.2 Mathematical description of cell growth

The growth of the cell wall indicated by the 3D motion of the quantum dot markers can be represented by the morphological deformation of the unwrapped intensity map and the motion of the centerline, whose curvature remains small in the beginning of the growth, typically hours before buckling becomes significant. Under the constraint of normal growth that the cell radius remains constant, the cell wall has two possible kinds of allowed deformations: elongation and twisting. In the representation of the unwrapped surface, elongation and twisting become stretching and shearing. In general, the instantaneous velocity of a point on the surface can be written as $\mathbf{v}(s, \theta)$ with two components $v_s(s, \theta)$ and $v_\theta(s, \theta)$. The growth rate tensor is the spatial gradient of the velocity:

$$\mathbf{R} = \nabla \mathbf{v}(s, \theta), \tag{4.1}$$

which has four components with physical meaning of axial elongation rate, circumferential growth rate, twisting rate, and axial shearing rate. Note that the velocity gradient tensor $\mathbf{R}$ is not the strain rate tensor, which is defined as

$$\mathbf{D} = \frac{1}{2}(\mathbf{R} + \mathbf{R}^T). \tag{4.2}$$

Limited by the imaging and labeling resolution practically, the velocity gradient along the circumferential direction and the shearing along the cell axis are too small to detect, or

$$\partial_\theta \mathbf{v}(s, \theta) \approx 0. \tag{4.3}$$

With this constraint, I effectively consider only two types of growth: circular insertion along the entire circumference of the cylindrical cell, and plain shear corresponding to twisting during growth, and v_s and v_θ do not have θ dependence. Thus in this section, it is more convenient to study the velocity gradient $\mathbf{R}$ instead of the strain rate tensor $\mathbf{D}$. The elongation and twisting rates are

$$R_e = \frac{\partial v_s(s,\theta)}{\partial s}, \tag{4.4}$$

and

$$R_t = \frac{\partial v_\theta(s,\theta)}{\partial s}. \tag{4.5}$$

In general, if one zooms in and look at the insertion at microscopic scale, the tip of a

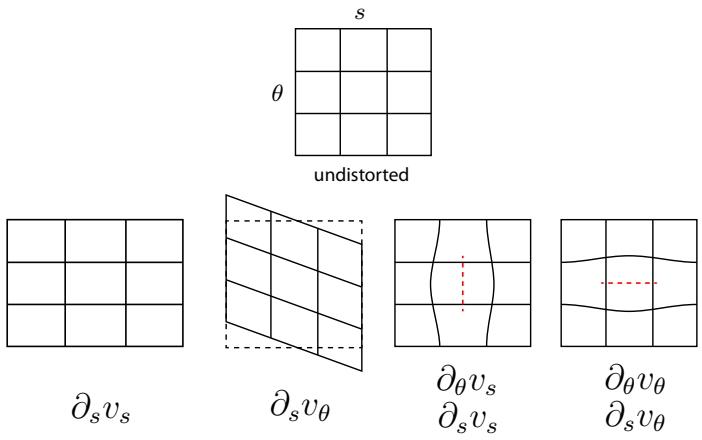

Figure 4.5: Demonstration of the effect of the four components of the growth rate tensor indicated by the deformation of a wireframe along the axial direction s and circumferential direction θ. $\partial s v_s$ and $\partial s v_\theta$ are the elongation and twisting, and the combinations with $\partial\theta v_s$ and $\partial\theta v_\theta$ correspond to the insertion along axial and the circumferential direction indicated by the red dashed lines.

newly inserted strand forms a dislocation, and the insertion of a finite length strand causes shear velocity gradient along the axial direction at the tip of the new strand, thus $\partial_\theta v_s(s,\theta)$ is not strictly zero, as long as the dislocations exist. I will neglect shearing along the axis, and only consider the circumferentially averaged growth and twist for experimental data.

4.3.3 Tracking single quantum dots for cell wall morphology dynamics

Each 3D stack at every time point can be unwrapped, and the collection of the unwrapped intensity can be visualized in the from of a kymograph of the intensity projection along the circumferential θ direction (figure 4.6(a)). It is readily clear that the growth of the cell wall is shown as the diverging traces, and similarly, the twisting during growth is shown as the nonparallel traces in the $\theta - t$ projection. Qualitatively, the elongation distributed all along the cell length, which is consistent with previous results that like many other rod-shaped bacteria, *B. subtilis* cell wall material insertion is distributed. In the growth kymograph, two groups of motion emerges, one being

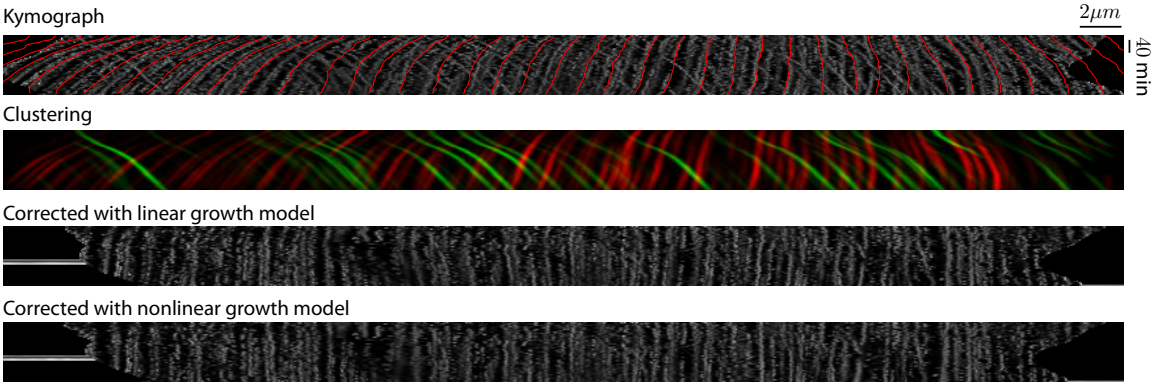

Figure 4.6: The projection of intensity kymograph of the unwrapped quantum dot fluorescence intensity on the surface of a growing *B. subtilis* cell along the circumferential direction, showing only the dynamics along the axial direction. (a) The kymograph in the Eulerian specification. Overlaid is the streamlines of originally equally spaced positions along the cell axis following the detected nonuniform growth. (b) Wall-attached quantum dots and detached dots move in two distinctive groups as shown in the kymograph (a). The probability distribution of traces of the dots belonging to the attached or the detached group of dots is shown in red and green respectively. (c) A spatially uniform but temporally nonuniform growth model can approximately describe the growth. In the Lagrangian specification where the coordinate follows the uniform growth model, the traces appear as nearly straight lines, and the deviation from straight lines suggests heterogeneous growth. (d) The kymograph in the Lagrangian specification under the heterogeneous growth model in both space and time. The stream lines following the heterogeneous growth model shown in (a) tracks the motion of individual dots better, as indicated by more parallely aligned traces in the kymograph in the Lagrangian specification.

the diverging growth traces, the other being non-diverging and pure translational. The presence of the second group is because the cells are in physical contact with the glass coverslip and the agarose gel, and the attached quantum dot can fall off the surface and stay stationary with the substrate rather than the cell wall. When extracting growth from the unwrapped movie, these detached quantum dots must be excluded.

In order to obtain the growth map, I first approximate the growth as a linear function of the position on the surface, where R_e and R_t are constants, or equivalently

$$v_s(s) = R_e s + v_{s0} \tag{4.6}$$

$$v_\theta(s) = R_t s + v_{t0}. \tag{4.7}$$

The linear growth approximation is applied to both the attached and detached quantum dots with different growth rates. The separation of the two groups is achieved iteratively following an expectation-maximization (EM) approach. Briefly, each location in each frame has a clustering probability of morphing with the attached group or the detached group, and it is calculated based on the difference between the local velocity and the predicted velocity of that location from the two linear growth groups using recently estimated growth rates. Since the attached and detached markers move continuously in time instead of reappearing randomly among the frames, the clustering probability distribution also has continuity in time that depends on the two linear growth respectively. After each location is associated with the two groups probabilistically, the growth rates are updated from least square fits with weights calculated from the image intensity and the grouping probability. This procedure is repeated till convergence.

More generally, even with the constraints in equation (4.3), the growth can be deviated from the linear growth as listed in equation (4.7). The deviation from

linear growth is clearly shown in figure 4.6(c) where the traces in the kymograph after correction with a linear elongation still appear locally converging or diverging. This observation suggests that the cell growth rate is not uniform along the cell, and linear growth model is not sufficient given the resolution achieved in our experiments. To refine the growth rates, I slice the unwrapped images into stripes spanning from $\theta = 0$ to 2π, corresponding to rings along the cell, and obtain the shift in both axial and circumferential directions using sub-pixel image registration routines[56]. The nonlinear, nonuniform growth is shown in figure 4.6(a), where the traces of locations with equal distance are shown in red on top of the kymograph.

In figure 4.6(a), the kymograph of the unwrapped intensity is described in a coordinate system that has the same metric as the lab frame, where the trajectories of the quantum dots appear as diverging traces. If the growth is treated as a fluid flow, such description of the dynamics of the flow field is called the Eulerian specification. The flow quantities in Eulerian specification are written as a function of the axial coordinate s and time t as used in the previous sections. It is also applicable to build a coordinate system that is attached to the motion of the flow namely the "Lagrangian specification", where the position is labeled with a time-independent vector, usually the position at an initial time t_0, in our case the initial arc position s_0. It is particularly useful to describe the morphological changes because in the Lagrangian specification, the kymograph of the quantum dots appears straight lines parallel to the time axis, and particular locations fixed on the cell, for example the locations of the septa, remain stationary (figure 4.6(c), (d)). Note that the Lagrangian specification is a non-flat metric, and thus the time derivative of a vector includes the change of the coordinate:

$$\frac{\mathrm{D}}{\mathrm{D}t} = \frac{\partial}{\partial t} + (\mathbf{v} \cdot \nabla), \tag{4.8}$$

where $\frac{\mathrm{D}}{\mathrm{D}t}$ is the total time derivative. As a trivial example, the speed of a point fixed on the cell wall at location $s(s_0, t)$ is

$$\begin{aligned} \frac{\mathrm{D}s(s_0,t)}{\mathrm{D}t} &= \frac{\partial s(s_0,t)}{\partial t} + (\mathbf{v}\cdot\nabla)s(s_0,t) && (4.9)\\ &= v_s\frac{\partial s}{\partial s} && (4.10)\\ &= v_s. && (4.11) \end{aligned}$$

The coordinate in the Lagrangian specification does not have temporal dependence, and thus the first term vanishes, and the velocity is included in the time dependent metric. In practice, the transformation between the two specifications is achieved with numerical interpolation.

4.4 Cell wall growth is heterogeneous

Following the routines of tracking the cell wall deformation, we obtain a velocity field in the Eulerian specification $\mathbf{v}(s, t)$, which can be transformed into the Lagrangian representation. To illustrate the morphological changes that a long *B. subtilis* chain undergoes, a set of constant $s(s_0, t)$ and $\theta(s_0, t, \theta_0)$ at equal distance is displayed as time progresses (figure 4.7). Effectively, the equally spaced grid lines act as fiducial markers that resembles the motion of the quantum dots but appear in more regular patterns. Note that due to the intrinsic blinking of quantum dots, only a portion of the quantum dots are visible in each frame. The elongation is indicated by the horizontal expansion, which settles at an unevenly distributed spacing between grids, suggesting that the elongation rate is also uneven along the cell length. Meanwhile, the grid is sheared along the circumference to both positive and negative directions, suggesting that the local shearing or twisting is highly active and variable.

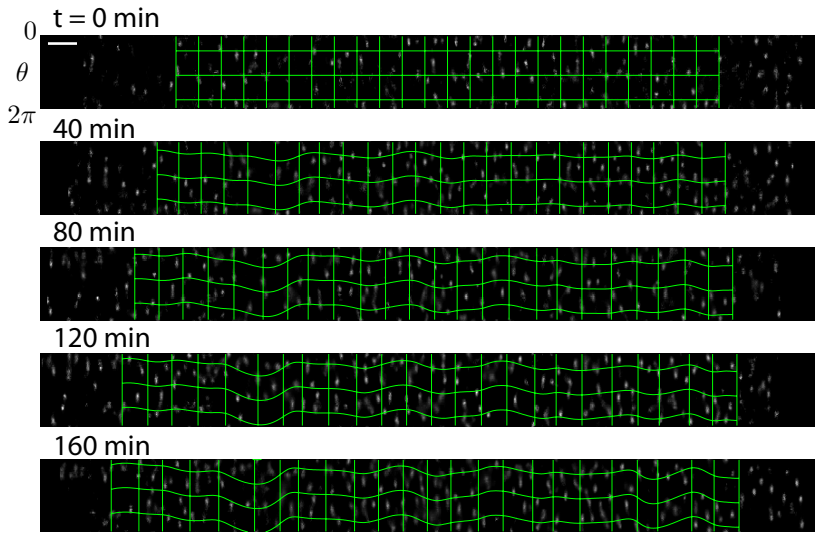

Figure 4.7: The temporal evolution of fiducial grid lines generated based on the growth map of a *B. subtilis* cell chain shows the morphological changes of the unwrapped cell surface at different time when the cell is growing. Both axial elongation and circumferential distortion due to twisting are observed.

The heterogeneous growth and twist of the cell unwrapped in figure 4.7 are better shown in the strain rate distribution as functions of the arc position along the cell and time. Figure 4.8 (a) and (b) shows the elongation rate $\partial_s v_s(s,\theta)$ and twisting rate $\partial_s v_\theta(s,\theta)$ in the Lagrangian specification, so that the values at a constant arc position represent strain rates at a fixed position relative to the cell instead of a fixed point in space. Due to the finite labeling density in this specific example, the spatial resolution is limited to a sub-cellular length of 1 μm. The growth maps show that the elongation rate and twisting rate are highly heterogeneous in both space and time. The elongation rate is overall positive, but fluctuates at typical spatial scale of 5 μm. The cause of this variability is possibly due to the intracellular growth heterogeneity, or the differentiation among individual compartmentalized cells in a long chain. The high growth or twisting activity on these "islands" persists in time typically for 10 to 30 minutes, which is the relevant time scale of the formation of new septa in these chaining cells. How the pauses between active growth relate to the septa formation, or whether other factors cause the pause remain unidentified.

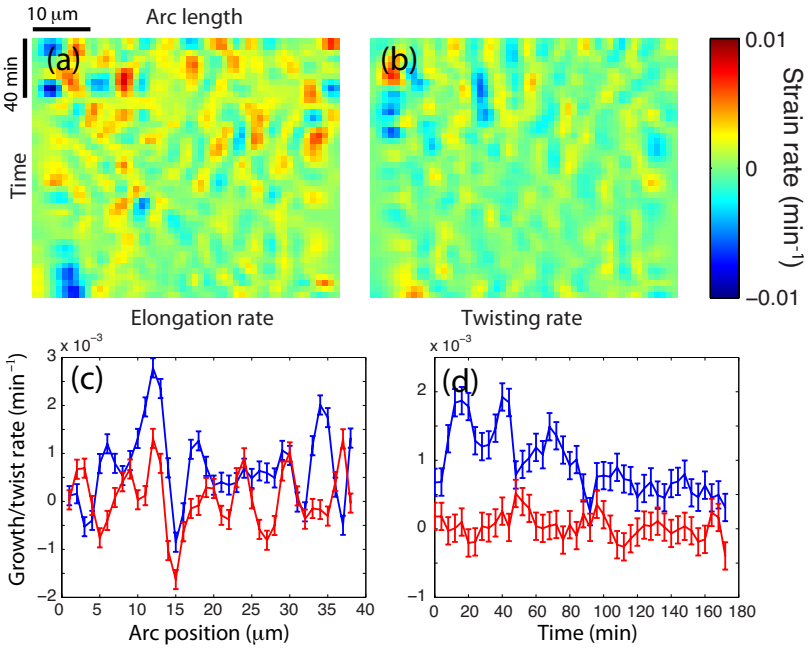

Figure 4.8: Growth map of the same *B. subtilis* cell chain as in figure 4.7. (a) Elongation rate as a function of time and arc position along the cell length in the Lagrangian specification. (b) Twisting rate as a function of time and arc position. (c) The time average of the elongation (blue) and twisting (red) rates as functions of the arc position. (d) Overall strain rates across the entire length of the chaining cells as functions of time.

When the cell growth is described in the Lagrangian specification as in figure 4.8(a) and (b), the dependence of growth rate only on the arc position can be obtained by simply averaging over the time as shown in figure 4.8(c). Both elongation and twisting rates show strong periodic pattern in the temporal average, suggesting that the active and inactive growth regions remain relative stationary relative to the cell at cellular spatial scale, in contrary to the proposed uniform insertion model at molecular and sub-cellular level. The spatial average of the growth and twisting rates are shown in figure 4.8(d). The overall twisting has a much small variability if averaged over 50 μm than at shorter cellular length scales, indicating that both left-handed and right-handed helical growth are present at nearly equal probability. The elongation rate has three major peaks of growth, but slows down due to the stress response caused by the excitation illumination.

4.5 Discussions and outlooks

In this chapter, I introduce a framework to quantitatively study the cell wall insertion dynamics in live *B. subtilis* cells using fluorescence nano-motion capture. The morphological changes of the cell wall is indicated by high density of fluorescence markers, and is determined to better than sub-micrometer resolution at tens of nanometer accuracy, and with minute temporal resolution. The spatial and temporal resolution far exceed existing method that attempted to resolve the growth dynamics of the bacterial cells, and for the first time provide the complete three-dimensional information. By projecting the fluorescence intensity on the curved cylindrical surface of the cell onto a plain, the problem is simplified to tracking the morphology of a two dimensional membrane. The dynamics of the morphology is described by the normal and shearing strain rates, corresponding to elongation and twisting. I show that both elongation and twisting are highly heterogeneous at sub-cellular spatial scale, and vary temporarily at a time scale of 5 minutes. Spatially, both elongation and twisting appear compartmentalized at a typical scale of 5 μm, which is in accordance with the length of single *B. subtilis* cells.

Several reasons can give rise to this heterogeneity in growth rate along the cell length. It is well known that in many rod-shaped bacteria such as *E. coli* and *B. subtilis*, the old poles are inert, meanwhile the density of PBPs at the old poles is lower than the mid-cell for unclear reasons[17]. In chainning *B. subtilis*, even thought remaining attached, the cells are separately by complete septa and intact cell membranes between one another. Near the septa, the growth rate can be slower than the mid cells, and thus a heterogeneous growth is expected. It is also possible that the segregated cells have independent and different growth rates due to the intrinsic noise in gene expression[91]. In filamentous cyanobacteria, cells are able to undergo heterocyst differentiation that forms spatial patterns spontaneously or in accordance with environmental signals[94]. The differentiation between individual cells can be

another reason to give rise to the micrometer-scale growth heterogeneity. Different from chaining but segregated cells, another type of filamentous cell morphology can be obtained by inhibiting the septum-forming protein PBP-3 (FtsI) with cephalexin or aztreonam in *E. coli*, in which case the PBP-3 protein is recruited periodically to form ring structures along the cell length[159], but unable to close the PG to form septa. In this case, the cytoplasm is connected, and inter-cellular differentiation is suppressed. However, the recruitment of the septal proteins such as FstZ and FtsI is still present in filamentous cells[159]. Is the periodic growth pattern expected in the filamentous cells? In other words, is the spatial localization of the Z-ring, the existence of a closed septum, or the cellular differentiation what causes the nonuniform growth? By looking at the growth pattern at sub-cellular scale resolved by the growth map, these question can be addressed to help understand the spatial distribution of the cell wall synthesis complexes and their roles in growing cell wall and forming septum.

The localization of the PG synthesis complexes ultimately determines the pattern the cell wall grows[51, 48, 150], and the former has been observed experimentally that the PBP complexes form diffraction-limited spots on the membrane of the cells, both in gram-positive and gram-negative bacteria, and translocate approximately along the circumferential direction. This processive motion is the basis for providing a global PG insertion order, which is suggested to be essential for a robust elongation where the radius of the cell and PG cross-linking density remain constant along the cell. However, the correlation between the PG synthesis complex locomotion and the growth pattern has never been directly shown. The quantum dot labeling density can be well above 10 μm^{-1}, whereas the distance between fluorescently labeled PBP-2 in *B. subtilis*[51] and MreB in *E. coli*[150] is typically over 500 nm. The sub-minute temporal resolution of the growth map is sufficient to capture the cell wall morphological changes given that the translocation speed of these protein complexes is typically

600 nm/min. Our framework of quantitatively study cell wall growth dynamics is a platform potentially capable of bridging the molecular growth mechanism and the global cell morphology.

As the work in this thesis is in progress, the Huang Lab is investigating growth pattern in gram-negative bacteria *E. coli* also by fluorescently label cell wall and observe the growth. In their work, they use WGA tagged with organic dye to create a nonuniform staining pattern on the cell envelope, and track the motion of these features on the circumference of the cell envelope in two-dimensional projection. Due to the limitations of using continuous labeling instead of individual marker as discussed in the previous section, the spatial resolution of their approach is typically above micrometer. Also, the 2D projection drops all motion information in 3D, thus unable to resolve twisting during cell growth. In fact, in case of a helical growth, the elongation and twisting will have a mixed contribution to the 2D projection of intensity on the circumference, and cause complication to the motion tracking.

One limitation of our experimental setup is the requirement to immobilize cells on the surface for imaging. I used agarose gel as a physical constraint to press cell on the glass coverslip, where I observe two major drawbacks. Firstly, the cell elongation involves deforming agarose gel at the tips of the cells, which effectively forms a resistive force to cell elongation. I have observed that for higher agarose gel stiffness or higher pressing force over the cell, the cell tend to grow into more s-shaped curves with an averaged curvature of 5-10 μm, and eventually stalled. Secondly, the physical contact between cell and glass coverslip increases the probability of quantum dots detaching from the cell wall, and the detached quantum dots stay stationary to the coverslip, complicate the motion tracking, and reduce the density of the moving quantum dots. Purposely designed microfluidic devices potentially provide a solution to the immobilization problem. For instance, the "mother machine" developed by Wang *et al* has been used to observe rod-shaped *E. coli* growth[154] and to measure

the mechanical property of the filamentous cells. In such setup, the free end of the cell does not experience any mechanical constraint and is free to elongate and twist. The detachment due to the turnover of the PG will not complicate the analysis because the detached quantum dots will quickly diffuse away. It is also applicable to apply the labeling and washing all on the same device, or to restore the labeling density after the dilation due to PG insertion. It is plausible that the combination of the nano-motion capture assay with microfluidic techniques will help provide cell wall growth map at higher resolution and at more natural conditions.

The choice of quantum dot as the marker allows to observe cell growth with little photobleaching, and sub-diffraction limit density can be achieved on live cells, while dimmer quantum dots requires brighter excitation intensity. The outstanding resistance to photobleaching makes photons cheap, granting higher signal-to-noise ratio in each frame, better z-resolution by having more sections in each stack, and better temporal resolution. However, the total photons obtained per unit time is then limited by the tolerance of *B. sutbilis* to light instead of the fluorescence marker. Even with the introduction of the *rsbQ* deletion as suggested in [8], the cells are still only able to grow with an already compromised rate under 1 W/cm^2 532 nm light illuminated during exposures that take 1% time, and more intensive illumination will generally inhibit growth. To address this issue, I developed an optically selective mutagenesis assay, where bacteria in a droplet of growth medium grow under nonuniform green light illumination at an averaged intensity of 0.2 W/cm^2 (figure 4.9). It is reported that for accelerated selective mutagenesis requires both gradient of selective pressure and cell motility[168], which are satisfied in the "droplet under light gradient" design, although a more ideal configuration would be similar to the "death galaxy" as described in [168] under a nonuniform illumination. After around hundreds of cell cycles, a mutated strain of parent strain PB605←DS215 develops significantly higher resistance to green light and is able to grow under 10 times brighter 532 nm laser

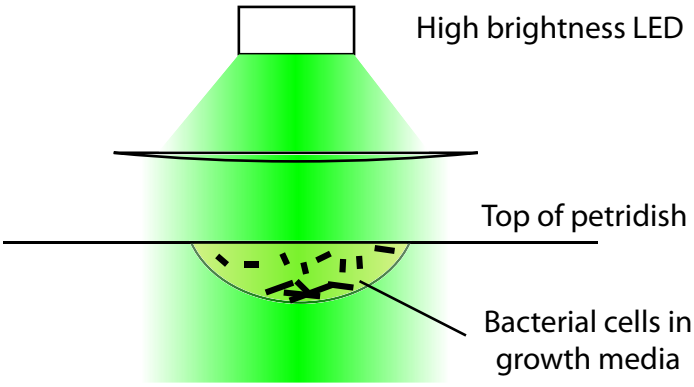

Figure 4.9: A schematic figure of the green-light resistance mutagenesis setup. A 5 microliter drop of growth media containing *B. subtilis* is placed under constant illumination at 0.2 W/cm^2 from a high brightness green LED. The high tolerance to green light allows taking fluorescence images at higher intensity, finer z-sectioning and better temporal resolution.

illumination than its parent strain. I did not observe apparent morphological difference from the parent strain, nor the growth rate had any difference. The sequence of this new strain is to be investigated yet, and it is likely to improve both spatial and temporal resolution of the growth and finally reach molecular scale.

Chapter 5

Breaking the Diffraction Barrier by Spatial Covariance Reconstruction (SCORE) Microscopy

5.1 Diffraction Limit and Super-resolution Imaging Techniques

In Chapter 4, I describe a new method to observe bacterial cell wall growth dynamics using fluorescence microscopy. Due to the small size of bacteria and the high labeling density, it is a technical challenge to resolve the spatial distribution of all the individual fluorescence marker. More generally, far-field light microscopy is an essential non-invasive probing tool in many fields of biology and biophysics, especially for life imaging *in vivo* and *in vitro*, yet it is the intrinsic physical property of light that determines how much one sees through any kind of optical microscopy technique.

The information provided by fluorescence imaging is essentially limited by the resolution, defined as the finest structure that the imaging technique is able to resolve, and the resolution is critically limited by the diffraction of the objective aperture.

Recently, several novel imaging techniques has been developed aiming to break the diffraction limit. These super-resolution techniques can be roughly categorized into three different types. The first type utilizes a spatially or temporally engineered illumination pattern to either reduce the volume of the detected target in a controllable way such as in stimulated emission depletion (STED) microscopy[61, 79, 62] or using reversible saturable optical fluorescence transitions (RESOLFT)[66], or encode the spatial information into other low-frequency signals such as in saturated structural illumination microscopy (SSIM) where angular or temporal responses of the fluorophore s were used as spatial information carriers[57]. These types of imaging techniques usually require much higher excitation or switching power than conventional epi- or confocal fluorescence microscopy, and may cause phototoxicity and photodamage in certain biological systems. The optical complexity and cost are other factors that also limit the application of these methods.

The second group of methods resolves the distribution of fluorescent sources based on single particle localization. Stochastic optical reconstruction microscopy (STORM) [119] and photo-activated localization microscopy (PALM) [15, 64] were developed and achieved a resolution of 10 nm by sequentially activate single emitters and localize them individually at a precision beyond diffraction[163]. However, the limitation of STORM/PALM lies in the fact that the resolving ability is based critically on the spatial separation of emitters, thus limiting the number of emitters resolved in each frame. A reconstructed image usually requires a minimum of 10^4 images, or tens of minutes of imaging time [37]. Live cell imaging still remains challenging to all approaches mentioned above. Aiming at obtaining high information density by looking at more densely distributed bright emitters, Holden *et al* applied the principle of an astronomy software package that was capable of separating closely located Gaussians to super-resolution imaging and introduced DAOSTORM [67]. Compressed sensing STORM (CSSTORM) and deconSTORM also address the

same overlapping PSF problem and are able to work with 5 to 10 times higher density of switched on emitters[170, 102] Higher emitter density remains challenging for these essentially single emitter localization based methods.

Instead of resolving the localization of emitters based on single switching events, the third group of approaches extracts the localization information from the statistics of the pixel intensities, therefore overlapping is no longer a limiting factor but rather preferred since higher density of emitter provides higher intensity variance. Many different kinds of emitters including fluorescent protein, organic dye[37] and nano crystal[105, 126] have particular temporal intensity fluctuation patterns, or fluorescence intermittency (FI). Super-resolution optical fluctuation imaging (SOFI) was developed based on the independence of the emitter intensity fluctuation, and effectively reduced the PSF width by taking the simple temporal cumulant of the pixel intensities[39]. SOFI was then improved by including spatial cross-cumulant in intensity fluctuation[40]. For the same principles, Lidke *et al.* resolved the location of densely distributed individual quantum dots from the spatial covariance of the pixel intensity fluctuation and independent component analysis (ICA)[87]. This method is shown to be applicable to a small number of sources but becomes intractable if the number of emitter reaches 10, and thus is not applicable to resolving continuous structures. A realistic model that optimizes the location and blinking of emitters was built by Cox *et al* to give super-resolution images at a greatly improved temporal performance of seconds[30]. The computation complexity of this global optimization is however extremely high, making it unideal to use. These statistical methods in practice reaches a resolution of 100 nm, slightly poorer than the single particle localization techniques but requires much less number of frames, typically in the range of hundreds to thousands.

In this chapter, I introduce an image reconstruction algorithm in the third category named spatial covariance reconstructive (SCORE) microscopy. I start from the

fluorescent intensity covariance between pixels of a stack of images, combine the prior knowledge of the shape of the point spread function (PSF) to map the distribution probability of individual emitters. Our method inherits the advantages of previous statistical approaches including insensitivity to background, no upper limit to the fluorescent emitter on-time thus allowing higher information density per frame and much lower requirements on number of frames, and easiness of implementation from standard epi-fluorescence setups. Through principle component data compression, I only consider components that have significant contribution to the variance of pixel intensities, and thus reduces the noise and computational cost. I quantitatively compare the results of STORM and SCORE in simulations, where the quality is defined as the Kullback-Leibler divergence from the ground truth to the resulted images. As demonstrations, I applied SCORE on microtubule in HeLa cells labeled with organic dye and quantum dots, and in both cases I am able to achieve sub-diffraction resolution of 100 nm within a few seconds of imaging. The resolution is limited by our labeling quality, and better imaging quality can be obtained using existing selections of fluorophore that have more robust intensity fluctuation.

5.2 Image reconstruction model

In a series of fluorescence images of a specimen taken at different time, I assume that the fluorescent emitters locate at a finite number of fixed locations in space $\mathbf{x}_m$, where m is the index of the position: $m = 1, 2, \ldots, M$. Here I do not place constraints on the distribution of x_m, thus they can be arbitrarily dense locally or even overlap. Each emitter undergoes statistically independent fluctuation in intensity that follows particular statistics depending on the nature of the emitters, which can be organic dye, fluorescent protein or nanocrystal. Let one record a sequence of T images of these flickering or blinking emitters, in which the instantaneous intensity of each emitter is

$s_{m,t}$ with $t = 1, 2, \ldots, T$. The independence condition of the intensities from different emitters is equivalent to $P(s_{m,t}, s_{n,t}) = P(s_{m,t})P(s_{n,t})$ for $m \neq n$. Each emitter is imaged as a diffraction limited spot described as the point spread function (PSF), which can be approximated as a Gaussian function in two dimensions. The width of the PSF depends on the imaging wavelength, the numerical aperture of the objective and the axial distance from the focal point. In our model, I assume the PSFs are identical, or equivalently demand that the sources are localized in a 2D plane. The more general three dimensional case will be discussed later. Let the individual PSF be $f(x_i - x_m)$, which is the intensity value of the i^{th} pixel at location x_i of a 2D Gaussian function centered at the mth source location x_m. The temporal sequence of image pixel intensity in the noise free case is $I_t(x_i) = \sum_m f(x_i - x_m)s_{m,t}$. It can be written in vector notation $I_t(x_i) = \mathbf{f}^T\mathbf{s}$, where $\mathbf{f} = (f(x_i - x_1), f(x_i - x_2), \ldots, f(x_i - x_M))^T$, and $\mathbf{s} = (s_{1,t}, s_{2,t}, \ldots, s_{M,t})^T$. The observed pixel intensity recorded by a camera is corrupted by the photon arriving shot noise and the measurement noise.

The problem of reconstructing image is to fine the best estimate of the collection of the centers of the PSF $\mathbf{x}_m$ from $\hat{I}_t(x_i)$, assuming that f is a known Gaussian and $s_{m,t}$ follows mutually independent and identical statistics (figure 5.1). The difficulty of globally optimizing the emitter locations and intensity sequences lies in the fact that the number of emitter m is unknown and the parameter space is high-dimensional. It helps to reduce the dimension of the problem by truncating the principle component of the data set above the noise level as suggested in [87]. Instead of seeking the solution in terms of the location of each emitter as done in [87], I coarse-grain the set of center locations x_m onto a finite mesh grid at x_k, $k = 1, 2, ..., K$, usually an up-sampled mesh of the camera pixel array, and on each grid resides an emitter with fluctuating amplitude a_k. Statistically, a_k scales with the square root of the local emitter density to resemble the identical covariance.

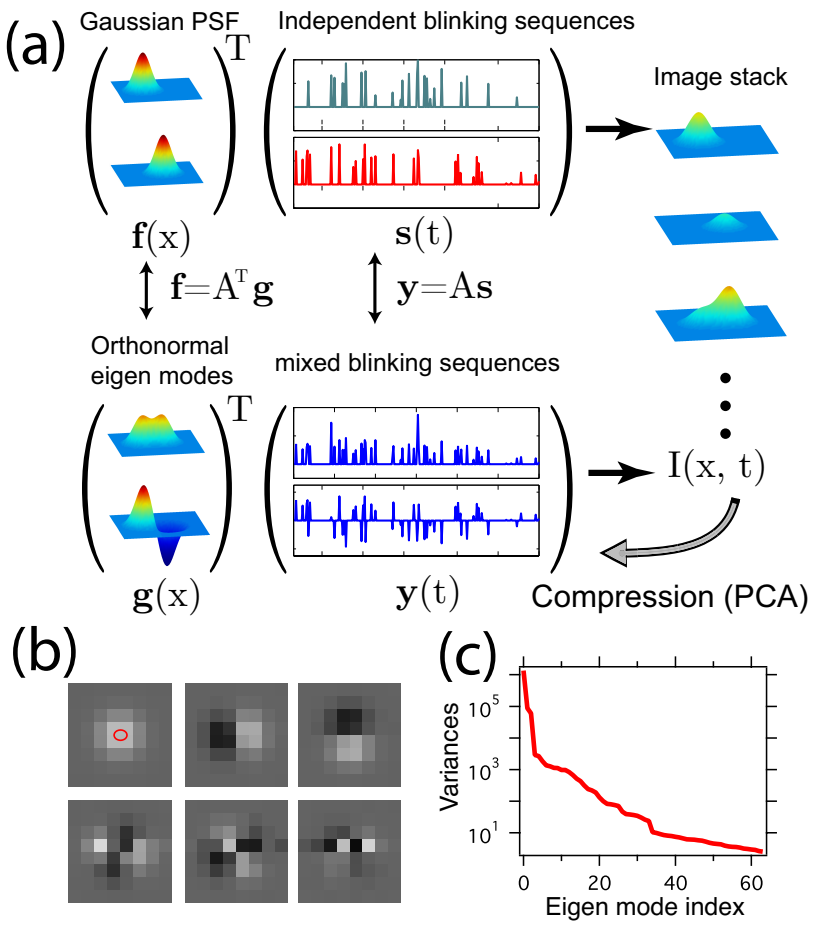

Figure 5.1: The principle of SCORE is illustrated in a simulated data. (a) Each of the two emitters gives a Gaussian shaped point spread function $f(x)$, associated with a temporal blinking sequence $s(t)$ that is independent one another. The product of the spatial profiles and temporal sequences is the observable images, which can be transformed into a set of orthonormal eigen modes $g(x)$ and associated mixed fluctuation sequences $y(t)$. The distribution of the emitters can be found by measuring the distance between a Gaussian and the subspace span by the eigen modes that have sufficient energy above noise. (b) First 6 eigen modes of an ellipse. (c) The sorted variances of all the 64 eigen modes.

Specifically, the covariance matrix between pixels of an image stack is defined as

$$C_{ij} = \langle (I_t(x_i) - \langle I_t(x_i) \rangle_t)(I_t(x_j) - \langle I_t(x_j) \rangle_t) \rangle_t \tag{5.1}$$

where $\langle\ \rangle_t$ takes the average over time index t. The normalized eigenvectors of C_{ij} forms a set of orthonormal basis that explains the variations of pixels in groups, while

the corresponding eigenvalues are the variance explained by these eigen modes. In the principle component analysis, eigenvectors with variance greater than a threshold are usually kept as meaningful signals while the rest are treated as noise and are omitted. The sorted variance typically shows a kink clearly separating signal from the noise background (figure 5.1). I take the threshold at the kink of the variance, and let N be the number of eigenvectors that have significant variances, and eigenvectors be $g_n(x_i), n = 1, 2, \ldots N$, or $\mathbf{g}$ in the vector notation. Note that N is typically much smaller than the true value of number of emitter M due to the noise. The truncated set of eigen modes is a compressed representation of the original pixel intensity covariance. Gaussian modes centered at emitters with the correct width can be recovered from the truncated set $\hat{\mathbf{g}} = (g_1, g_1, ..., g_{i_0})^T$, whereas falsely located Gaussian modes is far from the linear space spanned by the truncated set, because these mis-placed modes do not contribute variance to the covariance, and therefore are dropped in the compression process. As an extremely example, in the noise free case, the eigen subspace of a small number of individual fluctuating Gaussians intersects with the whole set of Gaussian function precisely at the true locations of the sources. I generalize this property into higher number of individual emitters in presence of noise to estimate the likelihood based on the Euclidean distance from the eigen mode subspace to a Gaussian function:

$$D(x_0; \hat{\mathbf{g}}) = \frac{\|\mathcal{G}(x_0, \sigma) - \left[\mathcal{G}(x_0, \sigma)\hat{\mathbf{g}}^T\right] \hat{\mathbf{g}}\|}{\|\mathcal{G}(x_0, \sigma)\|}, \tag{5.2}$$

where $\left[\mathcal{G}(x_0, \sigma)\hat{\mathbf{g}}^T\right] \hat{\mathbf{g}}$ is the projection of a Gaussian function centered at x_0 on the compressed subspace $\hat{\mathbf{g}}$, and $\|\cdot\|$ takes the L-2 norm. This distance distribution is mapped to a probability-like distribution by treating the distance as the residual of

the maximum-likelihood fit:

$$a_k = \exp\left(-\frac{D^2(x_k;\hat{\mathbf{g}})}{2h^2}\right), \tag{5.3}$$

where h is an imperial parameter that can be determined by the scale of maximum gradient allowed in the reconstructed image. This parameter can be determined if a desired maximum gradient magnitude of the reconstructed image is given:

$$\nabla_k^2 a_k = \frac{I^2 D^2}{4h^4}\nabla_k^2 D(x_k), \tag{5.4}$$

from which h can be implicitly solved. In this emitter distribution reconstruction method, the truncation of eigen modes plays the key role in rejecting Gaussian functions that do not contribute to the variances. The resulted image is however insensitive to the precise choice of the truncation threshold. One can apply other criteria to determine the likelihood of a Gaussian from the whole set of eigen modes, but a simple truncation at the noise floor is a proper approach.

To further refine the image reconstructed based on the distance between Gaussian function and subspace of the eigenvectors, I compare the variances of the eigenvectors obtained from the PCA of the observed images and the variances calculated from the reconstructed emitter distribution assuming emitters have independent but identical fluctuation statistics, and optimize the emitter distribution to make the two similar. I show that this refinement is able to improve the quality of reconstructed images from simulated data. However for experimental data I will include the details of the variance shaping in future works.

5.3 Results

5.3.1 Quantitative comparison of STORM and SCORE

The quality of single emitter localization based imaging method such as STORM/PALM is determined by many factors including emitter brightness, switching duty cycle and number of frames in an ideal drift-free case. The localization precision of a single emitter scales with the width the width of the point spread function (PSF) and inverse square root of the photons received by the camera. The on-off duty cycle of the emitters places an upper bound of the allowed emitter labeling density to achieve single emitter localization in a diffraction-limited area, which in turn defines the maximum spatial frequency of the resolvable feature according to the Nyquist criteria. However, the actual density of localized emitters in the reconstructed image is proportional to the number of frames and the emitter duty cycle. It has been shown experimentally that the limiting factor of the image reconstruction quality can be either localization precision or sampling density, depending on the choice of the specific fluorophore[37]. In conventional single-frame based image reconstruction algorithms, the two factors independently determine the limit. Harvesting more photons in one switch-on event does not increase the allowed emitter density, and for a fixed emitter brightness, accumulating more frames does not improve localization precision either.

In contrast, by making use of the pixel intensity covariance, SCORE breaks the limits of the emitter density upper bound. Regardless of the overlapping, a higher duty cycle means higher variance of each emitter brightness and higher signal-to-noise ratio in the covariance matrix. Accumulating more frames provides better statistics of the pixel covariance, thus also improves the ability to resolve smaller features. To show the effect of higher duty cycle and number of frames on SCORE, I quantitatively test the performance in the simulation as follows. The width of the PSF σ is set to

1 pixel, where the pixel size is in the range of 100 nm to 150 nm in realistic cases (figure 5.2(a)). I place 100 emitters at equal distances on a sub-diffraction-sized ellipse with long axis being σ and short axis 0.8σ (red oval in figure 5.2(a)). The averaged number of photons collected in one switch-on event depends on the specific fluorophore. Here I choose a typical value of an averaged 1000 photon per switch, following an exponential distribution to simulate the variability of photons emitted in each switching event. The switching follows a two-state model with $p_{off} = 0.9$ for switching from on-state to off-state in the next frame, and p_{on} varies to give different duty cycles (dc). A Gaussian white noise with standard deviation of 2 is added to the generated images to simulate image read out noise, which is typically below 1-2 photons on an EMCCD camera. A set of reconstructed images using STORM and SCORE are collected at a series of variable p_{on} from 0.0005 to 0.5, and total number of frames from 100 to 10000.

To quantitatively describe the quality of a reconstructed image, I interpret it as a probability density distribution of finding an emitter, and use KullbackLeibler (KL) divergence to describe the distance between ground truth and the images. The KL divergence is defined as

$$D_{KL}(P\|Q) = \sum_k P_k \ln(\frac{P_k}{Q_k}), \tag{5.5}$$

where P_k and Q_k are the intensity (probability distribution) of the true emitter positions and the resolved STORM or SCORE images respectively. Since the simulated emitters reside on a discrete set of points, I convolve the discrete distribution with a Gaussian function of the size of a up-sampled grid size x_k to avoid aliasing. The KL divergence for STORM and SCORE images are calculated and the median values of 20 to 40 repeats are shown in figure 5.2(b) and (c). Sample images at 300 frames and 2000 frames and various duty cycles are shown in figure 5.2(d), along with the

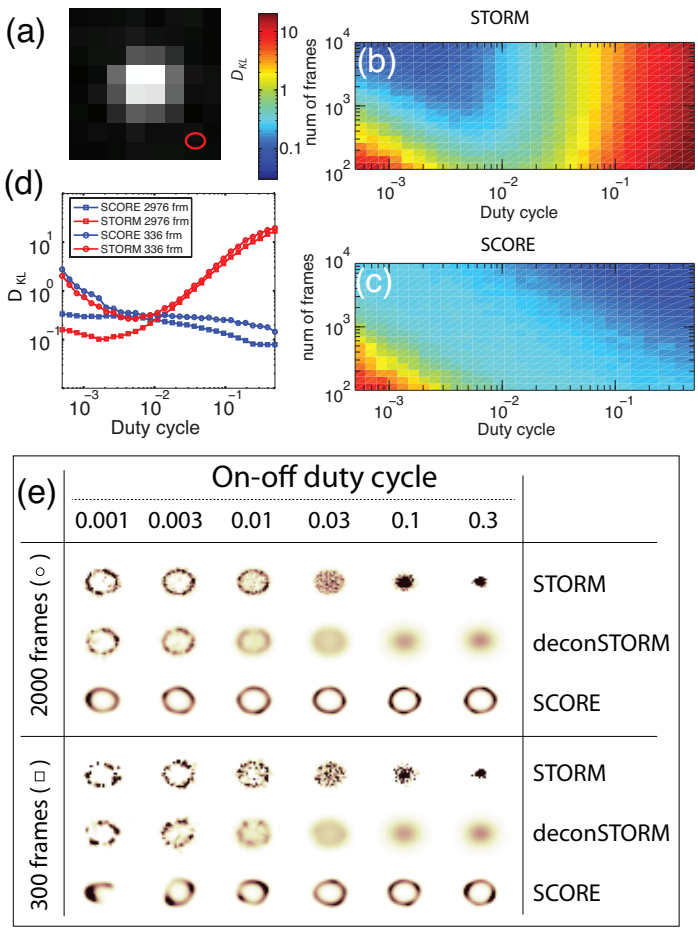

Figure 5.2: Comparisons of STORM and SCORE using a simulated emitters distributed on an ellipse. (a) A Typical image of an emitter giving 1000 photons, with an PSF width of 1 pixel. An in scale ellipse is shown at the bottom right. (b,c) The logarithm of KullbackLeibler (KL) divergence of reconstructed STORM (b) and SCORE (c) images with the ground truth distribution at various duty cycle and number of frames. (d) KL divergence of two methods at stack size of 336 and 1833 frames as a function of duty cycle. (e) Sample images of STORM, deconSTORM and SCORE at various duty cycle and stack size.

comparison with standard STORM method and deconSTORM. At high stack size and low duty cycle below the critical value of 0.01, both STORM and deconSTORM are able to reconstruct the ellipse at good accuracy, but SCORE has lower accuracy due to low emitter intensity variance at low duty cycle. One major artifact I observe is a systematically reduced radius of the oval, causing a large deviation from the true locations, even tough the hollow structure of the oval was correctly resolved. With variance shaping, the radius can be more accurately restored, and a lower KL

divergence better than STORM is achieved. Above the critical duty cycle, STORM quickly failed to resolve the hollow structure and collapse to a single point, and deconSTORM has a better tolerance to overlapping emitter but is still unable to resolve the ellipse if more than 10 emitters are switched on in average. One can decrease the labeling density to allow higher duty cycle, in which case the localized emitter density is limited by the number of frames, and the best quality image is always obtained near the critical labeling density/duty cycle. In contrast, SCORE consistently performs better at higher duty cycles, reaching a lower KL divergence than the optimal result of STORM. At a lower image stack size of 300 frames, STORM and deconSTORM behave qualitatively similarly to the previous 2000-frame stack size, except that the images are more discontinuous. However, SCORE is still able to perform reasonably well, resulting in a consistently smoother and more accurate result as the duty cycle increases to an optimal value of 0.1, which is much higher than the acceptable maxima of STORM and deconSTORM (figure 5.2(e)).

Another limiting factor of the reconstructed image quality is the localization precision of each emitter, determined by its brightness and the level of background noise[141]. In single emitter localization type of techniques, the uncertainty in determining emitter location effectively blurs the true emitter localization configuration, and this blurring effect can not be easily corrected by accumulating frames. To study the effect of localization precision on imaging quality, I increase the background noise in our simulation to a higher level of 15 photons on each pixel, and vary the signal-to-noise ratio by tuning the number of photons received from a switched-on emitter in a range of 100 to 3000 per frame. The KL divergence of STORM and SCORE images from the ground truth is calculated at their corresponding sub-optimal duty cycle of 0.002 for STORM and 0.05 for SCORE, and at various number of frames and emitter brightness as shown in figure 5.3(a) and (b). In the low SNR regime, the STORM image quality is limited by the photon shot noise and background noise, accumulat-

ing frames indeed has little effect decreasing the KL divergence (figure 5.3 (c)), and only increasing emitter brightness helps. Different from STORM, the KL divergence of SCORE images from the true distribution decreases as more frames are collected (figure 5.3 (c)), because the covariance of noise decreases as the inverse-square-root of the stack size whereas the covariance of the true signal is independent of the stack given that the flickering statistics remains stable. For fixed number of frames, a higher number of photons increases the SNR, thus improves the imaging quality of both STORM and SCORE, and the latter benefits more dramatically from brighter emission. This is because by allowing overlapping source images, SCORE effectively increases SNR at a fixed background noise level, thus outperforms STORM at high background noise conditions. I also observe that variance shaping further improves the image quality comparing with SCORE, in that it restored the radius of the ellipse more accurately.

5.3.2 SCORE images of fluorescently labeled Microtubule

As experimental demonstrations, I apply SCORE imaging on microtubule fluorescently labeled with either organic dye or quantum dots (QD) at short time scale of a few seconds and compare with STORM when applicable. Microtubule in fixed HeLa cells are stained with antibodies conjugated with Alexa Fluor 647 fluorescent dye, and imaged through epi-fluorescence microscopy because the microtubules are far from the glass-buffer interface. A 50 mW 643 nm diode was kept on during the entire image acquisition that gives around 10 kW/cm^2 excitation and switching-off light, and after the brief exposure of a few seconds under the red laser, the majority of the fluorophores are switched off. Then at the gaps between the camera exposure, I add a short laser pulse with 50 mW power at 405 nm wavelength to switch on Alexa Fluor 647 fluorophore to achieve higher duty cycle. A bright and nonuniform background signal degrades the image, but does not significantly impact the SCORE analysis

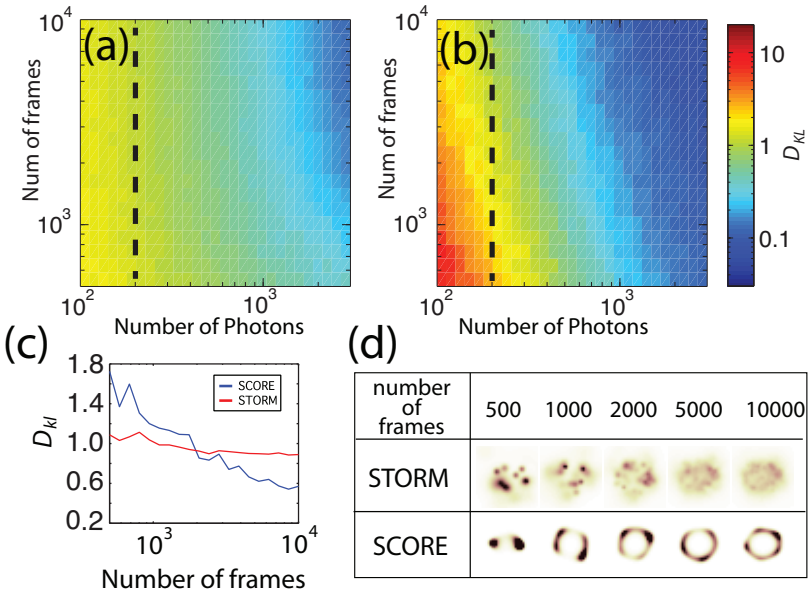

Figure 5.3: low photonComparison of STORM and SCORE at lower signal-to-noise ratio where the number of photons per switch-on is low and background noise is high. (a) The dependence of KL divergence of STORM images on the number of accumulated frames and photons per frame at high level of background noise ($\sigma = 15$). (b) Same test as (a) on SCORE. (c) A slice of KL divergence at 256 photons per frame, indicated as the dashed lines in (a) and (b). (d) Samples of reconstructed images from the two methods at 256 photons per frame and selected number for frames.

since covariance calculation only takes the variation into account. After the initial burst of the switching-on that last 3-5 seconds, the duty cycle relaxes to a low value under the 405 nm activation for minutes, when regular STORM image is suitable. The images are acquired at 100 frames per second to capture the fast dynamics of the fluorophore switching dynamics.

I analyzed the first 5 seconds of data using SCORE after the UV activation laser was turned on when the duty cycle of Alexa Fluor 647 was the highest, shown in figure 5.4(c) next to the epi-fluorescence image (a) and the variance (second-order SOFI) (b) of all 500 frames. Since the background intensity is high and nonuniform, the displayed mean is high-pass filtered for better illustration of the features with lower dynamic range than the background. The same set of 500 frames are also analyzed with standard STORM (figure 5.4(d)). From only 5 seconds of data, SCORE

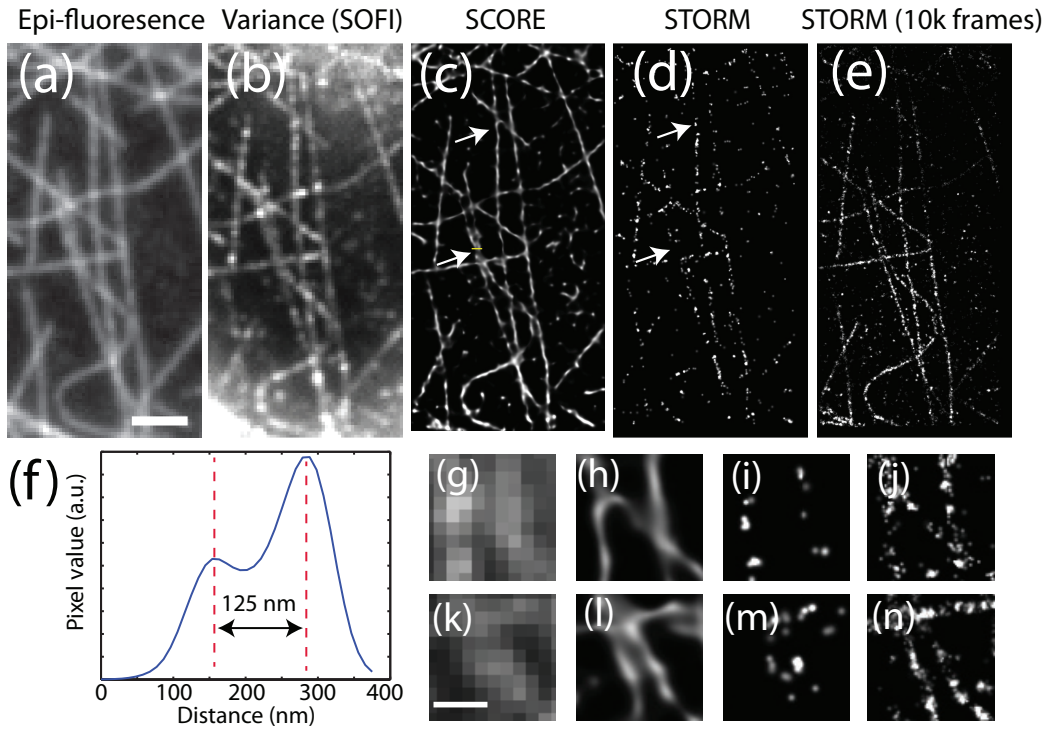

Figure 5.4: low photon Microtubule of Hela cells is labeled with Alexa Fluor 647 and analyzed with SCORE and STORM at various number of frames. (a) The epi-fluorescence image of the labeled microtubule before the dye is switched off. (b) The variance of 500 frames where the 405 nm laser activates high density of fluorophore with overlapping PSF. (c) and (d): SCORE and STORM analysis of the 500 frames. (e) STORM analysis of a total 10000 frames with low density of switched-on emitters. (f) Intensity profile of a line in SCORE image indicated by the arrow and yellow line in (c). (g)-(n) Two zoomed portion of the variance, SCORE, 500 frame STORM and 10000 frame STORM. Scale bars: (a-e) 2 μm, (g-n) 500 nm.

is already able to resolve sub-diffraction limited structure at sub-diffraction scale of 120 nm where our PSF width is 150 nm. In comparison, the high duty cycle and overlapping images of close emitters cause STORM to reject many activated emitters, resulting in a low density of resolved centers (figure 5.4(d,i,m)). The next 10000 frames have sufficiently low duty cycle and suitable for standard STORM analysis, with the result shown in figure 5.4(e). Higher number of resolved emitters provides a better representation of the labeled microtubule, although still discontinuous ((e,j,n)). Two selected regions indicated by the arrows in (c) and (d) are zoomed in as demonstrations in panel (g-n).

The performance of organic dyes suffers from photobleaching after several switching cycles, and the condition I performed our experiment was optimized for STORM imaging so that the flickering was not fully promoted. It has been reported that mixing both oxidant and reductant with dyes increases both switching-on and off rates[27], thus one can anticipate faster and more robust switching dynamics for better statistical analysis. Another type of fluorescent source that is bright and intrinsically fluctuate the emission intensity is quantum dot. Its variability in brightness is often considered as a negative factor in imaging applications, although this fluorescent intermittence is ideal for fluctuation statistics based super-resolution techniques as shown in recent works[87, 40] and for SCORE. I label microtubule in HeLa cells with antibody conjugated with QD655, use a 20 mW 532 nm wavelength laser as excitation light, and image at oblique illumination condition with a NA 1.46 objective at 135 frames per second to capture the fast intensity fluctuation of quantum dots (figure 5.5).

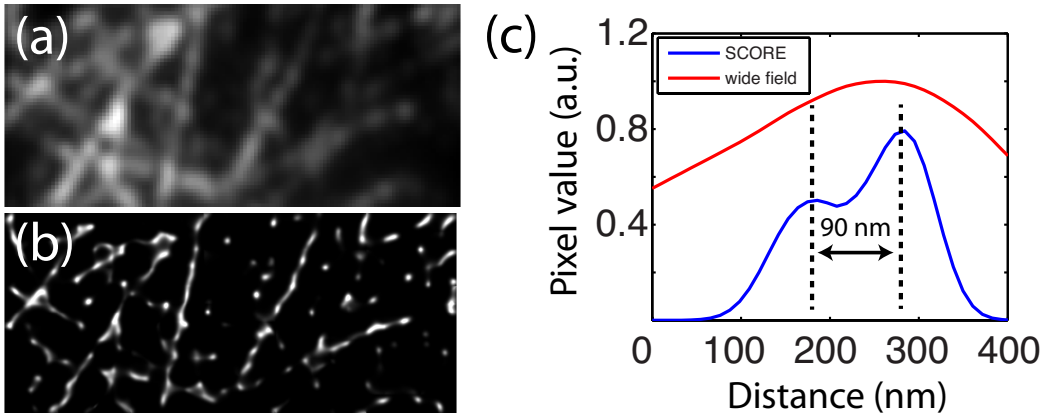

Figure 5.5: Quantum dot labeled microtubule in HeLa cells is imaged and analyzed with SCORE. (a) An averaged image of 1000 frames (7.4 seconds) of quantum dot labeled microtubule (cyan), overlaid with SCORE image of the same 1000 frames (red). (b) Intensity line profile of he labeled portion of the wide field image (indicated by the arrow in (a)) and SCORE image (blue line). Scale bar: 1 μm.

Quantum dots have much better resistance to photobleaching than organic dyes. The power-law distribution of the on and off time of quantum dots over a broad time

scale suggests that there is no typical time scale[126], thus I chose to image at a fast frame rate of 135 frames per second limited by the camera bandwidth, which still provided sufficiently fast dynamics and intensity variation for SCORE analysis. However, compared to Alexa Fluor 647 labeled microtubule, quantum dot labeling is more nonuniform and discontinuous along the microtubule (figure 5.5(a)) presumably due to the larger size and the quality of our sample. Figure 5.5(a) shows an overlay of the SCORE image (red) and the average (cyan) for comparison. SCORE image clearly shows the breaks between labeled segments (figure 5.5(b)), and is able to resolve fine structures near the junctions of two microtubules at 90 nm spatial resolution (figure 5.5(b)).

5.4 Discussion

Super-resolution imaging has become available on a conventional epi-fluorescence microscope with little to no modification to the optical design. The fine structural information embedded in a sequence of images can be restored in two groups of methods: single particle localization method as in STORM and PALM, and intensity fluctuation statistical approaches as in SOFI, ICA and SCORE. STORM/PALM and their variant localization methods have becoming increasingly popular due to the outstanding resolution. The quality of the reconstructed images are limited by essentially two factors: the localization precision determined by the emitter brightness and background noise, and sampling density that is set by the fluorophore duty cycle, labeling density and acquisition time. Either factor can be the bottleneck of the final image quality, and improving the other has little effect. Moreover, STORM/PALM typically requires thousands or more images for dense enough sampling due to the non-overlapping condition, and thus greatly limits the use in capturing dynamics faster than minute scale. By looking at the covariances between the intensities of

pixels statistically, SCORE is no longer limited by the non-overlapping condition, and is able to reconstruct images with comparable quality from less frames that contain denser information. In addition, any improvements in emitter brightness and its variation, number of frames, higher labeling density, and lowered background noise all contribute to better statistics, therefore the imaging quality is no longer limited by one single bottleneck. In particular, a higher labeling density is preferably chosen for SCORE instead of carefully limited in STORM. However, in the case of low emitter density where emitters are known to separate well, single particle localization methods make use of this information that the statistical methods ignores, and are able to resolve the locations at much better accuracy at the cost of substantially higher acquisition time.

SCORE is closely related, but different from the other two methods that resolves emitter distribution from intensity fluctuation, SOFI[39, 40] and ICA method[87]. All three methods share the common advantages of analyzing intensity statistics over single particle localization methods discussed above. SOFI and its later improvement XC-SOFI primarily takes the temporal fluctuation of individual pixels into account. The spatial correlation (cross cumulant) information is used to interpolate estimation between pixels to achieve finer resolution. SCORE considers the covariance between all pairs of pixels to estimate the distribution of emitters, and by sorting and truncating the eigen modes, SCORE efficiently resolves the distribution in the linear subspace that contains the majority of the information contained in the original image stack in a much higher dimensional space. Also from the eigen modes obtained from the principle component analysis (PCA), Lidke *et al* resolved the localization of finite number of quantum dots from the temporal sequence of the eigen modes using independent component analysis (ICA), however the ability to resolve individual emitters quickly becomes intractable if more than several emitters are packed in one PSF area. Instead of attempting to resolve individual emitters with their specific temporal blinking se-

quence, I use the distance between the eigen modes and Gaussian functions, and our method is capable of estimating continuous distribution rather than finite discrete point distribution.

Because the covariance matrix does not depend on the basal intensity at each pixel, SCORE will reject any temporally non-drifting background, such as nonspecific autofluorescence signal. This property allows SCORE to analyze images with only a portion of emitters switching while the rest remains on. Since the fluorescence intermittence takes place at much faster time scale than the photobleaching, it is applicable to temporally high-pass filter the intensity sequence at each pixel before processing to remove the slowly varying background signal. The out of focus light can also be treated as background light since the intensity correlation of defocused light is delocalized and spatially convolved into more uniform signals in time, thus contribute less to the covariance.

Many different types of fluorescent sources undergoes intensity fluctuations at fast time scale, thus serve as possible candidates for SCORE as well as SOFI. In this thesis, I used organic dye and quantum dots as demonstrations for SCORE imaging. Organic dye can switch between activated and dark states in proper chemical environment, but relatively small number of switching cycles before bleaching limits the SCORE image quality. For quantum dots, the high brightness, robust fluorescence intermittence and resistance to photobleaching are the major advantages as fluorescent sources. However, the slightly larger size and toxicity are the limiting factors for using it as probes in live systems. In the past decade, a library of fluorescent proteins are also reported to have stochastic or controllable intensity fluctuation or switchablility in emission spectra at fast time scales, such as mTFP0.7[63], Dronpa[3], rsCherry[134], IrisFP[1], rsTagRFP[137]. Dedecker *et al* have applied intensity-fluctuation based super-resolution technique SOFI to imaging structures labeled with Dronpa labeled Lyn kinase[36] and resolved structure at 100-200 nm spatial scale. Their work sug-

gested the possibility to use fluorescent protein in statistical super-resolution methods including SCORE.

Covariance calculation can be extended to three-dimensional imaging, where images at various focal depths are collected simultaneously. In this case, photons from the a bright emitter are distributed on multiple fields focusing at different axial depths simultaneously, and the covariances between pixels generate a set of three-dimensional eigen modes. Following exactly the same principle, the emitter distribution in 3D can be estimated by measuring the distance from the PSF in 3D to the subset of the eigen modes. The inhomogeneity of the 3D PSF in the axial direction is critical for the axial resolution. The double-elliptical[69] and double-helix PSF[109, 110] are both potential candidates for SCORE application in 3D.

5.5 Materials and Methods

5.5.1 Cell Culture and Immunostaining

Human HeLa cells were cultured as described in [92]. Cells were fixed in formaldehyde followed by permeablization[92]. Fixed cells were washed in PBS 3 times, incubated with mouse anti-tubulin (Sigma-Alderich) 24 hours at 4°C, then washed with PBS 3 times and incubated with 20 nM anti-mouse IgG fused with Alexa Fluor 647 (Life Technology) in PBS and 6% w/v BSA for 30 minutes. Stained cells were washed in PBS and replaced with imaging buffer containing 50 mM Tris at pH 8.0, 10 mM NaCl, 10% glucose w/v, 5 mg/ml glucose oxidase, 100 ug/ml catalase and 100 mM βme [37]. All chemicals were purchased from Sigma-Alderich unless noted otherwise.

Quantum labeled cells were prepared and treated in the same way described above. Cells incubated with primary antibody were washed with PBS 3 times, and incubated with 20 nM anti-mouse IgG fused with QDot 655 (Life Technology) in PBS and 6%

w/v BSA for 30 minutes. Stained cells were washed in PBS and directly mounted to the microscope for imaging.

5.5.2 Microscopy and Imaging

Microtubule *in vivo* images were taken on a home-built microscope with Olympus NA 1.4 objective. A 50 mW 643 nm laser was used as the excitation and deactivation source, and 50 mW 405 diode laser was used as the activation laser. Both lasers were sent to the objective with a multi-band dichroic mirror, and the a multi-band emission filter was used to clean the emission. Images were collected using an EMCCD camera (Andor).

Quantum dot labeled microtubule images were taken on a Nikon TE-2000 inverted microscope. A home-built 20 mW 532 nm diode laser was used as the excitation source, and a dichroic mirror (FF560, Semrock) and long-pass filter (XF3089, Omega) were used as the beam-splitter and the emission filter. The images were collected with an EMCCD camera (iXon+ 897E, Andor Technology).

5.5.3 Image Analysis

For SCORE analysis, image stacks of Alexa Fluor 647 labeled microtubule were assumed to have a fixed background with a decaying intensity. The decaying background was subtracted from the raw images before SCORE analysis. The image field is divided into overlapping regions of interest with size of 8×8 pixels, and the processed ROIs are stitched with pyramidal weight masks (2D equivalent of triangle window function in 1D). Quantum dot images do not have observable photobleaching, thus background correction is not necessary. The entire image was divided into 10×10 ROIs and stitched in the same way described above.

STORM images in the simulations are reconstructed from the Gaussian fit of the individual frames, since all emitters are located with 1 PSF width, no sepa-

rate or Gaussian mixture fit is necessary. I discarded all frames that contains less than 300 photons prior to Gaussian fit. The STORM images were rendered from the localization results, and each detected emitter is displayed as a Gaussian whose width scales with the inverse square root of the emitter intensity as described in [37]. Images of Alexa dye was first processed using QuickPalm plug-in of ImageJ to obtain the center and width information, which are used to render the STORM image as described above. All simulations, Gaussian fit in STORM simulations, and STORM image rendering and SCORE analysis were performed in MATLAB (The-MathWorks,Natick,MA).

Chapter 6

Developing Tracking Algorithm for Mutually Exclusive Objects

6.1 Introduction

A broad range of biological problems on many length scales, from cells to whole animals, require the ability to track moving individuals with a group. Advances in computer vision in the past two decades had enabled computed-aided automatic or semi-automatic tracking programs to greatly boost the capacity to analyze large amount of data and reduce the involvement of human observers. However, many traditional tracking algorithms struggle when the objects come into physical contact or even overlap within an image. Recent work addressed this problem by separating objects using a Gaussian mixture model with an area prior followed by identity matching and successfully applied this approach to track walking *Drosophila* with minimal human supervision [20]. Tsai and Huang further extended this approach by refining the segmentation of the *Drosophila* images into different body parts which enables more detailed measurements to be made [147]. A non-Bayesian frame work was used by Chaumont et al. to track multiple mice by modeling the animal body

with a series of physical "primitives" connected by joints and elastic springs that can interact with each other [33]. All of these algorithms are capable of handling large amounts of images, $> 10^4$ frames, with relatively little tracking error that is then corrected manually. However, this error rate increases with reduced image quality or when the objects move close to one another more frequently.

In most tracking solutions, image segmentation is performed on each frame to identify individual objects. This is then followed by an identity matching scheme between frames based on distance, object birth and death probabilities and other estimated parameters [72, 20]. Active contours (snakes) are a popular image segmentation approach that is widely applied in analyzing biological and medical images. The contour of the compartment boundary is treated as an elastic band that interacts with the image and exhibits a damped relaxation to the minimum energy state [75]. In addition to closed-contour uses for measuring parameters like object area, open active contours can be used to detect filamentous objects such single actin filaments [86] and actin networks [164]. In these approaches, active snakes can be allowed to merge, break, fork and recombine.

In this work, we solve the tracking problem using a deformable membrane model which is an extension of the active contour model to higher dimensions. In order to prevent merging of multiple objects, we added a repulsive interaction between neighboring contours. I test this method on two practical examples from neuroscience and microbial ecology: walking *Drosophila* and gliding bacteria *Myxococcus xanthus* are tracked at high density with low error rate (¡ 5×10^{-6} per fly per second, or 10^{-5} per cell per second), and at high efficiency (better than 50 frames per second when tracking 5 flies). Finally, we discuss the close connection between Bayesian techniques the energy minimization approach.

6.2 Repulsive open active contour model

6.2.1 The classical active contour model

In the classical active contour model, a feature in an image, usually a line, boundary or edge, is found by relaxing an elastic contour that interacts with the image to its minimum energy state. The energy of the snake consists of the internal elastic energy of the contour and the image energy based on the location of the contour in the image E_{im}, calculated along the contour $\mathbf{x}(s)$, in N dimensional space

$$E = \int_A^B \left(\frac{1}{2} \left(\alpha |\mathbf{x}'(s)|^2 + \beta |\mathbf{x}''(s)|^2 \right) + E_{im}(\mathbf{x}) \right) ds, \tag{6.1}$$

where α penalizes the energy when the contour is deviated from a uniform straight line and β adds an additional cost to bending. A and B are the termini of an open contour, which we define as 0 and 1, or in case of a closed contour, the integral path is closed. Minimizing E is equivalent to solving

$$\alpha \mathbf{x}'' - \beta \mathbf{x}'''' - \nabla_{\mathbf{x}} E_{im}(\mathbf{x}) = 0. \tag{6.2}$$

Equation 6.2 can be written discretely as

$$A^* x_i + \frac{\partial E_{im}}{\partial x_i} = 0, \quad i = 1, 2, ..., N, \tag{6.3}$$

where each x_i is an M-element vector that defines the contour using M discrete points that are equally spaced along s. A^* is the $M \times M$ circular pentadiagonal discrete

equivalent of the operator $-\alpha d^2/ds^2 + \beta d^4/ds^4$

$$A^* = \begin{pmatrix} a_0+b_0 & a_1+b_1 & b_2 & 0 & ... & 0 & b_2 & a_1+b_1 \\ a_1+b_1 & a_0+b_0 & a_1+b_1 & b_2 & 0 & ... & 0 & b_2 \\ b_2 & a_1+b_1 & a_0+b_0 & a_1+b_1 & b_2 & 0 & ... & 0 \\ & & & ... & ... & & & \\ 0 & ... & 0 & b_2 & a_1+b_1 & a_0+b_0 & a_1+b_1 & b_2 \\ b_2 & 0 & ... & 0 & b_2 & a_1+b_1 & a_0+b_0 & a_1+b_1 \\ a_1+b_1 & b_2 & 0 & ... & 0 & b_2 & a_1+b_1 & a_0+b_0 \end{pmatrix}, \tag{6.4}$$

with $a_0 = 2\alpha$, $a_1 = -\alpha$, $b_0 = 6\beta$, $b_1 = -4\beta$, $b_2 = \beta$. Equation 6.3 can then be solved iteratively via

$$x_i^\tau = (A^* + \gamma I)^{-1} \left(\gamma x_i^{\tau-1} - \nabla_i E_{im}(x_i^{\tau-1}) \right), \tag{6.5}$$

where τ is the iteration index, γ sets the time step, and ∇_i denies the spatial derivatives $\partial/\partial x_i$. Additional forces can be conveniently incorporated into the model by adding a force term F_i

$$x_i^\tau = (A^* + \gamma I)^{-1} \left(\gamma x_i^{\tau-1} - \nabla_i E_{im}(x_i^{\tau-1}) + F_i \right), \tag{6.6}$$

Numerous variations of this active contour model have been developed for specific image-analysis and tracking problems, including the use of variable stretching and bending stiffnesses α and β, sophisticated image potentials E_{im}, and the inclusion of additional forces for specific purposes. Here, we aim to solve the multiple object tracking problem in time-lapsed movies.

6.2.2 Open contours

While a circular pentadiagonal matrix A^* is suitable for dealing with a closed contour, for open contours, the motion of the two tips needs to be considered separately. I modify the first and last two rows of A^* such that the internal force acting on the tips is equal to half of the internal force on the nearest neighbor, but in the opposite direction

$$A = \begin{pmatrix} -a_1/2 & -a_0/2 & -a_1/2 & 0 & ... & 0 \\ a_1 & a_0 & a_1 & 0 & ... & 0 \\ & & ... & ... & & \\ 0 & ... & 0 & a_1 & a_0 & a_1 \\ 0 & ... & 0 & -a_1/2 & -a_0/2 & -a_1/2 \end{pmatrix}. \tag{6.7}$$

I also set $\beta = 0$ in all the open-contour examples because penalizing the contour length adds an effective energetic cost to path curvature. I find that a non-zero value for beta does not qualitatively change the behavior of the open contours analyses.

Without an additional constraint, the tips are left free to interact with the image. Tip forces can be added to elongate or shorten the contour in order to control the contour length. In many multiple object time-lapse tracking problems, the characteristic spatial scale of the underlying objects is known and does not change, even though the objects can change position, orientation, and twist over time. In this work, we fix the length of the contours by adding a harmonic tip-stretching force, F_{str}, based on the length of the contour, l_0,

$$F_{str} = -\kappa(l - l_0)\hat{\rho}, \tag{6.8}$$

where $\hat{\rho}$ is the tangential direction of the contour at the tip pointing outwards,

$$\hat{\rho} = \begin{cases} -\frac{d\mathbf{x}/ds}{|d\mathbf{x}/ds|} & : s = 0 \\ \frac{d\mathbf{x}/ds}{|d\mathbf{x}/ds|} & : s = 1 \\ 0 & : \text{otherwise} \end{cases}, \tag{6.9}$$

l is the length of the contour, $l = \int_0^1 |d\mathbf{x}/ds|\, ds$, and κ governs the relative magnitude of the stretching force.

6.2.3 Track contour motion over time

The kymograph of a contour that moves in N-dimensional space over time is a continuous surface in $N + 1$ dimensions. In certain types of problems where the objects undergo Brownian motion, a global optimization strategy such as the framework to solve the linear assignment problem (LAP) is usually necessary. However, in many other cases where the trajectories are smooth, local optimization is sufficient and more efficient. Here we apply the concept of active contours to the temporal dimension as well as the spatial dimension within each frame, and optimize the localization of the two-dimensional active membrane in the $N + 1$-dimensional kymograph. Different from freely moving contours in all spatial dimensions, the object has one unique location at each time point, and no localization information is carried at times between frames. For these reasons, we require the control points of the active surface to move within each time slice but do not allow along the temporal axis. For active surface, x_{it} is a $M \times T$ matrix that determines the location of the contour at all time, where M is the number of control points along the contour, and T is the number of frames. I seek the solution of

$$Ax_{it} + x_{it}B^T + \frac{\partial E_{im}}{\partial x_{it}} - F_{it} = 0, \quad i = 1, 2, ..., N, \quad t = 1, 2, ..., T, \tag{6.10}$$

where $T \times T$ pentadiagonal matrix B that calculates the derivatives in time has the same structure as A. This equation can also be solved iteratively as

$$(A + \gamma I)x_{it}^{\tau} + x_{it}^{\tau} B^T + \nabla_i E_{im}(x_{it}^{\tau-1}) - \gamma x_{it}^{\tau-1} - F_{it} = 0, \tag{6.11}$$

which is in the form of a Sylvester equation.

In practice, instead of optimizing the active surface on all frames, we slice the kymograph into overlapping blocks in the temporal dimension and sequentially obtain the optimized short localization segments in accordance with the results from previous blocks in time. When the temporal projection of the kymograph of one or multiple objects has overlaps, incorrect initial condition will cause slow convergence or trap the solution at local minimums where the registration of traces to image potential minima is swapped. By solving the problem in a block-wise manner, we avoid incorrect initial placement of the contours and greatly reduce the computation time using the local initial guess based on previous results.

6.2.4 Repulsion between multiple contours

Active contour and surface models can be applied to an image or time-lapse movie of multiple objects by starting at different initial locations. However, when the objects are in close proximity to one another, the barrier that separates the two objects in the image energy landscape can diminish below a significant level due to noise and other image-based effects (Fig. 6.1). As a result, two contours or surfaces with different initial locations can converge to the same image energy minima. To avoid this collapse, we optimize the energy of multiple snakes simultaneously with the addition of a mutual repulsive force between the contours or surfaces. Because the repulsive force resembles physical exclusion, we limit the range of this force to the approximate

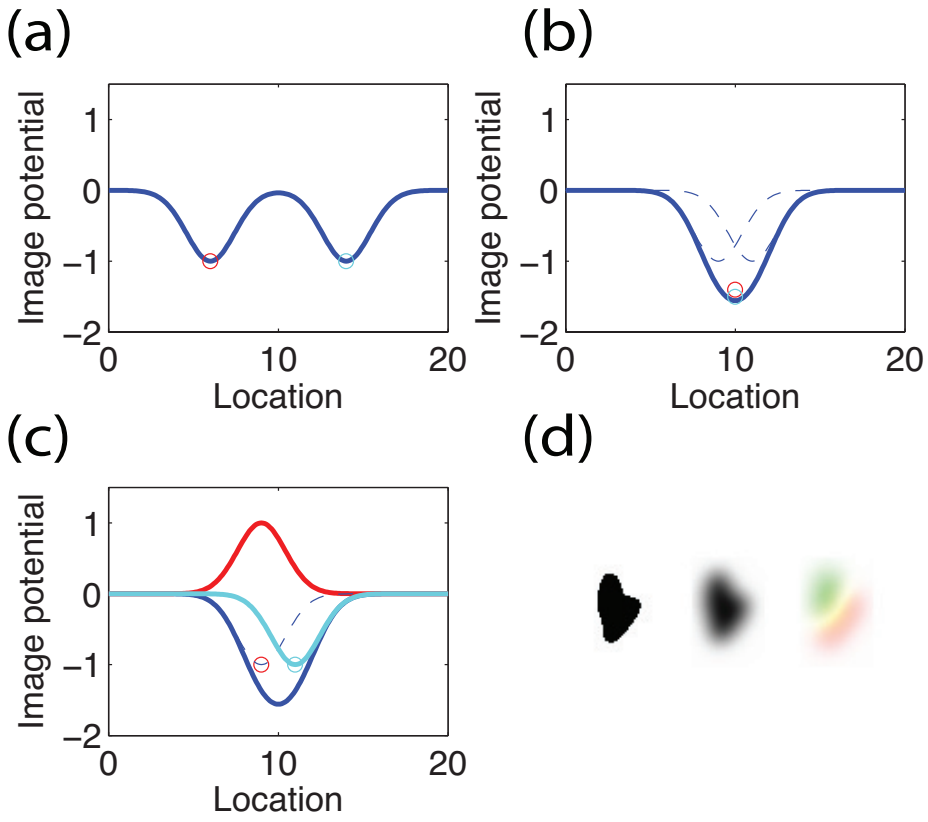

Figure 6.1: Schematic illustration of the principle of the repelling active contour. (a) While objects are far away and the attractive image potential fields (blue solid line) don't interact, two active objects (red and cyan circles) fall to the minimum image energy correctly. (b) When objects get close, the potential fields (blue dashed lines) overlap and causes dislocation of the minima, or merged minimum. Two active objects fall into the same minimum. (c) With the repulsive potential added (red solid line), the total field the other object is in is recovered (cyan solid line). (d) This same principle can be easily applied to two and higher dimensions as shown.

size of the objects being tracked, and set the force magnitude to match the depth of the typical image energy minima.

In our model, we choose the force to have a quadratic form with the cutoff distance x_0, the same as the typical width of an object:

$$F_{lm}^{repel}(s_l) = \int_0^1 \left[1 - \frac{|\mathbf{x}_l(s_l) - \mathbf{x}_m(s_m)|}{x_0}\right] \frac{\mathbf{x}_l(s_l) - \mathbf{x}_m(s_m)}{x_0} ds_m, \tag{6.12}$$

where $F_{lm}^{repel}(s_l)$ is the unit arc length density of the repulsive force acted on the l^{th} contour due to the presence of the m^{th} contour. A discretized version of Eq. 6.12 takes the form

$$F_{it;lm}^{repel} = \sum_{j=1}^{N} \left[1 - \frac{|\mathbf{x}_{it;l} - \mathbf{x}_{jt;m}|}{x_0} \right] \frac{\mathbf{x}_{it;l} - \mathbf{x}_{jt;m}}{x_0}, \tag{6.13}$$

where $\mathbf{x}_{it;l}$ is the coordinate of the i^{th} control point of the l^{th} contour at the t^{th} frame. Here, the repulsive force is not normalized by to the actual length of the contour, but this is not a significant problem if all contours have similar lengths. A cubic potential is a sufficiently close approximation to the overall shape of the attractive potential generated by Gaussian smoothing of the original image.

6.3 Implimentation to object tracking problems

6.3.1 *Drosophila* walking behavior

I first demonstrate the repulsive, active membrane model on movies of walking fruit flies. *Drosophila melanogaster* has become a popular model system for studying complex behaviors such as courtship, aggression, and learning through the analysis of time-lapse movies of fly position. In these experiments, individual flies often come physically close to each other causing their images to merge. The repulsive-snake model is particularly adept at resolving the position of flies during these events.

I recorded a 30-Hz movie of five male flies walking in a circular, 2.5-cm diameter, arena, a density of 1 fly/cm^2. Camera magnification was set such that a fly subtends a 7-by-15 pixel area in the image. Our tracking algorithm models each fly as an open contour, length 12 pixels, with 3 control points (Fig. 6.2). Our tracker is able to follow five flies correctly in all 20,203 frames (a total time of 673 seconds). An oval shaped image potential constraints the orientation of the open snakes, so that body direction is correctly resolved. Occasionally, a fly exhibits an escape behavior

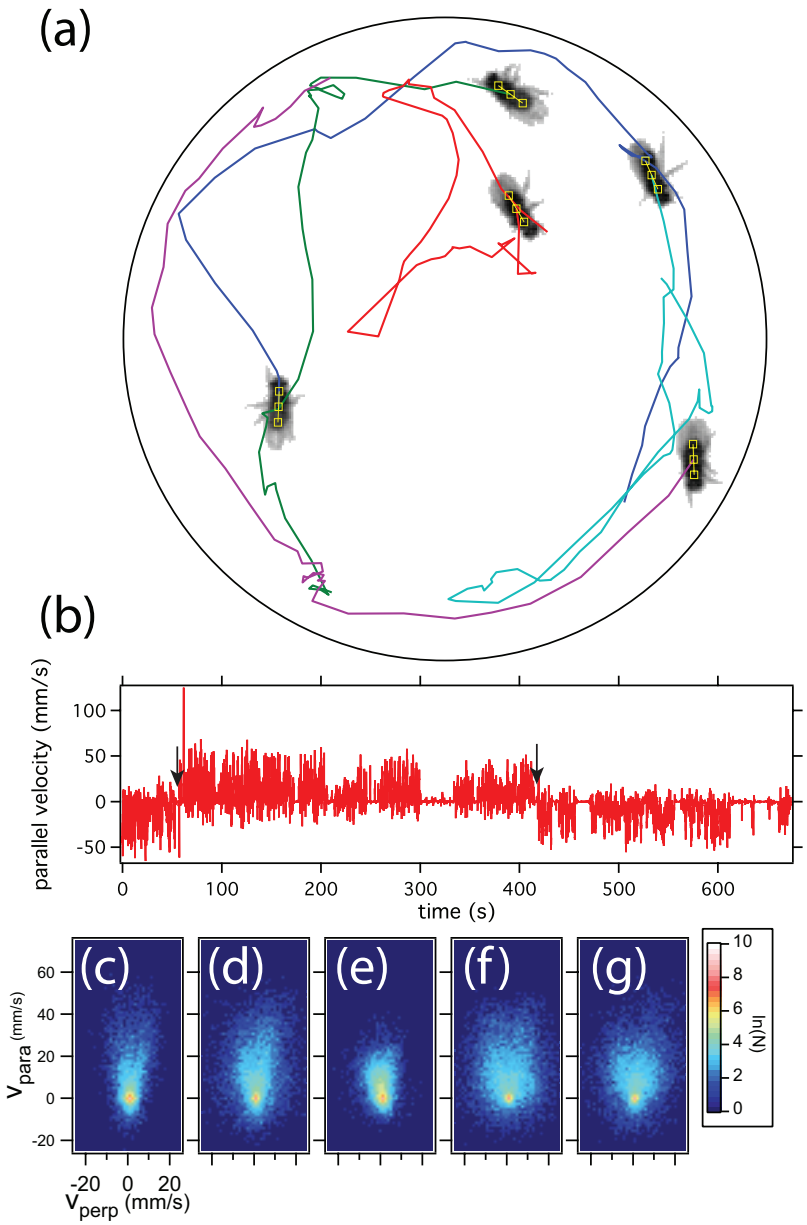

Figure 6.2: The velocity exacted from the tracking results of five male flies. The velocity is decomposed to the parallel and perpendicular components according to the direction of the fly pointing direction. (a) A sample image of five flies in the circular arena. The historical trajectories of the flies are labeled in different colors. (b) The raw parallel component is plot as a function of time. When fly jumps (indicated by arrows), the tracker may reverse the orientation and negate the velocity. (c-g) Velocity histograms of five individual flies. The color indicates the logarithm of the counts in each bin.

that causes a quick change in location and head direction. Because our algorithm does not currently consider image details other than the second-spatial moment, we do not attempt to distinguish head from tail although this is possible using purely image-based metrics in certain circumstances. Consequently, jumps may reverse the head-tail orientation (Fig. 6.2b). However, because flies mostly move forward, in the direction of the head, and the jumping frequency is small, on the order of 0.1 min^{-1}, a Hidden Markov method is suitable for the detection of jumps. I use this information and adopt the Viterbi algorithm to determine the forward-backward head direction as the last step of our fly tracking software [28]. Figure 6.2 (c-g) shows the 2D, log-probability distribution function of walking velocity for each of the five flies.

To increase the number of fly-fly encounters and test the ability of the repulsive algorithm to distinguish individuals, we placed one female and two male flies in the arena. Both male flies spend a large amount of time attempting to court the female fly, resulting in frequent merging of the fly images. 85% of the time at least one of the male flies is within 6 mm of the female fly and 31% of time both male flies are with this distance (Fig. 6.3a). Images are analyzed with our tracking algorithm with 100% correct registration of flies and only one orientation reversal caused by a jumping event (Fig. 6.3b). I calculated the position of a fly relative to another for all pairs of flies. Similar to previous analyses [20], we find that male flies tend to approach the female fly from the ear (Fig. 6.3 c, d), while maintaining a head direction oriented towards the female (Fig. 6.3 e, g). I compared the performance of our algorithm to the output of the CTRAX fly tracker [20] using the 5-male assay, the one female, two male (1F2M) assay, and a high density movie with 16 flies in a 5 cm^2 arena (Table 6.1). At high densities, flies frequently come in contact with each other and jumping is more frequent. Because CTRAX allows the number of objects to vary, it has three types of tracking error: identity swap, lost and spurious detection. In our repulsive contour model, where the number of flies is fixed, identity

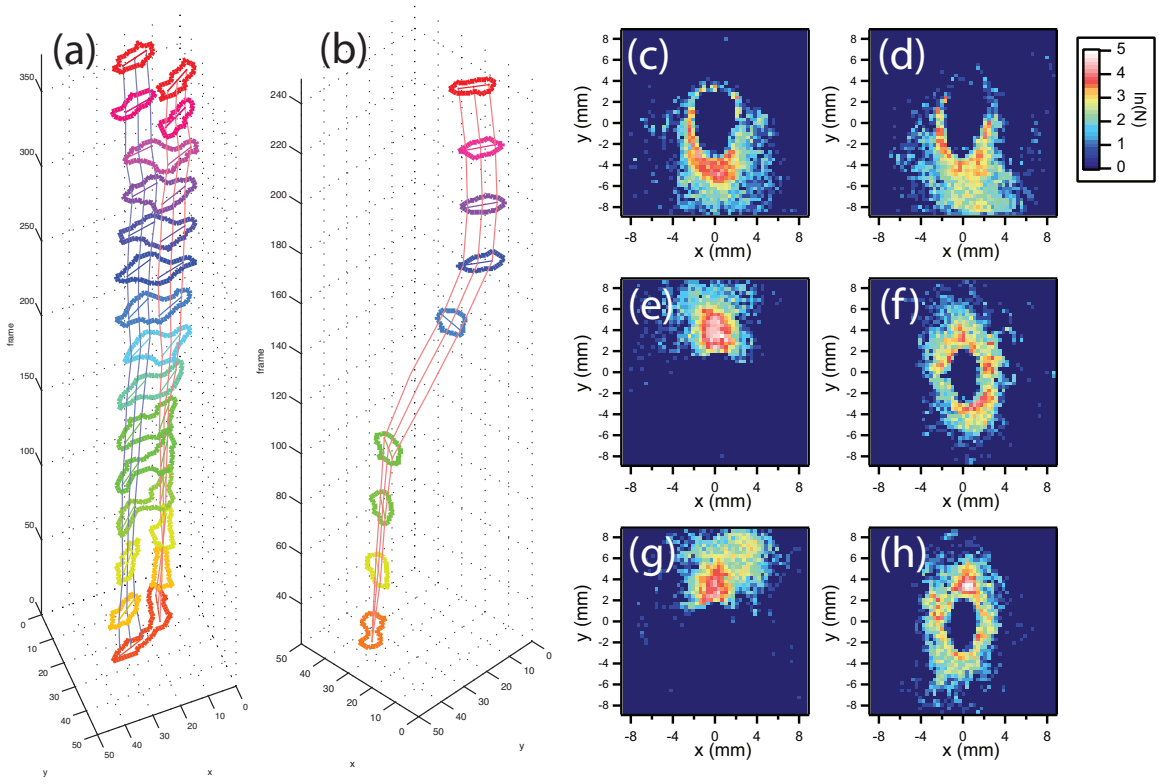

Figure 6.3: Tracking results of touching and jumping *Drosophila* are shown in the three dimensional kymograph, where the contours of the binary fly mask are indicated in false color according to time. The positions of the objects are shown in the same color and connected by lines as visual aid. (a) Two flies move in proximity of each other and then apart, causing the mask and contours to merge and split again. (b) A missing frame is caused by the a fly jumping event, followed by re-orientation. (c) -(h) The distribution of the relative position between two flies is shown as the logarithm of the count. The displacement is measured relative to the first fly on the perpendicular (x) direction and parallel (y) or the head direction.

Assay	Length of Movie (frames)	Fly-fly contacts	**CTRAX**		**Repulsive Contours**	
			Error	Speed (fps)	Error	Speed (fps)
5 males	20203	1427	0	4.4	0	40
1F2M	9000	12956	25	3.5	0	70
16 flies	4581	8717	9	3.1	3	10

Table 6.1: Comparison between CTRAX and the repulsive snake model. For all three movies tested, the number of fly pairs that have a distance closer than twice the fly width is counted as a fly-fly contact. In speed comparisons, both trackers were run on a single CPU core.

swap is the only kind of error. In addition, we compare the speed of the two tracking packages when run on an Intel i5 processor.

In the 5-male movie, where flies rarely come in close proximity to each other (3% of the time), both trackers are able to track all the flies without error. At higher fly density however, 3 flies cm^{-2}, both trackers are still able to distinguish individual flies although CTRAX has a small portion of spurious detections and fly jumping becomes the primary source of identity swap error. When the images flies constantly stay in close proximity, our model is still able to locate the flies from the boundary contour, but CTRAX suffers from overlapping detections. Moreover, we observe that the tracking quality of CTRAX is crucially sensitive to value of user-defined input parameters such as the image threshold and the Gaussian oval shape prior that requires multiple trials to optimize. In comparison, the repulsive snake model only requires the knowledge of the spatial scale, either the fly length or width, and the number of flies. The repulsive snake tracker is also 3-20 times faster than CTRAX.

6.3.2 *Myxococcus xanthus* gliding motility

Top highlight the ability of the repulsive contour technique to track densely packed objects, we analyzed movies of 2D swarms of *Myxococcus xanthus* cells. *Myxococcus xanthus* is a soil bacterium that forms complex, 3D group structures by gliding along solid surfaces (ref a review of myxo!). We immobilized *Myxococcus xanthus* cells

between an agarose gel and a glass surface such that cells form a single layer at the interface. Using bright field microscopy, the bacterial cell body appears dark and is surrounded by a bright halo. Cells are often tightly packed and the image contrast between the neighboring cells is poor.

I preprocessed the raw microscopy images before calculating the image-based potential for contour relaxation. I first calculated the eigenvalues and eigenvectors of the Hessian of the images to quantify features such as valleys (the cell bodies) and ridges (the cell halos). Because the background of the image is uniform, the two eigenvalues of the Hessian are linearly correlated with the pixel value. Hence, the first two principle components of the two eigenvalues and the image intensity are used to quantify image features. Qualitatively, the pixels are distributed in two clusters within this two-dimensional projection, with valley pixels residing in one cluster and the ridge pixels in the other. All background pixels lie within the small region between the clusters. In areas of high cell density and low image contrast, the projected distribution of individual pixels is similar to the background, however the alignment of the Hessian eigenvectors is more locally ordered than the background. The correlation length of the cell alignment typically extends to a few cell widths. Analogous to the quantification of the order in magnetization, each pixel carries an effective dipole that points along the direction of lager eigenvalue with an magnitude defined as the difference of the two eigenvalues, and the locally averaged dipole moment is the order parameter that describes how well nearby features are aligned. The alignment order parameter, together with the two principle components of the eigenvalue-image intensity space, forms a three-dimensional space in which the valley, ridge and background pixels are clearly separated. The orientation of the three sets is determined using an expectation-maximization algorithm and the pixels are simply clustered into three types by the coordinates along the major direction of each set of pixels (Fig. 6.4). I undersegment the valley and the background to prevent areas of too-high im-

age potential as the repulsive contour model is robust against undersegmented ridges but prone to errors caused by oversegmented valleys. The enhanced image used to calculate the image potential is computed using

$$I = p_b + 0.5p_r, \tag{6.14}$$

with

$$p_b + p_r + p_v = 1, \tag{6.15}$$

where p_b is the probability of a pixel being the background, p_r being the ridge, and p_v being the valley. I is Gaussian blurred with $\sigma = 1.5$ pixels before taking the gradient to give a smooth image force field (Fig. 6.4d).

Snakes of 25 control points are evolved in an image gradient calculated from the preprocessed images (Fig. 6.4d). The repulsive force between control points on nearby cells is taken to be a quadratic function of the distance

$$F_{rep} = \begin{cases} (1 - \|\mathbf{x}_{it}\|/d_0)\hat{\mathbf{x}}_{ij} & : |\mathbf{x}_{it}\| < d_0 \\ 0 & : |\mathbf{x}_{it}\| \geq d_0 \end{cases}, \tag{6.16}$$

where $\mathbf{x}_i j$ is the distance vector between two control points on two different contours and $\hat{\mathbf{x}}_{ij}$ is the unit direction vector. d_0 is a cut-off distance that sets the length scale of the repulsive force. I set d_0 to be 70% of the averaged cell width, about 7 pixels.

To prevent contours from starting the relaxation procedure at an initial position that crosses a ridge in the image (Fig. 6.5), we reduce the initial length of each contour to eliminate possible crossings, and let the lengths of the snakes grow back to their normal length during relaxation. This growth is implemented by adjusting the targeted snake length l_0 in equation 6.8 during each iteration by an amount

$$\Delta l_0^\tau = \tanh(l_0 - l^{\tau-1}), \tag{6.17}$$

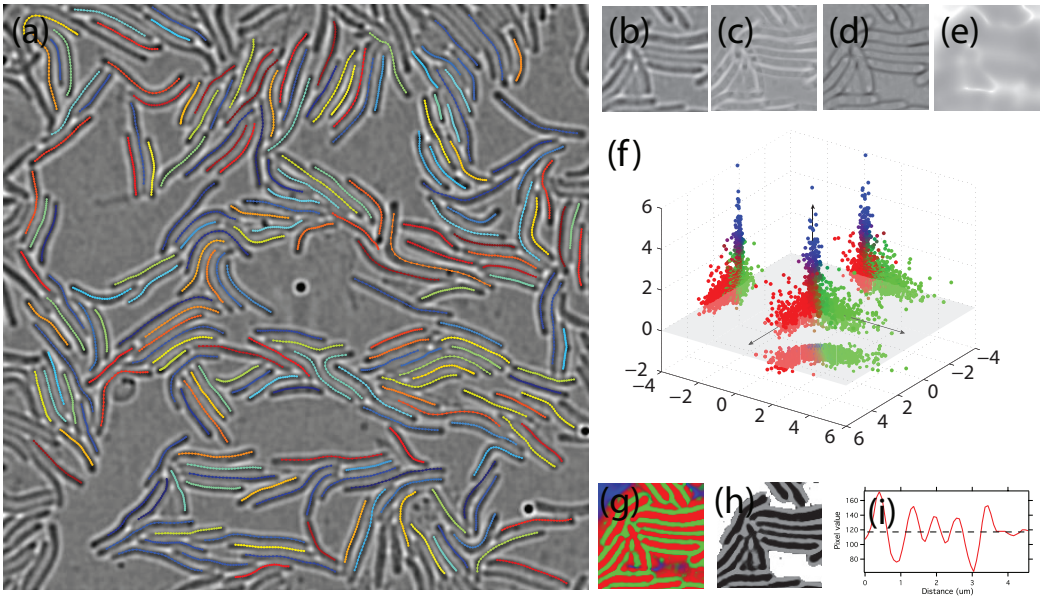

Figure 6.4: Raw image of *Myxococcus xanthus* cells is take under a bright field microscope, and the image is transformed into the probability map that is then used to generate the image potential to interact with the snakes. (a) A complete field of view of 41 μm$\times$ 41 μm (512$\times$512 pixels) contains about 200 *Myxococcus xanthus* cells. The relaxed position of the contours are overlaid on top of the grayscale image. (b) Zoomed in image of a portion in (a). (c,d) The large and the small eigenvalues of the Hessian matrix in (b). (e) The averaged eigenvectors can indicate the magnitude of alignment of eigenvectors. (f) The distribution of pixels in the classifier coordinate. Pixels are categorized into three groups along the three axes, and color-coded in red (ridge), green (valley) and blue (background). The projections along three axises are shown to assist vision. (g) After classification, each pixel in the image is color coded in the same way as in (f) according to the probability of being ridge, valley or background. (h) The enhanced image is calculated from the classification probability map shown in (g). (i) Image intensity profile on a line segment illustrates the nonuniform contrast at the edge and at the inside of a cell cluster.

where l^τ and l_0^τ are the actual length and target length at iteration τ, and l_0 is the normal length. The increased length is split between the two ends of the contour according to the resistant force exerted on the termini:

$$\Delta l_{head}^\tau = \frac{F_{tail}}{|F_{head}| + |F_{tail}|} \Delta l_0^\tau \tag{6.18}$$

$$\Delta l_{tail}^\tau = \frac{F_{head}}{|F_{head}| + |F_{tail}|} \Delta l_0^\tau, \tag{6.19}$$

where $F_{head} > 0$ and $F_{tail} < 0$ are the tangential components of the image and repulsive forces exerted on the termini. Figure 6.5 demonstrates how this inchworm-like motion corrects misplacement of the contours. With the length initially shortened, the initial crossing configuration is eliminated (Fig. 6.5b). The upper tip grows until it hits the ridge and is unable to grow further due to steric constraints (Fig. 6.5c, d). The lower tip keeps growing along a narrower valley until the length reaches the target length (Fig. 6.5e, f).

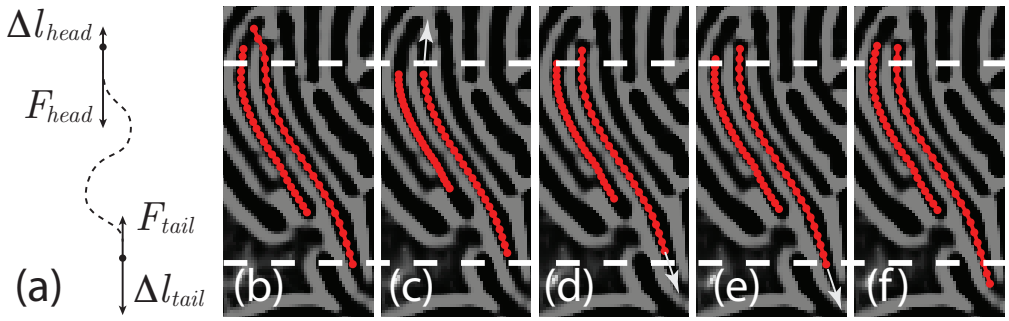

Figure 6.5: A snake can ride across a ridge and cause a marginally stable configuration, and allowing tips to grow solves this problem. (a) The total growth of the two ends of a contour is determined by the current length and the normal length of the contour. The growth is distributed unevenly to two ends according to the tangential resistance force. Dashed line indicates a hypothetical contour and the two ends are indicated by the round dots. (b) Without the growing ends, the contours are trapped in a marginally stable configuration, where the right contour leaks to the left pocket and squeezed left contour short. (c-f) The length of the contours are shortened initially and let grow. The white arrow indicates the direction of the tip growth, and the white dashed lines are the visual guide to help illustrate the growth.

I have also included several non-essential optimizations to the dynamics of the contours. The tangential component of the force exerted on each control point is individually calculated and the average value is applied on each control point. The arc distance between control points is also uniformly redistributed after a certain number of iterations. These optimizations improve the axial relaxation without qualitatively changing the behavior of the contours.

I used the repulsive snake model as described above to detect *Myxococcus xanthus* motion within a 41 μm$\times$41 μm field consisting of 512$\times$512 pixels (Fig. 6.4a). 205 cells are initially within the field of view and we tracked these cells for 400 frames at a rate of 12 frames/min. During the time course of the movie, cells move a distance about equal to 10 times their cell length and the local adjacency order is completely altered for most of the cells. Our algorithm successfully tracks 204 cells of the total 205 cells with one cell leaking into a neighboring cell image that entered the field in the middle of the movie. Figure 6.6a shows the projected traces of all 205 cells, labeled in different colors and overlaid on the first frame of the movie. These traces indicate that cells are capable of smoothly turning while gliding and reversing direction of motion. The tangential speed of one highly motile cell shows accurate velocity estimation and directional reversals approximately every 7 minutes (Fig. 6.6b). Figure 6.6(c) shows a histogram of the smoothed tangential speed of all 205 tracked cells. The speed roughly follows an exponential distribution with a mean and variance of $\sim 2\mu$m/min, in agreement with a previously reported values (REF!!!!).

6.4 Discussion

Active contour models are widely applied in detecting features with high contrast such as boundaries in an image and is shown to be successful especially for closed contours. Several studies applied the concept of active snake in detecting open con-

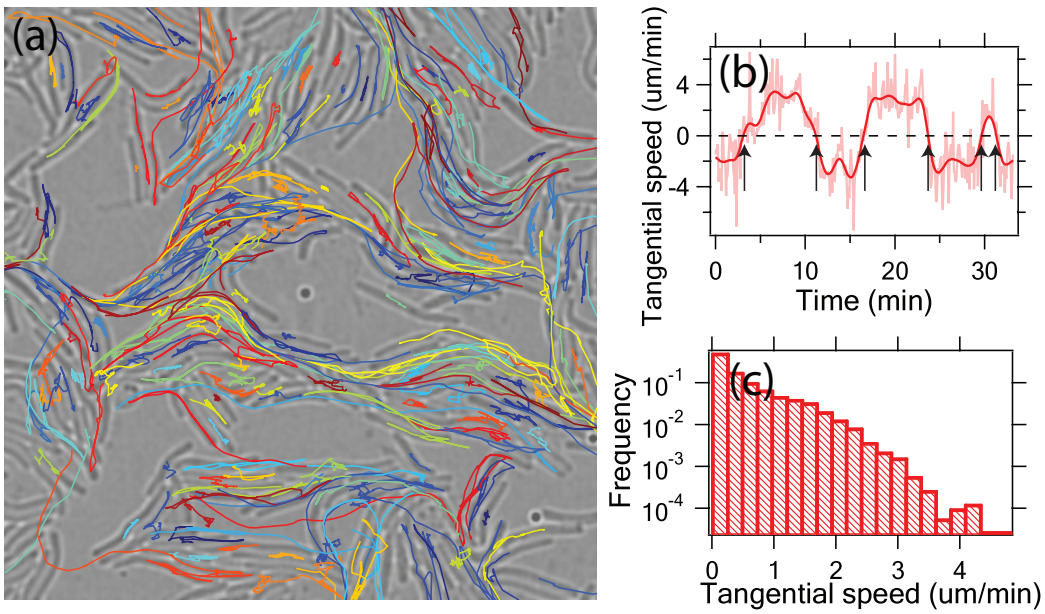

Figure 6.6: Tracking results of *Myxococcus xanthus* cells. (a) Trajectories of 202 cells are indicated in different colors, overlaid with the first frame of the movie. (b) The tangential gliding speed along the cell is plot against time. Raw speed trace (light red) is smoothed by Gaussian kernel with $\sigma = 72$ seconds (dark red). Six reversions are identified by the zero-crossings of the smoothed speed curve (indicated by arrows). (c) The histogram of gliding speed magnitude of 205 cells roughly follows an exponential distribution with mean and variance of 2 μm/min.

tours with finite length, for instance actin filaments. On the other hand, along with other machine vision techniques that segments targets from an image, active contour can be applied on individual images in time-lapsed movie in particle tracking problems. The solution is usually separated into two stages. The objects or particles are first identified in each frame individually, then the correspondence is assigned between objects in different frames. Merging/disappearing or splitting/emerging are allowed with specific statistical properties, usually in a maximum-likelihood fashion based on the intensity level, shape changes or moving distance. In this two-stage approach, the object assignment is limited by the object detection quality while it is not readily easy to use the inter-frame object assignment information to assist particle detection. Optimizing assignments across multiple frames can deal with single frame tracking error but dramatically increases computational expenses. In our approach, we treat

the temporal dimension as an extrusion of the spatial dimension of the images and the object trajectories as elastic continuum that interacts with both the stacked images and themselves as repulsive forces. Similar to the penalty based on moving distance in the linear assignment problem, the elastic energy in temporal dimension penalizes trajectories that deviates from linear motion, but different from the two-stage solutions, the correspondence assignment is part of the localization of the objects using image intensities.

Level set method is insensitive to the topology of the contours, and therefore ideal in dealing with contours with unspecified topological features. One drawback that limits the application of active contour and level set methods is the difficulty in applying shape constrains to the contours. This problem can be partly solved by using shape prior in level set approaches at the cost of computation time. However in many cases, the characteristic topological and geometrical features remain conserved through the entire movie, for instance the fly shape and size in the first example, cell length in the second example and the number of objects (flies, cells) in the two examples above. These conserved geometric characters are predetermined and placed as constraints to the solution in terms of the snake length in the first two examples and serves as explicit shape prior. In addition to resembling the physical shapes with geometric constrains in size and shape, our model also captures the mutually exclusive nature of these objects by adding the repulsive force, which effectively prevents trajectories from crossing or collapsing into one image potential minima as the physical repulsion prevents overlapping of the objects.

Another drawback of active contour methods is its sensitivity to the initial position and local minima in image potential. In the second example, ambiguous segmentation of cells takes place frequently due to the poor quality of the raw images, causing faulty gaps between cells and bumps along the cell body, especially in area of high cell density. Upon sudden cell acceleration, the linear prediction may place the ini-

tial position into a faulty local minimum as shown in figure 6.5(b). Among various segmentation algorithms, watershed is particularly suitable in dealing with varying boundary values, at the cost of the convenience to control the geometric properties of the segmented area. I adopt the idea of watershed algorithm in our active snake model in terms of dynamic contour length, and the tip growth are governed by the resistant forces on the two termini. This tip growth scheme is in directly analogy to the case in one dimensional watershed method, where the expansion of the two boundary points is inversely proportional to the steepness of the potential well. The combination of active contour and tip growth is essentially a watershed algorithm with an explicit shape prior that has the capability to correct mistakes caused by improper initial positions (figure 6.5(c-f)).

Image preprocessing is usually beneficial, sometimes essential in order for the active contours to relax into the correct potential minima. Because efficient dynamics of the contours requires a smooth potential landscape with slowly varying gradients, in our examples the raw images are all Gaussian smoothed before taking the gradient, or equivalently convolved by the derivative of gaussian (DoG) kernel. Several factor determines the blurring radius, including the spatial scale of the objects (fly width, cell width) and the distance between prediction and the true position of the objects, usually at the same scale of the moving distance between frames. The blurring kernel can be set variable depending on the motion of the objects, such as in the fly tracking case where fly undergoes normal walking behavior and occasional large distance jumps. I use a Gaussian kernel with the radius the same as the fly width for the former case to achieve fast performance, and if a jump is detected, a global linear attractive potential that is only visible to the jumping flies is added on top of the original kernel. The image preprocessing is more essential and subtle in the second example. Comparing to the raw images, the pixel intensity at the cell body, cell boundary and background is more uniform after we convert the pixel intensity into

assignment probability of three pixel categories. The elevated background intensity prevents contours from leaking to the outside, which is a severe problem if the image is not processed (data not shown). Pixel classification also enhances the barrier between cells and normalizes the pixel values on the cells.

Since the evolution of the contours follows explicit dynamics indicated in equation 6.3, it is convenient to implement additional factors that affects the tracking results in terms of explicit forces, or modify the elastic property to fit particular shape requirements. The length constraints and tip growth are applied in the form of explicit force in the case of tracking flies and *Myxococcus xanthus* cells. In the first example, we also add energy costs to penalize sharp turns, which is observed to cause identity swaps in rare ambiguous frames. In addition to applying explicit forces to the contours, the internal degrees of freedom of the contour curvature allows flexibility in modeling more complex shapes. For instance, the bending elasticity can be set as a variable along the contour instead of a constant, therefore allowing parts of the contour to act as soft joints and the rest as hard stems. This is especially suitable in tracking objects with internal motion such as head turning for mice.

Because the image information in adjacent frames are considered as a whole in the localization, minor corruptions in images can be corrected by the adjacent frames. On the other hand, major corruption can cause propagating errors in the following frames. The relaxation to the right image potential minimum suffers especially when the image potential energy landscape is highly curved with a large number of local minima, such as in the case of *Myxococcus xanthus* images where cells are bent and intertwined with identical local statistical character of pixel intensities. Inchworm tip growth has the ability to correct initial misplacement given that the cells only moves tangentially in a small amount (20%) relative to the cell length within two frames. Our algorithm also does not consider the case new objects entering the image. New

objects can be detected using other methods such level set and then treated as a regular repulsive active snake.

Comparing our active snake tracking model that uses the explicit dynamics of the contours with the Bayesian approaches such as in [20], the essential principles are correspondingly similar to model the physical properties of the objects. Active contour model treats images as a potential energy landscape, and the objects are described by a set of contours with specific lengths and bending properties to define the shape. Contours move according to the image potential with certain damping factor until relaxing at a minimum, and we add repulsion forces between objects to prevent merging. Correspondingly in Bayesian approaches, each image is treated as a spatial distribution of pixel vales, and an object is a parameterized distribution model with particular shape priors, such as the covariance and centroid of a Gaussian distribution. Tracking is essentially maximizing the posterior likelihood of the modeled distribution explaining the image, which involves a particular numerical gradient descending scheme similar to the damped dynamics of contours. A Gaussian mixture model is adopted in case of multiple object tracking, which clusters pixels into groups with small or no overlaps resembling repulsion between Gaussian mixtures.

Chapter 7

Conclusions

Mechanical cues are known to be important to cellular physiological function in both eukyreotes and prokyreotes. For bacteria, the key mechanical parameter, the membrane tension regulates the turgor pressure and cell growth rate. I used AFM and fluorescent microscopy to probe the elastic properties of live *E. coli* cells in a system that allows us to separately probe pressure and elasticity. Our results indicate that the turgor pressure in live cells is ~ 30 kPa, or ~ 0.3 atm. My data further indicate that the cell wall stress-stiffens. Stress–stiffening affords a unique mechanical advantage to cells by preventing abrupt cell shape changes against perturbations of external osmolarity while maintaining a relatively compliant cell elasticity under normal conditions. In combination with more compliant cytoplamic membrane, the nonlinear cell wall elasticity provides a passive adaptation strategy that balances between tension measurement sensitivity and protection against osmotic shocks.

The bacterial cell wall undergoes highly active remodeling during cell growth. For most bacteria, maintaining a specific shape is essential for many cell functions internally and externally when interacting with the environment. The shape of the bacteria cell wall is determined by the spatial and temporal order of the material insertion along the cell wall, yet the specific insertion rules are elusive. To depict the temporal-

spatial growth order, I developed a novel platform that used high density fluorescent labeling over the entire rod-shaped gram-positive bacteria *B. subtilis* cell surface to capture the morphological changes of the cell wall at sub-cellular to diffraction-limited spatial resolution and minute temporal resolution. Assisted by this approach, I found that chaining *B. subtilis* cells grow and twist in a highly heterogeneous fashion both spatially and temporally. Regions of high growth and twisting activity have a typical length scale of 5 μm, and the growth rate persists for 10-40 minutes. Whether this heterogeneity of growth is caused by the distribution of the peptidoglycan synthesis complexes internally, or by inter-cellular differentiation among individual segregated cells remains unknown. This platform is also able to connect the distribution and motion of the PG synthesis complexes to the actual material insertion to help understand how microscopic molecular process self-organizes to give rise to a global order in the cell shape.

Motivated by the need to resolve densely distributed quantum dots on the surface of the cells at high temporal resolution for cell wall growth map measurements, I developed a super-resolution imaging technique based on the statistics of the intrinsic fluorescence intermittence of quantum dots, namely the Spatial Covariance Reconstruction (SCORE) microscopy. It makes use of the intensity fluctuation variation correlation between all pairs of pixels and the known point spread function (PSF) to reconstruct a probability density map for the fluorophore distribution. It achieves sub-diffraction lateral resolution of 100 nm from 5 to 7 seconds of imaging. Comparing with the single particle localization based techniques such as STORM, PALM and FIONA, SCORE is typically 10 to 100 times faster. SCORE microscopy is insensitive to background and can be applied to different types of fluorescence sources, including but not limited to organic dye and quantum dot that we have tested experimentally in this work. It is also easy to implement experimentally with virtually no change to the

existing imaging setup, and can be extended to three-dimensional super-resolution imaging.

Also initiated from the cell wall growth map project, I developed a multiple-object tracking algorithm for time-lapsed movie based on the active contour model, taking into account the physical exclusion of the objects. In our model, multiple oval-shaped or elongated curved objects are represented by open elastic contours with individually fixed length in each frame, and the motion of objects in time is treated as an extrusion in the temporal dimension, thus the spatio-temporal kymograph are modeled as mutually repulsive elastic membranes. We illustrated the application of the repulsive active membrane model on two sets of realistic experimental data, tracking multiple *Drosophila* walking and chasing, and tracking individual curved gliding bacteria *Myxococcus xanthus* at high density. Individual objects are successfully tracked at high efficiency at video frequency with low error rate ($10^{-}4$) that can be conveniently corrected in additional separate steps.

Appendix A

E. coli strain YD133 and YD143 construction

A.1 Introducing gene knockouts from the Keio Collection

E. coli strain YD133 ($\Delta fimA\Delta fliC\Delta flgE$) is constructed from strain K-12, and the deletions are introduced from the Keio Collection by P1 transduction following the protocols described in [9]. The Keio collection is a library of *E. coli* nonessential gene knockouts, specifically replaced with a cassette of kanamycin resistance gene and FLP recognition target (FRT) sites. The cassette can be easily introduced to a recipient strain by transduction to delete any target gene, and then the cassette can be removed by FLP recombinase. In this protocol, the FLP recombinase is carried by a plasmid pCP20 that also has a temperature sensitive replicon. After the cassette is removed, the plasmid curing is achieved by growing the cells at a specific temperature.

A.2 Construction of YD133

To construct *E. coli* strain YD133, I started from the *flgE::kan* strain from the Keio Collection. Plasmid pCP20 is transformed into strain K-12 *flgE::kan* by electroporation. The transformants are grown on LB agar plates containing 10 μg/ml chloramphenicol and 50 μg/ml ampicillin at 30°C overnight. Transformants picked from the resulted colonies are grown in LB liquid media containing 10 μg/ml chloramphenicol and 50 μg/ml ampicillin at 30°C overnight to pop out the kanamycin resistance cassette in the recipient strain, then subcultured and grown at 37°C to cure the pCP20 plasmid. The deletion of the *kan* cassette and the plasmid curing can be verified according to the sensitivity of kanamycin, chloramphenicol and ampicillin.

To introduce new gene deletion to a strain, the recipient strain is transfected with the P1*vir* lysates of the donor strain from the Keio Collection. The detailed protocol of preparing lysates and transduction is listed in the following sections. The transductants are grown on LB agar plates containing 50 μg/ml kanamycin to select for the *kan* cassette from the donor strain. After the target gene is replaced, the cassette can be removed by the procedure described above using plasmid pCP20. Following this protocol, I sequentially deleted *flgE* and *fimA* to finally obtain strain YD133.

A.3 Construction of YD143

E. coli strain YD143 ($\Delta fimA\Delta fliC\Delta flgE$ *imp4213*) was constructed for the bulging experiment probed with AFM. This strain carries a frame deletion in the lptD gene, that gives *imp*4213 strain a higher permeability than the wild type cells. YD143 was built by introduction *lptD* mutation into strain YD133 that had no surface appendages by P1 transduction following the procedure in [116]. Briefly, lysate of *E. coli* strain NR693 (MC4100 *carB::Tn10 imp4213*) was prepared in advance, and was used

to transfect the recipient strain YD133. The transductant was grown on selective LB plate containing 12.5 μg/ml tetracycline. The $carB :: Tn10$ allele is 20%-25% linked to the *imp* locus, thus the around one fifth of the transductants contains the *imp*4213 mutation, which is verified by the inability to grow on MacConkey agar. The $carB :: Tn10$ allele was then removed by a transduction with the *imp*4213 lysate to make strain YD143 by selective growth on the M63 minimal plates because $carB$ null mutants cannot grow on minimal media. The YD143 is verified by its sensitivity to vancomycin, tetracycline, MocConkey agar, and the ability to grow in minimal media.

A.4 Preparation of and Transduction Using P1*vir* Lysates

The protocol listed here are the same as described in [127]. For reader's reference, the protocol is repeated here:

1. Inoculate a single colony of the donor strain in 5 ml LB medium and shake at 37°C overnight.

2. Inoculate 0.05 ml of the overnight culture in 5 ml of LB medium containing 0.2% glucose and 5 mM $CaCl_2$.

3. Incubate for 30 minutes at 37°C with aeration.

4. Add 0.1 ml of a P1*vir* lysate (5×10^8 phage/ml).

5. Shake or rotate at 37°C for 2-3 hours until the cell lyse.

6. Add 0.1 ml of chloroform and vortex.

7. Centrifuge at 4500g for 10 minutes to pellet the debris.

8. Carefully transfer the supernatant to a sterile, screw-capped tube. Add 0.1 ml of chloroform and vortex to mix. Store the lysate at 4°C.

To introduce a gene into the recipient strain by transduction, follow the following protocol:

1. Inoculate a single colony of the recipient strain in 5 ml LB medium and shake at 37°C overnight.

2. Centrifuge the overnight culture at 1500g for 10 minutes and resuspend the cell pellet in 2.5 ml of 10 mM $MgSO_4$ containing 5ml $CaCl_2$.

3. To 0.1 ml of resuspend cells in tubes, add variable amount of P1 lysate, usually from 10 μl to 0.1 ml. Also prepare a tube of just the P1 lysate as a negative control.

4. Incubate the tubes for 30 minutes at 30°C without shaking.

5. Add 1m of LB with 10 mM sodium citrate.

6. Incubate 30 minutes at 30-37°C without shaking.

7. Centrifuge 1500g for 10 minute to pellet. Discard the supernatant.

8. Add 0.1 ml of 1 M sodium citrate.

9. Plate onto selective medium. For introducing the *kan* cassette from the Keio Collection, use 50 μg/ml kanamycin.

Appendix B

Labeling *Bacillus Subtilis* Surface Amine Groups

In order to visualize the cell wall growth, the surface of *B. subtilis* is decorated with high density of fluorescence markers. In brief, carboxyl quantum dots are covalently conjugated to the surface amine groups by N-ethyl-N-dimethylaminopropyl-carbodiimide (EDC). Since EDC is toxic, the conditions that cells are exposed to are carefully designed and controlled.

Labeling protocol:

1. Grow *B. subtilis* in the modified LB medium at 37°C in the shaker till optical density 0.1. Do not over grow cells or labeling will fail. The modified LB medium contains no sodium chloride but buffered by 20 mM potassium phosphate salts to pH 7.5-7.8

2. Prepare *fresh* 4 mg/ml EDC and 11 mg/ml sulfo-NHS (N-hydroxy sulfosuccinimide) solution in 10 mM pH 5.8-6.0 MES buffer. Sulfo-NHS is added to increase the stability of active intermediates.

3. Mix 2.5 ul 10 mM pH 5.8-6.0 MES buffer, 2.5 ul EDC solution in MES, 2.5 ul sulfo-NHS solution and 1-2.5 ul 8 uM carboxyl quantum dots (Invitrogen). React on

roter for 15 minutes at room temperature.

4. Dialyze the active quantum dots in at least 200 ml 10 mM MES buffer with a 20K MWCO mini dialysis tube (Fisher Scientific) for 15 minutes to remove the excess EDC and sulfo-NHS.

5. During this time, harvest cells, wash them in the incubation buffer three times. The incubation buffer contains 50 mM potassium phosphate buffer at pH 7.5-7.8, 0.1% w/v glucose and 2 mM $MgSO_4$. The final density of cells should be set to equivalent to OD 1-10.

6. Mix the dialyzed quantum dots with washed cells. Incubate at room temperature for 20 to 90 minutes.

7. Wash the labeled cells in the incubation buffer 3 times to remove the floating quantum dots.

Notes:

1. Overgrown *B. subtilis* are much harder to label, even under the optimized conditions.

2. EDC and Sulfo-NHS hydrolyzes in hours. Do not store the solution.

3. High salt concentration will cause quantum dots to aggregate. In practice, avoid total salt concentration that is greater than 60 mM. 4. Glucose and magnesium sulphate are added to the incubation buffer to keep the stress level to the minimum. Stressed cells usually do not grow under excitation light.

Appendix C

Controller for the Home-built Laser

The excitation laser used in the *B subtilis* experiment is a 532 nm wavelength diode laser powered by a home-built controller. The controller is required to output up to 500 mA constant current at 2.5-3.1 V, and to switch on and off at millisecond time scale. The controller takes two input signals, one from the camera exposure signal, the other from the digital output of the data acquisition board, and the output current is given only both of the signals are at high. For the convenience of driving the diode without input signal, when the input signals are unplugged, the input is set to high. For future reference, the circuit diagram is listed below.

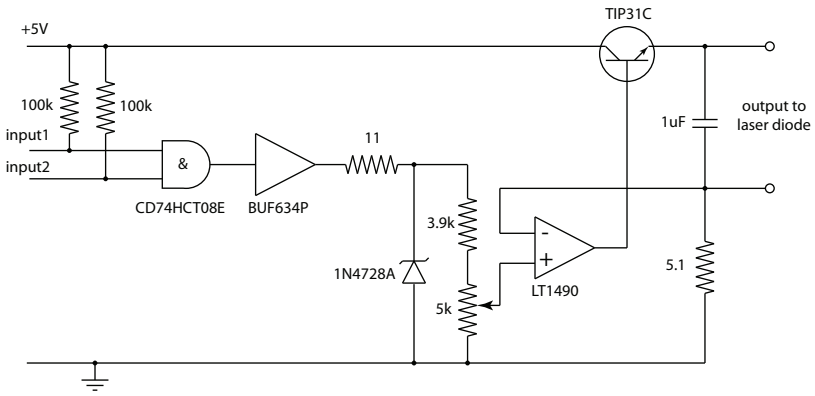

Figure C.1: The circuit diagram of the home-built laser controller.

Bibliography

[1] Virgile Adam, Mickal Lelimousin, Susan Boehme, Guillaume Desfonds, Karin Nienhaus, Martin J Field, Joerg Wiedenmann, Sean McSweeney, G. Ulrich Nienhaus, and Dominique Bourgeois. Structural characterization of irisfp, an optical highlighter undergoing multiple photo-induced transformations. *Proc Natl Acad Sci U S A*, 105(47):18343–18348, Nov 2008.

[2] Ariel Amir and David R Nelson. Dislocation-mediated growth of bacterial cell walls. *Proc Natl Acad Sci U S A*, 109(25):9833–9838, Jun 2012.

[3] Ryoko Ando, Hideaki Mizuno, and Atsushi Miyawaki. Regulated fast nucleocytoplasmic shuttling observed by reversible protein highlighting. *Science*, 306(5700):1370–1373, Nov 2004.

[4] Guillaume Andre, Saulius Kulakauskas, Marie-Pierre Chapot-Chartier, Benjamine Navet, Marie Deghorain, Elvis Bernard, Pascal Hols, and Yves F Dufrne. Imaging the nanoscale organization of peptidoglycan in living lactococcus lactis cells. *Nat Commun*, 1:27, 2010.

[5] M. Arnoldi, M. Fritz, E. Buerlein, M. Radmacher, E. Sackmann, and A. Boulbitch. Bacterial turgor pressure can be measured by atomic force microscopy. *Phys Rev E Stat Phys Plasmas Fluids Relat Interdiscip Topics*, 62(1 Pt B):1034–1044, Jul 2000.

[6] A. Dabiri Askari, F. Feihl, and B. Waeber. [arterial hypertension: macrocirculation and microcirculation]. *Rev Med Suisse*, 5(216):1778–80, 1782, Sep 2009.

[7] R. AUSTRIAN. The gram stain and the etiology of lobar pneumonia, an historical note. *Bacteriol Rev*, 24(3):261–265, Sep 1960.

[8] Marcela Avila-Prez, Jeroen B van der Steen, Remco Kort, and Klaas J Hellingwerf. Red light activates the sigmab-mediated general stress response of bacillus subtilis via the energy branch of the upstream signaling cascade. *J Bacteriol*, 192(3):755–762, Feb 2010.

[9] Tomoya Baba, Takeshi Ara, Miki Hasegawa, Yuki Takai, Yoshiko Okumura, Miki Baba, Kirill A. Datsenko, Masaru Tomita, Barry L. Wanner, and Hirotada Mori. Construction of escherichia coli k-12 in-frame, single-gene knockout mutants: the keio collection. *Mol Syst Biol*, 2:2006.0008, 2006.

[10] W. W. Baldwin, R. Myer, T. Kung, E. Anderson, and A. L. Koch. Growth and buoyant density of escherichia coli at very low osmolarities. *J Bacteriol*, 177(1):235–237, Jan 1995.

[11] Arturo M. Bar and Ronald G. Reifenberger. *Atomic Force Microscopy in Liquid: Biological Applications*. Wiley-VCH, 2012.

[12] John Bechhoefer. Feedback for physicists: A tutorial essay on control. *Reviews of Modern Physics*, 77(3):783, 2005.

[13] J. Bereiter-Hahn. Mechanics of crawling cells. *Med Eng Phys*, 27(9):743–753, Nov 2005.

[14] C. Berrier, A. Coulombe, I. Szabo, M. Zoratti, and A. Ghazi. Gadolinium ion inhibits loss of metabolites induced by osmotic shock and large stretch-activated channels in bacteria. *Eur J Biochem*, 206(2):559–565, Jun 1992.

[15] Eric Betzig, George H Patterson, Rachid Sougrat, O. Wolf Lindwasser, Scott Olenych, Juan S Bonifacino, Michael W Davidson, Jennifer Lippincott-Schwartz, and Harald F Hess. Imaging intracellular fluorescent proteins at nanometer resolution. *Science*, 313(5793):1642–1645, Sep 2006.

[16] D. C. Birdsell and E. H. Cota-Robles. Production and ultrastructure of lysozyme and ethylenediaminetetraacetate-lysozyme spheroplasts of escherichia coli. *J Bacteriol*, 93(1):427–437, Jan 1967.

[17] Tanneke Den Blaauwen, Mirjam E G Aarsman, Norbert O E Vischer, and Nanne Nanninga. Penicillin-binding protein pbp2 of escherichia coli localizes preferentially in the lateral wall and at mid-cell in comparison with the old cell pole. *Mol Microbiol*, 47(2):539–547, Jan 2003.

[18] Ian R Booth, Michelle D Edwards, Susan Black, Ulrike Schumann, and Samantha Miller. Mechanosensitive channels in bacteria: signs of closure? *Nat Rev Microbiol*, 5(6):431–440, Jun 2007.

[19] A. Boulbitch, B. Quinn, and D. Pink. Elasticity of the rod-shaped gram-negative eubacteria. *Phys. Rev. Lett.*, 85(24):5246–5249, Dec 2000.

[20] Kristin Branson, Alice A Robie, John Bender, Pietro Perona, and Michael H Dickinson. High-throughput ethomics in large groups of drosophila. *Nat Methods*, 6(6):451–457, Jun 2009.

[21] Robert A Britton, Patrick Eichenberger, Jose Eduardo Gonzalez-Pastor, Paul Fawcett, Rita Monson, Richard Losick, and Alan D Grossman. Genome-wide analysis of the stationary-phase sigma factor (sigma-h) regulon of bacillus subtilis. *J Bacteriol*, 184(17):4881–4890, Sep 2002.

[22] C. P. Broedersz, C. Storm, and F. C. MacKintosh. Nonlinear elasticity of composite networks of stiff biopolymers with flexible linkers. *Phys Rev Lett*, 101(11):118103, Sep 2008.

[23] C. Bustamante, J. F. Marko, E. D. Siggia, and S. Smith. Entropic elasticity of lambda-phage dna. *Science*, 265(5178):1599–1600, Sep 1994.

[24] Matthew T Cabeen and Christine Jacobs-Wagner. Bacterial cell shape. *Nat Rev Microbiol*, 3(8):601–610, Aug 2005.

[25] E. Canale-Parola. Motility and chemotaxis of spirochetes. *Annu Rev Microbiol*, 32:69–99, 1978.

[26] D. S. Cayley, H. J. Guttman, and M. T. Record. Biophysical characterization of changes in amounts and activity of escherichia coli cell and compartment water and turgor pressure in response to osmotic stress. *Biophys J*, 78(4):1748–1764, Apr 2000.

[27] Thorben Cordes, Ingo H. Stein, Carsten Forthmann, Christian Steinhauer, Monika Walz, Wolfram Summerer, Britta Person, Jan Vogelsang, and Philip Tinnefeld. Controlling the emission of organic dyes for high sensitivity and super-resolution microscopy. In *Advanced Microscopy Techniques*, page 7367 1D. Optical Society of America, 2009.

[28] T H Cormen. *Introduction to Algorithms*. MIT Press, Cambridge, Massachusetts, USA, 2001.

[29] Ben Corry and Boris Martinac. Bacterial mechanosensitive channels: experiment and theory. *Biochim Biophys Acta*, 1778(9):1859–1870, Sep 2008.

[30] Susan Cox, Edward Rosten, James Monypenny, Tijana Jovanovic-Talisman, Dylan T Burnette, Jennifer Lippincott-Schwartz, Gareth E Jones, and Rainer Heintzmann. Bayesian localization microscopy reveals nanoscale podosome dynamics. *Nat Methods*, 9(2):195–200, Feb 2012.

[31] J. Dai and M. P. Sheetz. Regulation of endocytosis, exocytosis, and shape by membrane tension. *Cold Spring Harb Symp Quant Biol*, 60:567–571, 1995.

[32] Kristopher E Daly, Kerwyn Casey Huang, Ned S Wingreen, and Ranjan Mukhopadhyay. Mechanics of membrane bulging during cell-wall disruption in gram-negative bacteria. *Phys Rev E Stat Nonlin Soft Matter Phys*, 83(4 Pt 1):041922, Apr 2011.

[33] Fabrice de Chaumont, Renata Dos-Santos Coura, Pierre Serreau, Arnaud Cressant, Jonathan Chabout, Sylvie Granon, and Jean-Christophe Olivo-Marin. Computerized video analysis of social interactions in mice. *Nat Methods*, 9(4):410–417, 2012.

[34] P. J. de Pablo, I. A T Schaap, F. C. MacKintosh, and C. F. Schmidt. Deformation and collapse of microtubules on the nanometer scale. *Phys Rev Lett*, 91(9):098101, Aug 2003.

[35] M. A. de Pedro, J. C. Quintela, J. V. Hltje, and H. Schwarz. Murein segregation in escherichia coli. *J Bacteriol*, 179(9):2823–2834, May 1997.

[36] Peter Dedecker, Gary C H Mo, Thomas Dertinger, and Jin Zhang. Widely accessible method for superresolution fluorescence imaging of living systems. *Proc Natl Acad Sci U S A*, 109(27):10909–10914, Jul 2012.

[37] Graham T Dempsey, Joshua C Vaughan, Kok Hao Chen, Mark Bates, and Xiaowei Zhuang. Evaluation of fluorophores for optimal performance in localization-based super-resolution imaging. *Nat Methods*, 8(12):1027–1036, Dec 2011.

[38] Yi Deng, Mingzhai Sun, and Joshua W. Shaevitz. Direct measurement of cell wall stress stiffening and turgor pressure in live bacterial cells. *Phys Rev Lett*, 107(15):158101, Oct 2011.

[39] T. Dertinger, R. Colyer, G. Iyer, S. Weiss, and J. Enderlein. Fast, background-free, 3d super-resolution optical fluctuation imaging (sofi). *Proc Natl Acad Sci U S A*, 106(52):22287–22292, Dec 2009.

[40] Thomas Dertinger, Ryan Colyer, Robert Vogel, Jrg Enderlein, and Shimon Weiss. Achieving increased resolution and more pixels with superresolution optical fluctuation imaging (sofi). *Opt Express*, 18(18):18875–18885, Aug 2010.

[41] Christopher Dombrowski, Wanxi Kan, Md Abdul Motaleb, Nyles W Charon, Raymond E Goldstein, and Charles W Wolgemuth. The elastic basis for the shape of borrelia burgdorferi. *Biophys J*, 96(11):4409–4417, Jun 2009.

[42] Julia Domnguez-Escobar, Arnaud Chastanet, Alvaro H Crevenna, Vincent Fromion, Roland Wedlich-Sldner, and Rut Carballido-Lpez. Processive movement of mreb-associated cell wall biosynthetic complexes in bacteria. *Science*, 333(6039):225–228, Jul 2011.

[43] K. Dutton, S. Thompson, and B. Barraclough. *The Art of Control Engineering*. Addison-Wesley, Harlow, England, 1997.

[44] U. S. Eggert, N. Ruiz, B. V. Falcone, A. A. Branstrom, R. C. Goldman, T. J. Silhavy, and D. Kahne. Genetic basis for activity differences between vancomycin and glycolipid derivatives of vancomycin. *Science*, 294(5541):361–364, Oct 2001.

[45] D. J. Fife, D. F. Bruhn, K. S. Miller, and D. L. Stoner. Evaluation of a fluorescent lectin-based staining technique for some acidophilic mining bacteria. *Appl Environ Microbiol*, 66(5):2208–2210, May 2000.

[46] Marshall Fixman. Classical statistical mechanics of constraints: A theorem and application to polymers. *Proc Natl Acad Sci U S A*, 71(8):3050–3053, Aug 1974.

[47] Ingo Fritz, Carsten Strmpl, and Wolf-Rainer Abraham. Phylogenetic relationships of the genera stella, labrys and angulomicrobium within the 'alphaproteobacteria' and description of angulomicrobium amanitiforme sp. nov. *Int J Syst Evol Microbiol*, 54(Pt 3):651–657, May 2004.

[48] Leon Furchtgott, Ned S Wingreen, and Kerwyn Casey Huang. Mechanisms for maintaining cell shape in rod-shaped gram-negative bacteria. *Mol Microbiol*, Apr 2011.

[49] Lu Gan, Songye Chen, and Grant J Jensen. Molecular organization of gram-negative peptidoglycan. *Proc Natl Acad Sci U S A*, 105(48):18953–18957, Dec 2008.

[50] M. L. Gardel, J. H. Shin, F. C. MacKintosh, L. Mahadevan, P. Matsudaira, and D. A. Weitz. Elastic behavior of cross-linked and bundled actin networks. *Science*, 304(5675):1301–1305, May 2004.

[51] Ethan C Garner, Remi Bernard, Wenqin Wang, Xiaowei Zhuang, David Z Rudner, and Tim Mitchison. Coupled, circumferential motions of the cell wall synthesis machinery and mreb filaments in b. subtilis. *Science*, 333(6039):222–225, Jul 2011.

[52] Anindya S Ghosh and Kevin D Young. Helical disposition of proteins and lipopolysaccharide in the outer membrane of escherichia coli. *J Bacteriol*, 187(6):1913–1922, Mar 2005.

[53] Zemer Gitai, Natalie Anne Dye, Ann Reisenauer, Masaaki Wachi, and Lucy Shapiro. Mreb actin-mediated segregation of a specific region of a bacterial chromosome. *Cell*, 120(3):329–341, Feb 2005.

[54] S. F. Goldstein and N. W. Charon. Motility of the spirochete leptospira. *Cell Motil Cytoskeleton*, 9(2):101–110, 1988.

[55] E. W. Goodell. Recycling of murein by escherichia coli. *J Bacteriol*, 163(1):305–310, Jul 1985.

[56] Manuel Guizar-Sicairos, Samuel T Thurman, and James R Fienup. Efficient subpixel image registration algorithms. *Opt Lett*, 33(2):156–158, Jan 2008.

[57] Mats G L Gustafsson. Nonlinear structured-illumination microscopy: wide-field fluorescence imaging with theoretically unlimited resolution. *Proc Natl Acad Sci U S A*, 102(37):13081–13086, Sep 2005.

[58] O. P. Hamill and B. Martinac. Molecular basis of mechanotransduction in living cells. *Physiol Rev*, 81(2):685–740, Apr 2001.

[59] Emma J Hayhurst, Lekshmi Kailas, Jamie K Hobbs, and Simon J Foster. Cell wall peptidoglycan architecture in bacillus subtilis. *Proc Natl Acad Sci U S A*, 105(38):14603–14608, Sep 2008.

[60] Michael Hecker, Jan Pan-Farr, and Uwe Vlker. Sigb-dependent general stress response in bacillus subtilis and related gram-positive bacteria. *Annu Rev Microbiol*, 61:215–236, 2007.

[61] S. W. Hell and J. Wichmann. Breaking the diffraction resolution limit by stimulated emission: stimulated-emission-depletion fluorescence microscopy. *Opt Lett*, 19(11):780–782, Jun 1994.

[62] Stefan W Hell. Far-field optical nanoscopy. *Science*, 316(5828):1153–1158, May 2007.

[63] J. Nathan Henderson, Hui-wang Ai, Robert E. Campbell, and S. James Remington. Structural basis for reversible photobleaching of a green fluorescent protein homologue. *Proceedings of the National Academy of Sciences*, 104(16):6672–6677, 2007.

[64] Samuel T Hess, Thanu P K Girirajan, and Michael D Mason. Ultra-high resolution imaging by fluorescence photoactivation localization microscopy. *Biophys J*, 91(11):4258–4272, Dec 2006.

[65] J. O. Hjortdal. Extensibility of the normo-hydrated human cornea. *Acta Ophthalmol Scand*, 73(1):12–17, Feb 1995.

[66] Michael Hofmann, Christian Eggeling, Stefan Jakobs, and Stefan W Hell. Breaking the diffraction barrier in fluorescence microscopy at low light intensities by using reversibly photoswitchable proteins. *Proc Natl Acad Sci U S A*, 102(49):17565–17569, Dec 2005.

[67] Seamus J Holden, Stephan Uphoff, and Achillefs N Kapanidis. Daostorm: an algorithm for high- density super-resolution microscopy. *Nat Methods*, 8(4):279–280, Apr 2011.

[68] Daryl P Holland and Anthony E Walsby. Digital recordings of gas-vesicle collapse used to measure turgor pressure and cell-water relations of cyanobacterial cells. *J Microbiol Methods*, 77(2):214–224, May 2009.

[69] Kerwyn Casey Huang, Ranjan Mukhopadhyay, Bingni Wen, Zemer Gitai, and Ned S Wingreen. Cell shape and cell-wall organization in gram-negative bacteria. *Proc Natl Acad Sci U S A*, 105(49):19282–19287, Dec 2008.

[70] J. V. Hltje. Growth of the stress-bearing and shape-maintaining murein sacculus of escherichia coli. *Microbiol Mol Biol Rev*, 62(1):181–203, Mar 1998.

[71] P. A. Janmey, S. Hvidt, J. Ks, D. Lerche, A. Maggs, E. Sackmann, M. Schliwa, and T. P. Stossel. The mechanical properties of actin gels. elastic modulus and filament motions. *J Biol Chem*, 269(51):32503–32513, Dec 1994.

[72] Khuloud Jaqaman, Dinah Loerke, Marcel Mettlen, Hirotaka Kuwata, Sergio Grinstein, Sandra L Schmid, and Gaudenz Danuser. Robust single-particle tracking in live-cell time-lapse sequences. *Nat Methods*, 5(8):695–702, Aug 2008.

[73] Hongyuan Jiang and Sean X. Sun. Morphology, growth, and size limit of bacterial cells. *Phys. Rev. Lett.*, 105(2):028101, Jul 2010.

[74] Suckjoon Jun and Andrew Wright. Entropy as the driver of chromosome segregation. *Nat Rev Microbiol*, 8(8):600–607, Aug 2010.

[75] Michael Kass, Andrew Witkin, and Demetri Terzopoulos. Snakes: Active contour models. *INTERNATIONAL JOURNAL OF COMPUTER VISION*, 1:321–331, 1988.

[76] Yoshikazu Kawai, Kei Asai, and Jeffery Errington. Partial functional redundancy of mreb isoforms, mreb, mbl and mrebh, in cell morphogenesis of bacillus subtilis. *Mol Microbiol*, 73(4):719–731, Aug 2009.

[77] Daniel B Kearns and Richard Losick. Cell population heterogeneity during growth of bacillus subtilis. *Genes Dev*, 19(24):3083–3094, Dec 2005.

[78] Taeyoon Kim, Wonmuk Hwang, Hyungsuk Lee, and Roger D. Kamm. Computational analysis of viscoelastic properties of crosslinked actin networks. *PLoS Comput Biol*, 5(7):e1000439, 07 2009.

[79] T. A. Klar and S. W. Hell. Subdiffraction resolution in far-field fluorescence microscopy. *Opt Lett*, 24(14):954–956, Jul 1999.

[80] W. Klein, U. Ehmann, and W. Boos. The repression of trehalose transport and metabolism in escherichia coli by high osmolarity is mediated by trehalose-6-phosphate phosphatase. *Res Microbiol*, 142(4):359–371, May 1991.

[81] A. L. Koch and R. J. Doyle. Inside-to-outside growth and turnover of the wall of gram-positive rods. *J Theor Biol*, 117(1):137–157, Nov 1985.

[82] G. H. Koenderink, M. Atakhorrami, F. C. MacKintosh, and C. F. Schmidt. High-frequency stress relaxation in semiflexible polymer solutions and networks. *Phys Rev Lett*, 96(13):138307, Apr 2006.

[83] L.D. Landau and E.M. Lifshitz. *Theory of Elasticity. Course of Theoretical Physics. Vol. 7 (third ed.)*. Pergamon, Oxford, 1986.

[84] J. F. Leterrier, J. Ks, J. Hartwig, R. Vegners, and P. A. Janmey. Mechanical effects of neurofilament cross-bridges. modulation by phosphorylation, lipids, and interactions with f-actin. *J Biol Chem*, 271(26):15687–15694, Jun 1996.

[85] N. Levina, S. Ttemeyer, N. R. Stokes, P. Louis, M. A. Jones, and I. R. Booth. Protection of escherichia coli cells against extreme turgor by activation of mscs and mscl mechanosensitive channels: identification of genes required for mscs activity. *EMBO J*, 18(7):1730–1737, Apr 1999.

[86] Hongsheng Li, Tian Shen, Dimitrios Vavylonis, and Xiaolei Huang. Actin filament segmentation using spatiotemporal active-surface and active-contour models. *Med Image Comput Comput Assist Interv*, 13(Pt 1):86–94, 2010.

[87] Keith Lidke, Bernd Rieger, Thomas Jovin, and Rainer Heintzmann. Superresolution by localization of quantum dots using blinking statistics. *Opt Express*, 13(18):7052–7062, Sep 2005.

[88] A.E.H. Love. The small free vibrations and deformation of a thin elastic shell. *Philosophical Transactions of the Royal Society of London. A*, 179:491–546, 1888.

[89] Andrew L Lovering, Susan S Safadi, and Natalie C J Strynadka. Structural perspective of peptidoglycan biosynthesis and assembly. *Annu Rev Biochem*, 81:451–478, 2012.

[90] L. Ma, J. Xu, P. A. Coulombe, and D. Wirtz. Keratin filament suspensions show unique micromechanical properties. *J Biol Chem*, 274(27):19145–19151, Jul 1999.

[91] Hdia Maamar, Arjun Raj, and David Dubnau. Noise in gene expression determines cell fate in bacillus subtilis. *Science*, 317(5837):526–529, Jul 2007.

[92] P. Maupin and T. D. Pollard. Improved preservation and staining of hela cell actin filaments, clathrin-coated membranes, and other cytoplasmic structures by tannic acid-glutaraldehyde-saponin fixation. *J Cell Biol*, 96(1):51–62, Jan 1983.

[93] J. A. Maurer and D. A. Dougherty. A high-throughput screen for mscl channel activity and mutational phenotyping. *Biochim Biophys Acta*, 1514(2):165–169, Oct 2001.

[94] John C Meeks and Jeff Elhai. Regulation of cellular differentiation in filamentous cyanobacteria in free-living and plant-associated symbiotic growth states. *Microbiol Mol Biol Rev*, 66(1):94–121; table of contents, Mar 2002.

[95] N. H. Mendelson, J. E. Sarlls, C. W. Wolgemuth, and R. E. Goldstein. Chiral self-propulsion of growing bacterial macrofibers on a solid surface. *Phys Rev Lett*, 84(7):1627–1630, Feb 2000.

[96] N. H. Mendelson and J. J. Thwaites. Cell wall mechanical properties as measured with bacterial thread made from bacillus subtilis. *J Bacteriol*, 171(2):1055–1062, Feb 1989.

[97] Samy O Meroueh, Krisztina Z Bencze, Dusan Hesek, Mijoon Lee, Jed F Fisher, Timothy L Stemmler, and Shahriar Mobashery. Three-dimensional structure of the bacterial cell wall peptidoglycan. *Proc Natl Acad Sci U S A*, 103(12):4404–4409, Mar 2006.

[98] Samy O Meroueh, Jed F Fisher, H. Bernhard Schlegel, and Shahriar Mobashery. Ab initio qm/mm study of class a beta-lactamase acylation: dual participation of glu166 and lys73 in a concerted base promotion of ser70. *J Am Chem Soc*, 127(44):15397–15407, Nov 2005.

[99] James G Mitchell. The energetics and scaling of search strategies in bacteria. *Am Nat*, 160(6):727–740, Dec 2002.

[100] Dylan M Morris and Grant J Jensen. Toward a biomechanical understanding of whole bacterial cells. *Annu Rev Biochem*, 77:583–613, 2008.

[101] Martin Muhling, Nicholas Harris, Amha Belay, and Brian A. Whitton. Reversal of helix orientation in the cyanobacterium arthrospira1. *Journal of Phycology*, 39(2):360–367, 2003.

[102] Eran A Mukamel, Hazen Babcock, and Xiaowei Zhuang. Statistical deconvolution for superresolution fluorescence microscopy. *Biophys J*, 102(10):2391–2400, May 2012.

[103] Jaan Mnnik, Rosalie Driessen, Peter Galajda, Juan E Keymer, and Cees Dekker. Bacterial growth and motility in sub-micron constrictions. *Proc Natl Acad Sci U S A*, 106(35):14861–14866, Sep 2009.

[104] Hiroshi Nikaido. Molecular basis of bacterial outer membrane permeability revisited. *Microbiol Mol Biol Rev*, 67(4):593–656, Dec 2003.

[105] M. Nirmal, B. O. Dabbousi, M. G. Bawendi, J. J. Macklin, J. K. Trautman, T. D. Harris, and L. E. Brus. Fluorescence intermittency in single cadmium selenide nanocrystals. *Nature*, 383(6603):802–804, October 1996.

[106] T. Ohashi, Y. Ishii, Y. Ishikawa, T. Matsumoto, and M. Sato. Experimental and numerical analyses of local mechanical properties measured by atomic force microscopy for sheared endothelial cells. *Biomed Mater Eng*, 12(3):319–327, 2002.

[107] J. T. Park. Turnover and recycling of the murein sacculus in oligopeptide permease-negative strains of escherichia coli: indirect evidence for an alternative permease system and for a monolayered sacculus. *J Bacteriol*, 175(1):7–11, Jan 1993.

[108] Gary J Patti, Jiawei Chen, and Michael L Gross. Method revealing bacterial cell-wall architecture by time-dependent isotope labeling and quantitative liquid chromatography/mass spectrometry. *Anal Chem*, 81(7):2437–2445, Apr 2009.

[109] Sri Rama Prasanna Pavani and Rafael Piestun. High-efficiency rotating point spread functions. *Opt Express*, 16(5):3484–3489, Mar 2008.

[110] Sri Rama Prasanna Pavani, Michael A Thompson, Julie S Biteen, Samuel J Lord, Na Liu, Robert J Twieg, Rafael Piestun, and W. E. Moerner. Three-dimensional, single-molecule fluorescence imaging beyond the diffraction limit by using a double-helix point spread function. *Proc Natl Acad Sci U S A*, 106(9):2995–2999, Mar 2009.

[111] M Peach and JS Koehler. The forces exerted on dislocations and the stress fields produced by them. *Phys Rev*, 80:436–439, 1950.

[112] Andrew E Pelling, Yinuo Li, Wenyuan Shi, and James K Gimzewski. Nanoscale visualization and characterization of myxococcus xanthus cells with atomic force microscopy. *Proc Natl Acad Sci U S A*, 102(18):6484–6489, May 2005.

[113] Laura Picas, Felix Rico, and Simon Scheuring. Direct measurement of the mechanical properties of lipid phases in supported bilayers. *Biophys J*, 102(1):L01–L03, Jan 2012.

[114] Marco Plomp, Terrance J Leighton, Katherine E Wheeler, Haley D Hill, and Alexander J Malkin. In vitro high-resolution structural dynamics of single germinating bacterial spores. *Proc Natl Acad Sci U S A*, 104(23):9644–9649, Jun 2007.

[115] M. T. Record, E. S. Courtenay, D. S. Cayley, and H. J. Guttman. Responses of e. coli to osmotic stress: large changes in amounts of cytoplasmic solutes and water. *Trends Biochem Sci*, 23(4):143–148, Apr 1998.

[116] Natividad Ruiz, Brian Falcone, Daniel Kahne, and Thomas J. Silhavy. Chemical conditionality: a genetic strategy to probe organelle assembly. *Cell*, 121(2):307–317, Apr 2005.

[117] Natividad Ruiz, Daniel Kahne, and Thomas J Silhavy. Advances in understanding bacterial outer-membrane biogenesis. *Nat Rev Microbiol*, 4(1):57–66, Jan 2006.

[118] Natividad Ruiz, Tao Wu, Daniel Kahne, and Thomas J Silhavy. Probing the barrier function of the outer membrane with chemical conditionality. *ACS Chem Biol*, 1(6):385–395, Jul 2006.

[119] Michael J Rust, Mark Bates, and Xiaowei Zhuang. Sub-diffraction-limit imaging by stochastic optical reconstruction microscopy (storm). *Nat Methods*, 3(10):793–795, Oct 2006.

[120] W. S. Ryu, R. M. Berry, and H. C. Berg. Torque-generating units of the flagellar motor of escherichia coli have a high duty ratio. *Nature*, 403(6768):444–447, Jan 2000.

[121] F. Sachs and C. E. Morris. Mechanosensitive ion channels in nonspecialized cells. *Rev Physiol Biochem Pharmacol*, 132:1–77, 1998.

[122] B. A. Sampson, R. Misra, and S. A. Benson. Identification and characterization of a new gene of escherichia coli k-12 involved in outer membrane permeability. *Genetics*, 122(3):491–501, Jul 1989.

[123] Dirk-Jan Scheffers and Mariana G Pinho. Bacterial cell wall synthesis: new insights from localization studies. *Microbiol Mol Biol Rev*, 69(4):585–607, Dec 2005.

[124] Jagesh V. Shah and Paul A. Janmey. Strain hardening of fibrin gels and plasma clots. *Rheologica Acta*, 36:262, 1997.

[125] Shasad Sharif, Sung Joon Kim, Harald Labischinski, and Jacob Schaefer. Characterization of peptidoglycan in fem-deletion mutants of methicillin-resistant staphylococcus aureus by solid-state nmr. *Biochemistry*, 48(14):3100–3108, Apr 2009.

[126] K. T. Shimizu, R. G. Neuhauser, C. A. Leatherdale, S. A. Empedocles, W. K. Woo, and M. G. Bawendi. Blinking statistics in single semiconductor nanocrystal quantum dots. *Phys. Rev. B*, 63:205316, May 2001.

[127] Thomas J. Silhavy, Michael L. Berman, and Lynn W. Enquist. *Experiments with gene fusions*. Cold Spring Harbor Laboratory, 1984.

[128] R. K. Sizemore, J. J. Caldwell, and A. S. Kendrick. Alternate gram staining technique using a fluorescent lectin. *Appl Environ Microbiol*, 56(7):2245–2247, Jul 1990.

[129] U. B. Sleytr and T. J. Beveridge. Bacterial s-layers. *Trends Microbiol*, 7(6):253–260, Jun 1999.

[130] I. Sonntag, H. Schwarz, Y. Hirota, and U. Henning. Cell envelope and shape of escherichia coli: multiple mutants missing the outer membrane lipoprotein and other major outer membrane proteins. *J Bacteriol*, 136(1):280–285, Oct 1978.

[131] A. M. Spormann. Gliding motility in bacteria: insights from studies of myxococcus xanthus. *Microbiol Mol Biol Rev*, 63(3):621–641, Sep 1999.

[132] Ramanujam Srinivasan, Mithilesh Mishra, Maki Murata-Hori, and Mohan K Balasubramanian. Filament formation of the escherichia coli actin-related protein, mreb, in fission yeast. *Curr Biol*, 17(3):266–272, Feb 2007.

[133] Margarita Staykova, Douglas P Holmes, Clarke Read, and Howard A Stone. Mechanics of surface area regulation in cells examined with confined lipid membranes. *Proc Natl Acad Sci U S A*, 108(22):9084–9088, May 2011.

[134] Andre C Stiel, Martin Andresen, Hannes Bock, Michael Hilbert, Jessica Schilde, Andreas Schnle, Christian Eggeling, Alexander Egner, Stefan W Hell, and Stefan Jakobs. Generation of monomeric reversibly switchable red fluorescent proteins for far-field fluorescence nanoscopy. *Biophys J*, 95(6):2989–2997, Sep 2008.

[135] Cornelis Storm, Jennifer J Pastore, F. C. MacKintosh, T. C. Lubensky, and Paul A Janmey. Nonlinear elasticity in biological gels. *Nature*, 435(7039):191–194, May 2005.

[136] A. R. Strm and I. Kaasen. Trehalose metabolism in escherichia coli: stress protection and stress regulation of gene expression. *Mol Microbiol*, 8(2):205–210, Apr 1993.

[137] Fedor V Subach, Lijuan Zhang, Theodorus W J Gadella, Nadya G Gurskaya, Konstantin A Lukyanov, and Vladislav V Verkhusha. Red fluorescent protein with reversibly photoswitchable absorbance for photochromic fret. *Chem Biol*, 17(7):745–755, Jul 2010.

[138] Matthew T Swulius, Songye Chen, H. Jane Ding, Zhuo Li, Ariane Briegel, Martin Pilhofer, Elitza I Tocheva, Suzanne R Lybarger, Tanya L Johnson, Maria Sandkvist, and Grant J Jensen. Long helical filaments are not seen encircling cells in electron cryotomograms of rod-shaped bacteria. *Biochem Biophys Res Commun*, 407(4):650–655, Apr 2011.

[139] M. Sra and U. B. Sleytr. S-layer proteins. *J Bacteriol*, 182(4):859–868, Feb 2000.

[140] R. Tharmann, M. M A E Claessens, and A. R. Bausch. Viscoelasticity of isotropically cross-linked actin networks. *Phys Rev Lett*, 98(8):088103, Feb 2007.

[141] Russell E Thompson, Daniel R Larson, and Watt W Webb. Precise nanometer localization analysis for individual fluorescent probes. *Biophys J*, 82(5):2775–2783, May 2002.

[142] J. J. Thwaites and N. H. Mendelson. Biomechanics of bacterial walls: studies of bacterial thread made from bacillus subtilis. *Proc Natl Acad Sci U S A*, 82(7):2163–2167, Apr 1985.

[143] J. J. Thwaites and N. H. Mendelson. Mechanical properties of peptidoglycan as determined from bacterial thread. *Int J Biol Macromol*, 11(4):201–206, Aug 1989.

[144] J. J. Thwaites, U. C. Surana, and A. M. Jones. Mechanical properties of bacillus subtilis cell walls: effects of ions and lysozyme. *J Bacteriol*, 173(1):204–210, Jan 1991.

[145] Kittichoat Tiyanont, Thierry Doan, Michael B Lazarus, Xiao Fang, David Z Rudner, and Suzanne Walker. Imaging peptidoglycan biosynthesis in bacillus

subtilis with fluorescent antibiotics. *Proc Natl Acad Sci U S A*, 103(29):11033–11038, Jul 2006.

[146] S. Trachtenberg. Mollicutes-wall-less bacteria with internal cytoskeletons. *J Struct Biol*, 124(2-3):244–256, Dec 1998.

[147] Hung-Yin Tsai and Yen-Wen Huang. Image tracking study on courtship behavior of drosophila. *PLoS One*, 7(4):e34784, 2012.

[148] Robert D Turner, Emma C Ratcliffe, Richard Wheeler, Ramin Golestanian, Jamie K Hobbs, and Simon J Foster. Peptidoglycan architecture can specify division planes in staphylococcus aureus. *Nat Commun*, 1:26, 2010.

[149] F. van den Ent, L. A. Amos, and J. Lwe. Prokaryotic origin of the actin cytoskeleton. *Nature*, 413(6851):39–44, Sep 2001.

[150] Sven van Teeffelen, Siyuan Wang, Leon Furchtgott, Kerwyn Casey Huang, Ned S Wingreen, Joshua W Shaevitz, and Zemer Gitai. The bacterial actin mreb rotates, and rotation depends on cell-wall assembly. *Proc Natl Acad Sci U S A*, 108(38):15822–15827, Sep 2011.

[151] Waldemar Vollmer and Joachim-Volker Hltje. The architecture of the murein (peptidoglycan) in gram-negative bacteria: vertical scaffold or horizontal layer(s)? *J Bacteriol*, 186(18):5978–5987, Sep 2004.

[152] Waldemar Vollmer and Stephen J Seligman. Architecture of peptidoglycan: more data and more models. *Trends Microbiol*, 18(2):59–66, Feb 2010.

[153] A. E. Walsby. The Pressure Relationships of Gas Vacuoles. *Proceedings of the Royal Society of London. Series B. Biological Sciences*, 178(1052):301–326, 1971.

[154] Ping Wang, Lydia Robert, James Pelletier, Wei Lien Dang, Francois Taddei, Andrew Wright, and Suckjoon Jun. Robust growth of escherichia coli. *Curr Biol*, 20(12):1099–1103, Jun 2010.

[155] Siyuan Wang, Hugo Arellano-Santoyo, Peter A Combs, and Joshua W Shaevitz. Actin-like cytoskeleton filaments contribute to cell mechanics in bacteria. *Proc Natl Acad Sci U S A*, 107(20):9182–9185, May 2010.

[156] Siyuan Wang, Leon Furchtgott, Kerwyn Casey Huang, and Joshua W Shaevitz. Helical insertion of peptidoglycan produces chiral ordering of the bacterial cell wall. *Proc Natl Acad Sci U S A*, 109(10):E595–E604, Mar 2012.

[157] G. Wanger, T. C. Onstott, and G. Southam. Stars of the terrestrial deep subsurface: a novel 'star-shaped' bacterial morphotype from a south african platinum mine. *Geobiology*, 6(3):325–330, Jun 2008.

[158] W. WEIDEL, H. FRANK, and H. H. MARTIN. The rigid layer of the cell wall of escherichia coli strain b. *J Gen Microbiol*, 22:158–166, Feb 1960.

[159] D. S. Weiss, J. C. Chen, J. M. Ghigo, D. Boyd, and J. Beckwith. Localization of ftsi (pbp3) to the septal ring requires its membrane anchor, the z ring, ftsa, ftsq, and ftsl. *J Bacteriol*, 181(2):508–520, Jan 1999.

[160] Courtney L White and James W Gober. Mreb: pilot or passenger of cell wall synthesis? *Trends Microbiol*, 20(2):74–79, Feb 2012.

[161] Janet M Wood. Bacterial osmosensing transporters. *Methods Enzymol*, 428:77–107, 2007.

[162] J. Xu, Y. Tseng, and D. Wirtz. Strain hardening of actin filament networks. regulation by the dynamic cross-linking protein alpha-actinin. *J Biol Chem*, 275(46):35886–35892, Nov 2000.

[163] Ke Xu, Hazen P Babcock, and Xiaowei Zhuang. Dual-objective storm reveals three-dimensional filament organization in the actin cytoskeleton. *Nat Methods*, 9(2):185–188, Feb 2012.

[164] Ting Xu, Hongsheng Li, Tian Shen, Nikola Ojkic, Dimitrios Vavylonis, and Xiaolei Huang. Extraction and analysis of actin networks based on open active contour models. *Proc IEEE Int Symp Biomed Imaging*, 2011:1334–1340, Mar 2011.

[165] X. Yao, M. Jericho, D. Pink, and T. Beveridge. Thickness and elasticity of gram-negative murein sacculi measured by atomic force microscopy. *J Bacteriol*, 181(22):6865–6875, Nov 1999.

[166] X. Yao, J. Walter, S. Burke, S. Stewart, M. H. Jericho, D. Pink, R. Hunter, and T. J. Beveridge. Atomic force microscopy and theoretical considerations of surface properties and turgor pressures of bacteria. *Colloids and Surfaces B: Biointerfaces*, 23(2-3):213 – 230, 2002.

[167] Kevin D Young. Bacterial morphology: why have different shapes? *Curr Opin Microbiol*, 10(6):596–600, Dec 2007.

[168] Qiucen Zhang, Guillaume Lambert, David Liao, Hyunsung Kim, Kristelle Robin, Chih kuan Tung, Nader Pourmand, and Robert H Austin. Acceleration of emergence of bacterial antibiotic resistance in connected microenvironments. *Science*, 333(6050):1764–1767, Sep 2011.

[169] Liming Zhao, David Schaefer, Haixin Xu, Swati J Modi, William R LaCourse, and Mark R Marten. Elastic properties of the cell wall of aspergillus nidulans studied with atomic force microscopy. *Biotechnol Prog*, 21(1):292–299, 2005.

[170] Lei Zhu, Wei Zhang, Daniel Elnatan, and Bo Huang. Faster storm using compressed sensing. *Nat Methods*, Apr 2012.

[171] M. Zoratti and V. Petronilli. Ion-conducting channels in a gram-positive bacterium. *FEBS Lett*, 240(1-2):105–109, Nov 1988.